
Electronic Thesis and Dissertation Repository

7-2-2013 12:00 AM

Delay Extraction based Macromodeling with Parallel Processing for Efficient Simulation of High Speed Distributed Networks

Sourajeet Roy
The University of Western Ontario

Supervisor
Dr. Anestis Dounavis
The University of Western Ontario

Graduate Program in Electrical and Computer Engineering
A thesis submitted in partial fulfillment of the requirements for the degree in Doctor of Philosophy
© Sourajeet Roy 2013

Follow this and additional works at: <https://ir.lib.uwo.ca/etd>



Part of the [Electrical and Electronics Commons](#), and the [VLSI and Circuits, Embedded and Hardware Systems Commons](#)

Recommended Citation

Roy, Sourajeet, "Delay Extraction based Macromodeling with Parallel Processing for Efficient Simulation of High Speed Distributed Networks" (2013). *Electronic Thesis and Dissertation Repository*. 1327.
<https://ir.lib.uwo.ca/etd/1327>

This Dissertation/Thesis is brought to you for free and open access by Scholarship@Western. It has been accepted for inclusion in Electronic Thesis and Dissertation Repository by an authorized administrator of Scholarship@Western. For more information, please contact wlsadmin@uwo.ca.

Delay Extraction based Macromodeling with Parallel Processing for Efficient Simulation of High Speed Distributed Networks

(Thesis format: Monograph)

by

Sourajeet Roy

Graduate Program in Engineering Science
Department of Electrical and Computer Engineering

A THESIS SUBMITTED IN PARTIAL FULFILLMENT OF THE REQUIREMENTS FOR
THE DEGREE OF DOCTOR OF PHILOSOPHY

The School of Graduate and Postdoctoral Studies
The University of Western Ontario
London, Ontario, Canada
© Sourajeet Roy 2013

Abstract

With the increase in signal speeds in VLSI systems, distributed effects arising in passive components such as high speed interconnects and power distribution networks are the main contributors of signal and power degradation at chip, package and board levels. As a result, computer aided design strategies targeting modeling and simulation of such high speed systems at the early design stages are critical requirements for VLSI designers. However, the computational demand of accurately capturing the distributed nature of such components is a major bottleneck facing traditional circuit solvers.

This thesis deals with two different approaches towards modeling of high speed distributed networks. One approach deals with cases where the physical characteristics of the network are not available and the network is characterized by its frequency domain, multiport tabulated data. The other approach is based on a detailed knowledge of the physical and electrical characteristics of the network and assuming a quasi transverse mode of propagation of the electromagnetic wave through the network.

In the first part of the thesis, a delay extraction based IFFT algorithm is described for the accurate macromodeling of electrically long interconnect networks characterized by its frequency domain, multiport Y parameter data. An important feature of this work is the ability to extract the higher order delays and the associated attenuation losses embedded in the data via time-frequency decompositions. The effect of including the higher order delays have been shown to lead to greater accuracy over existing direct IFFT or even single delay extraction based IFFT techniques for transient simulation.

The next part of this thesis deals with developing accurate broadband macromodels for package/board level power distribution networks (PDNs) where prior knowledge of the physical and electrical characteristics of the network is readily available. The proposed macromodeling technique is based on a delay extraction feature and has been readily applied to two dimensional (2D) and three dimensional (3D) PDNs with irregular geometries. The key advantage of the algorithm is that through explicit delay extraction, the distributed nature of the PDNs can be accurately captured, leading to more compact and more accurate broadband simulation of the network as compared to traditional lumped modeling approaches.

Finally, waveform relaxation (WR) based algorithms for parallel simulations of large multiconductor interconnect networks and 2D PDNs are presented. A key contribution of this body of work is the identification of naturally parallelizable and convergent iterative techniques that can divide the computational costs of solving such large macromodels over a multi-core hardware. Additional techniques to accelerate convergence, reduce the simulation cost per iteration as well as communication overheads among the cores have been described. Numerical examples are provided to illustrate the superior scalability of the proposed algorithm with respect to the size of the network and available parallel processors when compared to conventional sequential modeling approaches.

Keywords: Convergence, Delay extraction, Electromagnetic interference, High speed interconnects, Iterative algorithms, Macromodeling, Multiconductor transmission lines, Parallel processing, Power distribution networks, Power integrity, Signal integrity, Waveform relaxation.

Acknowledgments

This thesis could not be successful without the invaluable support of my supervisor Dr. Anestis Dounavis of the Department of Electrical and Computer Engineering at University of Western Ontario. I would like to express my gratitude towards him for introducing me to the area of computer aided design for VLSI applications and inculcating in me the enthusiasm for research. His motivation, keen acumen in this field of research and friendly disposition has always been a major motivation for my work.

I would also like to extend my thanks towards every faculty member, staff member and friend of the Department of Electrical and Computer Engineering, Western University for their support and help at various stages of my thesis work. I would like to specially mention my colleagues Dr. Majid Ahmadloo, Dr. Amir Beygi and Dr. Ehsan Rasekh for their invaluable advice and inspiration.

In addition, I would like to thank my parents, Mr. Tarit Kanti Roy and Mrs. Shanghamitra Roy for their blind faith in my scholarly ability even when it was convenient not to. I would also like to thank my sister Dr. Sohinee Roy for being the loudest cheerleader for me. She has taught me that every obstacle is just a detour, not a dead end. Finally, this thesis would have been impossible without the presence of my dearest friend, Ms. Alka Grover. Despite the miles separating us, her support and faith has been a torch that I carried through the best and worst of times.

Table of Contents

Abstract	ii
Acknowledgments.....	iv
Table of Contents	v
List of Tables	ix
List of Figures	x
Abbreviations	xv
Chapter 1	1
1 Introduction	1
1.1 Background and Motivation	1
1.2 Objectives and Contributions.....	5
1.3 Organization of the Thesis	7
Chapter 2	9
2 Background and Literature Review	9
2.1 Introduction.....	9
2.2 Macromodeling based on Measured Data.....	10
2.3 Macromodeling of Power Distribution Networks.....	13
2.3.1 Single Layered PDNs.....	15
2.3.2 Multilayered PDNs.....	16
2.4 High Speed Interconnect Modeling	20
2.5 Simulating Interconnects in SPICE-like Simulators.....	22
2.5.1 Lumped Segmentation	22
2.5.2 Matrix Rational Approximation.....	23
2.5.3 Method of Characteristics	25

2.5.4	Delay Extraction-Based Passive Compact Transmission-Line Macromodeling Algorithm (DEPACT)	27
2.5.5	Transmission Line Macromodels with Incident Fields	29
2.6	Waveform Relaxation for Parallel Simulation	30
2.6.1	Optimization based LP-WR	32
2.6.2	MoC based LP-WR	33
Chapter 3	35
3	Transient Simulation of Distributed Networks using Delay Extraction based Numerical Convolution	35
3.1	Introduction	35
3.2	Motivation and Review of Time-Frequency Decompositions	36
3.2.1	Motivation	36
3.2.2	General Time-Frequency Decompositions	37
3.3	Development of the Proposed Algorithm	39
3.3.1	Determining Multiple Delays (T_K)	39
3.3.2	Partitioning the Time-Frequency Plane	42
3.3.3	Computing the Attenuation Losses ($Y_{ij}^{(k)}(s)$)	43
3.4	Numerical Examples	45
3.5	Conclusion	53
Chapter 4	54
4	Delay Extraction based Macromodeling of Power Distribution Networks	54
4.1	Introduction	54
4.2	Development of the Proposed Macromodel	55
4.2.1	Formulation of Transmission Line Model for PDN	55
4.2.2	Modeling Unit Cells using DEPACT	59
4.2.3	SPICE Realization of Lossy Section	60
4.3	Numerical Examples	63

4.4 Conclusion	70
Chapter 5	71
5 Longitudinal Partitioning based Waveform Relaxation Algorithm for Efficient Analysis of Distributed Transmission Line Networks	71
5.1 Introduction.....	71
5.2 Overview of Waveform Relaxation Algorithms.....	72
5.3 Development of the Proposed Waveform Relaxation Algorithms	73
5.3.1 Proposed Partitioning Scheme for MTLs	74
5.3.2 Iterative Solution of Subcircuits using Gauss-Jacobi	76
5.3.3 Hybrid Iterative Solution of Subcircuits	77
5.4 The Computational Complexity of the Proposed Algorithm.....	80
5.5 Numerical Results	84
5.6 Conclusion	90
Chapter 6	91
6 Electromagnetic Interference Analysis of Multiconductor Transmission Line Networks using Longitudinal Partitioning based Waveform Relaxation Algorithm	91
6.1 Introduction.....	91
6.2 Background of EMI Analysis of MTL Networks	93
6.2.1 General Formulation of MTLs Exposed to Incident EM Fields	93
6.2.2 DEFACT Model for EMI Analysis.....	95
6.3 Development of the Proposed WR Algorithm.....	98
6.3.1 Generation of Compact Subcircuits	98
6.4 Numerical Examples	103
6.5 Conclusion	108
Chapter 7	109
7 Delay Extraction based Waveform Relaxation Algorithm for Fast Transient Analysis of Power Distribution Networks	109

7.1	Introduction.....	109
7.2	Development of the Proposed WR Algorithm.....	111
7.2.1	Proposed 2D Partitioning Methodology	114
7.2.2	Effect of Decoupling Capacitors.....	114
7.2.3	2D Hybrid Iterative Technique	116
7.3	Numerical Examples	120
7.5	Conclusions.....	127
Chapter 8	128
8	Summary and Future Work.....	128
8.1	Summary	128
8.2	Future Work	130
	References.....	133
	Curriculum Vitae.....	145

List of Tables

Table 3-1: Identified delays (Example 1).....	41
Table 3-2: Partitioning of the (ω, τ) plane for Example 1	42
Table 3-3: Comparison of identified delays with the theoretical values of (3.18) for Example 2.....	48
Table 3-4: Partitioning of the (ω, τ) plane for Example 2.....	48
Table 3-5: Identified delays (Example 3).....	50
Table 3-6: Partitioning of the (ω, τ) plane for Example 3.....	51
Table 4-1: Comparison of CPU run time and accuracy of proposed model with lumped model for Example 1.....	64
Table 4-2: Comparison of CPU run time and accuracy of proposed model with lumped model for Example 2.....	69
Table 5-1: Comparison of CPU run time for Example 2.....	89
Table 6-1: Comparison of CPU run time for Example 2.....	106
Table 7-1: Change in rate of convergence with number of decoupling capacitors for Example 1.....	122
Table 7-2: Comparison of CPU run time for Example 2.....	125

List of Figures

Figure 2-1: Modeling of PDN. (a) Single layered PDN. (b) Discretization of PDN into unit cells.	14
Figure 2-2: π representation of a unit cell.....	214
Figure 2-3: Illustrative example of multilayered PDN. (a) Original four layered structure (b) Original structure decomposed into two separate multilayered structures.	24
Figure 2-4: (a) Unit cell from the four layered PDN of Fig. 2-3. (b) Lumped π model of unit cell.....	27
Figure 1-5: Three-dimensional and cross sectional views of an interconnect structure.	19
Figure 1-6: Lumped transmission line model for single transmission line.....	21
Figure 1-7: Circuit realization of MoC for a two-conductor transmission line.....	24
Figure 1-8: Circuit realization of DEFACT macromodel.....	27
Figure 1-9: Longitudinal partitioning of single transmission line using lumped RLGC model	31
Figure 1-10: Subcircuits generated from Fig. 2.9 for single transmission line (no optimization).....	31
Figure 3-1: Circuit layout of illustrative example. (a) Circuit layout. (b) Geometric layout.....	40

Figure 1-2: Evaluating delay peaks of Example 1. (a) Energy of $ Y_{11} $ ($\eta_{11}(\tau)$). (b) Energy of $ Y_{12} $ ($\eta_{12}(\tau)$).....	41
Figure 3-3: Transient response of Example 1 using the proposed algorithm, HSPICE's W-element and direct IFFT. (a) Response at P2. (b) Response at P3.....	41
Figure 3-4: Propagation delay capture of Example 1 using the proposed algorithm, HSPICE's W-element and direct IFFT. (a) Response at P2. (b) Response at P3.....	44
Figure 3-5: Two port circuit for Example 2.....	46
Figure 3-6: Evaluating delay peaks of Example 2. (a) Energy of $ Y_{11} $ ($\eta_{11}(\tau)$) (b) Energy of $ Y_{12} $ ($\eta_{12}(\tau)$).....	47
Figure 3-7: Transient response at far end of Example 2.....	49
Figure 3-8: Two port circuit for Example 3.....	49
Figure 3-9: Transient response of Example 3 using the proposed algorithm, HSPICE's W-element and single delay extraction based IFFT [19]. (a) Response at Port 1. (b) Response at Port 2.....	52
Figure 4-1: Lumped circuit of a single face of unit cell.	55
Figure 4-2: (a) Multilayered unit cell. (b) Unit cell model using MTLs.	58
Figure 4-3: DEFACT realization of the single face of the unit cells using MTLs.	59
Figure 4-4: Physical structure of PDN for Example 1.....	62

Figure 4-5: Comparison of the proposed DEPACT model with the quasi-static lumped model. (a) Frequency domain response (Z_{12}). (b) Transient response at Port 2.	63
Figure 4-6: 6 coupled multilayered PDN problem of Example 2.....	65
Figure 4-7: Comparison of S parameters of Example 2 using the proposed and the lumped models for cell dimensions $l = 0.5$ cm. (a) Magnitude of S_{12} . (b) Magnitude of S_{13}	67
Figure 4-8: Comparison of S parameters of Example 1 using the proposed model ($l = 0.5$ cm) and the lumped model ($l = 0.167$ cm). (a) Magnitude of S_{12} . (b) Magnitude of S_{13}	67
Figure 4-9: Comparison of transient response of Example 2 using the proposed macromodel ($l = 0.5$ cm) and the lumped model ($l = 0.167$ cm) (a) Response at Port 2 (b) Response at Port 3.....	68
Figure 5-1: SPICE equivalent circuit of a MTL using DEPACT.....	73
Figure 5-2: Partitioning of MTLs into subcircuits for waveform relaxation.....	75
Figure 5-3: Hybrid GS-GJ iterative technique.....	78
Figure 5-4: Circuit of Example 1.....	85
Figure 5-5: Transient response for Example 1. All line lengths are $l = 30$ cm. (a) Transient response at output port N_1 . (b) Transient response at output port N_2	86
Figure 5-6: Convergence properties of the proposed hybrid iterative technique compared to GJ. All line lengths are $l = 30$ cm.....	86
Figure 5-7: Transmission line structure of Example 2.....	87

Figure 5-8: Transient response for Example 2. Line length of the network is $l = 50$ cm. (a) Transient response at output port N_1 . (b) Transient response at output port N_2	87
Figure 5-9: Scaling of computational cost for Example 2. (a) Scaling of computational cost with line length (l) (b) Scaling of CPU speed up with number of CPUs (p) ($l = 200$ cm).....	89
Figure 6-1: Geometry of a multiconductor transmission line exposed to an incident field.....	93
Figure 6-2: Discretization of MTL using DEFACT in the presence of incident fields.....	97
Figure 6-3: Proposed circuit representation of the incident field coupled with i^{th} lossless section. (a) Prior to grouping of the lumped sources. (b) After grouping of the lumped sources using (6.20).	100
Figure 6-4: Three coupled microstrip lines of Example 1. (a) Geometry of the transmission lines. (b) Circuit layout of the transmission lines.....	102
Figure 6-5: Transient response for Example 1 using the proposed LP-WR algorithm and full simulation. (a) Transient response at output port 4 (b) Transient response at output port 5.....	103
Figure 6-6: Transient response (V_{out}) of inverter in Example 1 with incident fields.....	104
Figure 6-7: Computational efficiency of the proposed LP-WR algorithm over full EMI simulation. (a) Scaling of computational cost with line length (l) (b) Scaling of CPU speed up with number of CPUs (p) ($l = 200$ cm).....	106

Figure 7-1: Equivalent circuit models for PDNs. (a) Transmission line representation of unit cell. (b) DEPACT representation of unit cell. (c) Equivalent circuit model of unit cell).....	111
Figure 7-2: Partitioning along the natural MoC interfaces provided by DEPACT model...	112
Figure 7-3: Proposed 2D partitioning.....	113
Figure 7-4: PDN structure of Example 1.....	120
Figure 7-5: Transient response for Example 2 using the proposed WR algorithm and full simulation. (a) Transient response at output port B using decoupling capacitors. (b) Transient response at output port B without decoupling capacitors.....	122
Figure 7-6: PDN structure of Example 1.....	124
Figure 7-7: Scaling of computational cost for Example 2. (a) Scaling of computational cost with number of subcircuits (N_0) (number of CPUs set to 1). (b) Scaling of CPU speed up with number of CPUs (p) ($N_0 = 100$).....	125

Abbreviations

CAD	Computer aided design
CMOS	Complementary metal oxide semiconductor
DEPACT	Delay extraction-based passive compact transmission-line macromodel
EMI	Electromagnetic interference
IC	Integrated circuit
IFFT	Inverse fast Fourier transform
LP-WR	Longitudinal partitioning based waveform relaxation
MNA	Modified nodal analysis
MoC	Method of characteristics
MRA	Matrix rational approximation
MTL	Multi-conductor transmission line
ODE	Ordinary differential equation
PCB	Printed circuit board
PDE	Partial differential equation
PDN	Power distribution network
PMoC	Passive method of characteristics
PRIMA	Passive reduced-order interconnect macromodeling algorithm.
p.u.l	Per-unit-length.
SPICE	Simulation program with integrated circuit emphasis
TEM	Transverse electromagnetic
TP-WR	Transverse partitioning based waveform relaxation
VF	Vector fitting

VLSI	Very large scale integration
WR	Waveform relaxation

Chapter 1

1 Introduction

1.1 Background and Motivation

Computer aided design (CAD) has become an integral step in the design, analysis and testing of very large scale integrated (VLSI) circuits and their packaging into electronic products. Through CAD, it has now become possible to perform complex sensitivity analyses, tolerance analyses and optimization studies of VLSI circuit design at the push of a button leading to easier understanding of design roadblocks and performance tradeoffs. However, for CAD to remain relevant, the simulations tools have to be able to take into account the rapid growth in packaging density, operating speeds and diverse functionality of modern integrated circuits (ICs).

A key aspect of CAD is signal integrity analysis. Signal integrity analysis is the investigation of signal quality as it travels through high speed interconnects. At high frequencies of operation, interconnects behave like distributed transmission lines. This distributed performance of interconnects are often the reason behind effects such as signal delay,

distortion, attenuation, electromagnetic interference (EMI), ringing and crosstalk which can severely degrade system performance and even lead to false switching of logic gates and damage terminating electronic circuits [1]-[3].

Another critical area of CAD is power integrity analysis. Power integrity analysis is the study of the distribution of the power supply to the active electronic circuits through power distribution networks (PDNs) [4]-[5]. Like high speed interconnects, PDNs are distributed networks and often are the sites of resonance, ground bounce, simultaneous switching noise (SSN), electromagnetic radiation and return path discontinuities (RPDs). Such effects not only lead to unreliable power distribution within the system but when coupled to the signal network, can adversely affect the signal quality as well [5].

Based on the above discussion, it is noted that accurate modeling of interconnects and PDNs are extremely important for the early stages of iterative electronic product design. However, commercial circuit simulators with integrated circuit emphasis such as SPICE [6] are typically unable to perform simulation of distributed networks terminated by nonlinear circuits (typically complementary metal oxide semiconductor (CMOS) circuits) as they suffer from the frequency/time mismatch problem. This frequency/time mismatch problem arises from the fact that distributed networks are described by partial differential equations (PDE) which are well represented in the frequency domain, whereas the transient responses of nonlinear circuits are described in the time domain by nonlinear differential equations. Hence, in order to perform transient analysis of distributed networks terminated by nonlinear CMOS circuits, macromodeling algorithms are required to convert the governing PDEs into a matrix of ordinary differential equations (ODE) in the time domain [1]-[3].

Macromodeling algorithms can be categorized into two classes – one class of algorithms deal with modeling of networks where no knowledge of the physical characteristics of the network structure is available whereas another class of algorithms deals with modeling of networks where *a priori* knowledge of the physical characteristics of the network is available and assuming a quasi transverse electromagnetic (TEM) mode of propagation through the network.

For the case where no knowledge of the physical characteristics of the network exists, the network is characterized by frequency domain, multiport tabulated data obtained either from electromagnetic simulations or from measurements [7]-[21]. The behavior of high speed distributed networks can be represented by frequency-dependent admittance, impedance, or scattering parameters. It is noted that although an inverse fast Fourier transform (IFFT) can be used to convert the multiport, frequency domain data into time domain for transient analysis, since the tabulated data is bandlimited, direct IFFT cannot explicitly enforce the delay of the port-to-port transfer functions and result in significant error in signal integrity analysis [19]. In a recent work [19], a single delay extraction based IFFT macromodel was developed. This algorithm was found to be highly accurate for networks with one dominant delay. However, this technique was unable to capture higher order delays due to multiple reflections at the far end of the network and hence has accuracy problems for general distributed networks with multiple dominant delays in the transfer function [21].

Macromodeling algorithms of a network with known physical characteristics can be either based on quasi-static lumped modeling algorithms or delay extraction based algorithms. Lumped modeling techniques include lumped resistive-inductive-conductive-capacitive

RLGC macromodel (for interconnect networks [1] and for PDNs [5]-[22]), PRIMA [23] and matrix rational approximation (MRA) [24]-[25], to name a few. The advantage of these algorithms is that they can be made to be passive by construction. However, lumped models attempt to implicitly approximate the delay of distributed networks such as high speed interconnects and PDNs as a rational function and hence require high order approximations to accurately capture the high frequency poles contributed by the delay portion of the transfer function. This leads to exorbitantly large models which are inefficient for use in the early design cycles.

On the other hand, delay extraction based techniques explicitly extract the delay of the network, thereby explicitly capturing most of the high frequency poles of the transfer function. The remainder of the transfer function can be approximated using a low order rational approximation leading to relatively compact and more accurate models than lumped modeling techniques. The generalized method of characteristics (MoC) is one such algorithm which has proved to be very efficient for long, low loss interconnect modeled as multiconductor transmission lines (MTLs) [26]-[30]. However, a major limitation of MoC is the potential loss of passivity that can occur in the model. Since transmission lines are passive elements, loss of passivity of the macromodel can lead to unstable results in the transient simulation even when terminated with passive circuits [8].

Recently, the delay extraction based passive macromodeling algorithm (DEPACT) has been found to provide very good results for modeling long interconnects compared to lumped models [31]-[32]. Not only does the DEPACT use a delay extraction feature for efficient analysis of electrically long networks but is also passive by construction, unlike the

generalized MoC algorithm. Nonetheless, the DEPACT being a sectioning based model, its accuracy depends on the losses of the interconnect network, line length and the maximum frequency of operation. As these parameters increase, additional sections need to be added thereby augmenting the computational costs of the algorithm. Thus, attempts to mitigate the rapid increase in simulation cost of the DEPACT algorithm with the network size and frequency of operation are still an open problems. Recently the delay extraction based W-element model (based on the MoC and provided by the SPICE platform) has been utilized to efficiently model single layered PDNs [33].

1.2 Objectives and Contributions

The objective of this thesis is to develop efficient broadband macromodeling algorithms for distributed networks such as high speed interconnects and PDNs and the following contribution are presented in this thesis.

Firstly, a delay extraction based IFFT algorithm is proposed for accurate and delay-causal transient analysis of high speed interconnects characterized by their frequency domain, multiport Y parameter data. The proposed algorithm uses time-frequency decompositions to extract multiple propagation delays and the associated attenuation losses from the frequency domain data in a piecewise manner, and then implements IFFT to efficiently convert the frequency response into a sum of delayed time domain responses. Numerical examples illustrate that the proposed algorithm shows significantly more accurate results for networks with multiple delays when compared to existing IFFT based macromodels.

Secondly, for PDNs where the physical characteristics of the structure are known and the electrical model can be derived from the discretization of the Helmholtz wave equation, novel delay extraction based modeling techniques have been developed. These techniques are based on the extension of the one dimensional (1D) DEFACT algorithm to the single layered (2D) and multilayered (3D) PDN structures in presence of holes, apertures and irregular geometry. Numerical examples have been performed to demonstrate the efficiency and accuracy advantages of the DEFACT algorithm for these 2D and 3D problems compared to the existing lumped modeling techniques.

Thirdly, for the parallel simulation of electrically long interconnects, a longitudinal partitioning based waveform relaxation (LP-WR) algorithm is developed. The key feature of this WR algorithm is that it exploits the DEFACT algorithm to ensure weak coupling between the subcircuits and consequently provides swift convergence. Furthermore, a hybrid iterative technique that combines the high parallelizability of Gauss-Jacobi iterative algorithms with the fast convergence of Gauss-Seidel iterative algorithms has been developed for further accelerating the convergence of the WR iterations. The overall algorithm exhibits good scaling with both the size of the network involved and the number of CPUs available leading to significant improvement in the computational costs over sequential SPICE algorithms.

Fourthly, electromagnetic interference (EMI) analysis of high speed interconnects using the above LP-WR algorithm has been proposed as well. A key feature of this work is that the benefits of parallel processing and the hybrid WR iterations can be easily extended to the

problem where EMI analysis is required. Hence, the proposed parallelizable algorithm is significantly more efficient than sequential SPICE algorithms for EMI.

Finally, the proposed WR algorithm has been extended to the problem of efficient modeling of singly layered (2D) PDNs. For PDN problems, the longitudinal partitioning algorithm and the hybrid WR iterations have been extended to a 2D partitioning scheme compatible with a 2D hybrid WR iterations. The overall algorithm retains its highly parallelizable and exhibits good scaling with both the size of the PDN involved and the number of CPUs available, similar to what has been observed for interconnect problems.

1.3 Organization of the Thesis

The thesis is organized as follows. Chapter 2 reviews the existing state of art for macromodeling of high speed interconnects and PDNs. This chapter covers both classes of macromodeling techniques – those based on port-to-port tabulated data as well as those based on quasi-TEM mode of propagation where the physical structure of the network is known. Moreover, a review of existing longitudinal partitioning based WR algorithms is also provided. Chapter 3 deals with the development of the proposed delay extraction based IFFT algorithm for macromodeling of interconnects characterized by port-to-port tabulated data. Examples are provided to compare the proposed work with pure IFFT based techniques and single delay extraction based IFFT techniques. Chapter 4 deals with the development of the delay extraction based macromodeling techniques for single layered (2D) and multilayered (3D) PDN structures. Numerical examples are provided to demonstrate the efficient and

accuracy of the proposed algorithms with respect to existing lumped techniques. Chapter 5 covers the proposed LP-WR algorithm for high speed interconnects and provides examples to demonstrate the advantages of this WR technique over sequential algorithms and other existing longitudinal partitioning based WR algorithms. Chapter 6 extends the LP-WR algorithm of Chapter 5 to the problem of EMI in high speed interconnects and chapter 7 covers the extension of the proposed WR algorithm to the 2D problem of PDNs. Finally, Chapter 8 summarizes the proposed work and also presents some suggestions for future related work.

Chapter 2

2 Background and Literature Review

2.1 Introduction

Interconnects provide the physical path for the signal to propagate between electrical devices in chips, electrical packages, printed circuit boards (PCB) etc. At low frequencies, interconnects can be modeled using a quasi-static lumped electrical RLGC model [1]-[2]. However, at high frequencies, when the wavelength of the travelling electromagnetic wave surrounding the conductors are much smaller than the line length, interconnects behave as distributed transmission lines and this distributed nature of performance is responsible for non ideal effects such as signal delay, distortion, attenuation, ringing and crosstalk [1], [2]. Similarly, PDNs at low frequencies behave as purely capacitive elements while at high frequencies they too exhibit distributed behavior [5]. In course of this chapter, the state of the art regarding macromodeling of such high speed distributed networks will be reviewed. The organization of this chapter is as follows: Section 2.2 explains macromodeling of high speed interconnect networks which are characterized by frequency domain, multiport tabulated data while Section 2.3 covers

the modeling of PDN structures using the conventional lumped electrical RLGC model. Section 2.4 explains macromodeling of high speed interconnect networks derived from quasi-TEM mode of propagation and Section 2.5 provides several transmission line macromodels for nonlinear circuit simulators. Finally, Section 2.6 describes existing WR techniques for parallel simulation of large networks.

2.2 Macromodeling based on Measured Data

Typically large interconnect networks can be characterized by their frequency domain, multiport admittance (Y), impedance (Z), or scattering (S) parameters obtained as tabulated data [7]-[21]. The goal of macromodeling is to derive accurate models based on this tabulated data which can then be reused for any arbitrary terminations.

Presently, there are two approaches towards deriving macromodels of interconnect networks characterized by band limited frequency domain data. One approach is based on approximating the tabulated data using rational functions via least squares curve fitting techniques such as vector fitting (VF) [10] and interpolation-based complex rational approximation [7]-[8]. In the time domain, the rational macromodel can be analytically represented as a sum of decaying exponentials and convoluted with any input signal using the recursive convolution technique [34]. The drawback of such rational macromodeling techniques lie in the fact that they attempt to implicitly capture the delay feature of the transfer function using rational basis functions and consequently require a large number of rational functions for broadband macromodels. Since the memory and time complexities associated with rational curve fitting scale as $O(N_p^2)$ and $O(N_p^4)$

respectively, where N_p is the number of identified poles, for conventional rational modeling of interconnect networks, N_p may be exorbitantly large and such models are computationally expensive to obtain [19]. Furthermore, passivity constraints need to be satisfied by the derived rational models in order to guarantee stable responses for the model connected to any arbitrary terminations [8]. Typical passivity enforcement techniques, such as that reported in [35], result in additional post processing and may increase the incurred computational costs.

Recently, new curve fitting techniques have been proposed based on delayed rational macromodeling techniques [17]-[18]. These techniques extract the propagation delays from the tabulated data while the remaining attenuation losses of the frequency response are approximated using rational curve fitting. This allows the time domain transfer function to be obtained as a sum of delayed exponentials which can be convoluted with any given input using the recursive convolution technique [34]. While such models are more compact in nature, they still require additional passivity enforcement schemes before they can be integrated with any arbitrary circuit termination.

An alternative approach seeks to simply perform an IFFT operation to convert the tabulated frequency domain data into time domain data, which can then be convoluted with any input using a numerical convolution technique. The advantages of an IFFT operation lies in the fact that it does not require a least square fitting operation and hence avoids the large memory and time constraints of such techniques. Moreover, an IFFT operation does not require any passivity enforcement. However, these techniques are not delay-causal by construction which is defined as an impulse response equal to zero for $t < t_p$, where t_p is the propagation delay of the system [19]. This is because a direct IFFT of a

band limited data does not explicitly preserve the delay of the transfer function and leads to signal fluctuations in early time [21]. In order to preserve the delay causality of the model, a single delay extraction based IFFT algorithm was proposed in [19] and is reviewed below.

Let us consider an interconnect network characterized by its frequency domain, multiport Y parameter data as

$$Y(s) = [Y_{ij}(s)]; \quad (i, j \in 1, \dots, P) \quad (2.1)$$

where

$$Y_{ij}(s) = H_{ij}(s)e^{-sT_{ij}} \quad (2.2)$$

and H_{ij} represents the remainder of the transfer function once the dominant delay T_{ij} has been extracted. From (2.1), it is noted that

$$|Y_{ij}(s)| = |H_{ij}(s)| \quad (2.3)$$

Based on (2.3), $\arg(H_{ij})$ can be obtained from the Hilbert transform as

$$\arg(H_{ij}(s)) = -\frac{1}{2\pi} \rho \int_{-\pi}^{\pi} \ln |Y_{ij}(j\theta)| \cot\left(\frac{s-j\theta}{2j}\right) d\theta \quad (2.4)$$

where ρ is the Cauchy's principal value of the integral and $\arg(x)$ is the argument of x [19]. Based on the knowledge of (2.3)-(2.4), the dominant delay T_{ij} can be approximated as

$$T_{ij} = -avg \text{ slope} \left(\arg \left(\frac{Y_{ij}(s)}{H_{ij}(s)} \right) \right) \quad (2.5)$$

where $\text{avg}(x)$ represents the average of a tabulated data x . Once the delay T_{ij} has been extracted, performing the IFFT on H_{ij} and enforcing the extracted delay yields a delay-causal response. Due to the explicit delay enforcement feature of this algorithm, it provides more accurate transient results compared to directly implementing IFFT on the data.

It is noted, however that for the Hilbert transform of (2.4), H_{ij} has to be a minimum phase response (i.e. it does not have any poles or zeros in the right half of the Laplace plane) [36]. This is true if there are no higher order delays embedded in H_{ij} or if the higher order delays have very little contribution to the function H_{ij} . This is because any general delay terms (e^{-sT}) embedded in H_{ij} may contribute zeroes in the right half of the Laplace plane. However, multiple reflections of the signal at the terminations of interconnect networks may result in significantly large higher order delays. As a result, sophisticated algorithms to extract the higher order delays are required for the case when H_{ij} may not exactly be a minimum phase response.

2.3 Macromodeling of Power Distribution Networks

Power Distribution Networks (PDNs) provide a path for the power supply to the core logic circuits and I/O drivers of high speed digital systems [4]-[5]. Ideally PDN should exhibit low impedance over a large frequency range of operation so that the transient

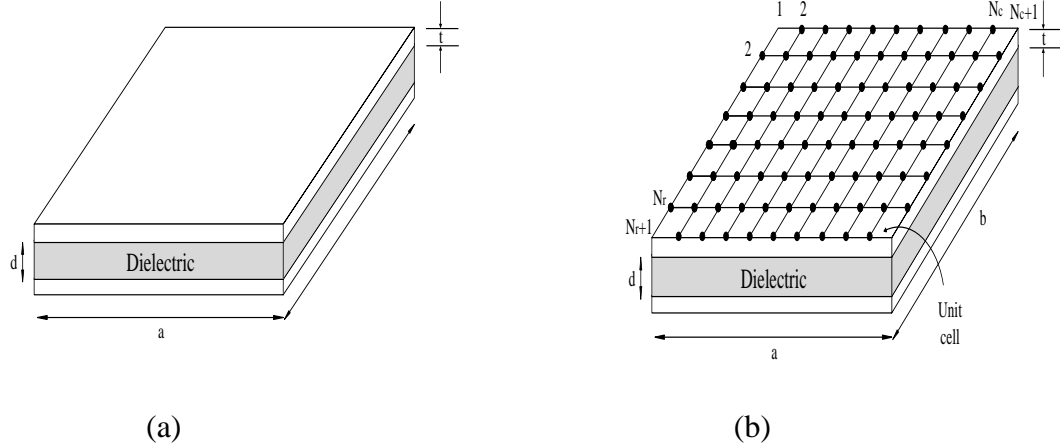


Figure 2-1: Modeling of PDN. (a) Single layered PDN. (b) Discretization of PDN into unit cells.

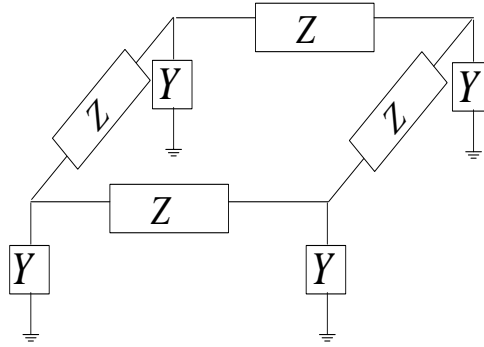


Figure 2-2: π representation of a unit cell. Each Z and Y block can be modeled using quasi-static lumped RLGC network [5].

currents induced by the simultaneous switching of digital circuits do not lead to excessive noise propagation over the PDN [4]-[5]. However with the progressive increase in clock speed, scaling of supply voltage, high switching speed of logic circuits and reduced noise margins, effects like ground bounce, EM interference and SSN noise arising in the PDNs can quickly lead to undesirable voltage fluctuations and propagation delays in chip, board and packaging levels. Hence PDNs are fast emerging as a critical area for electromagnetic compatibility (EMC) and power integrity (PI) verification for high speed

packages.

2.3.1 Single Layered PDNs

A PDN consisting of a rectangular signal/ground plane with single layered dielectric in between and assumed to be free of any surface irregularity is considered in Fig. 2-1(a). This PDN is typically represented in the frequency domain by the Helmholtz PDE [5]. In order to derive a macromodel that can represent the electrical performance of the PDN, typically finite difference discretization of the Helmholtz PDE is performed. Such a discretization of the PDE can be physically visualized as the discretization of the geometry into a grid of unit cells as shown in Fig. 2-1(b). The equivalent circuit representing a unit cell can be obtained from the physical and electrical parameters of the plane using a quasi-static model provided the dielectric separation between the power and ground plane pairs is much smaller compared to the dimensions of the plane [5]. Considering a square unit cell of dimensions (l) with a dielectric separation of (d) between planes, thickness of metal (t), metal conductivity (σ), loss tangent (δ) and relative permittivity (ϵ_r), the equivalent electrical parameters are

$$\begin{aligned} R &= \frac{2}{\sigma t}, C = \epsilon_o \epsilon_r \frac{l^2}{d}, L = \mu_o d, \\ G &= \omega C \tan(\delta), R_s = 2\sqrt{\frac{s\mu_o}{\sigma}} \end{aligned} \quad (2.6)$$

where $s = 2j\pi f$ is the Laplace variable, f is the instantaneous frequency, ϵ_o and μ_o are the permittivity and the permeability of free space, ϵ_r is the relative permittivity of the dielectric and R , L , G , C and R_s are the resistive, inductive, capacitive, conductive and skin effect losses contribution of the unit cell respectively [5]. Based on the parameters of (2.6), each unit cell of Fig. 2.1(b) can be represented by a π model as shown in Fig. 2-2

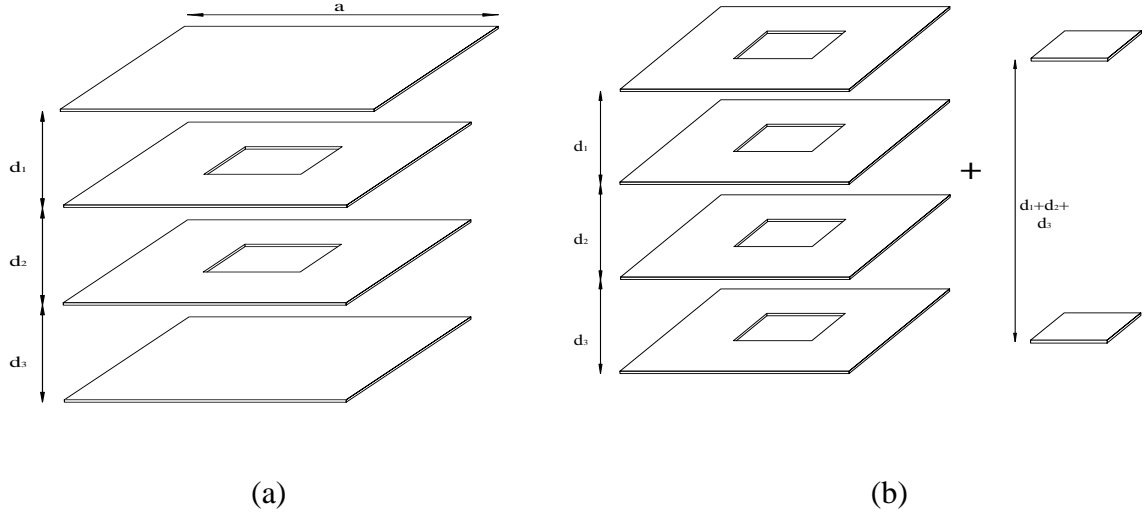


Figure 2-3: Illustrative example of multilayered PDN. (a) Original four layered structure
 (b) Original structure decomposed into two separate multilayered structures.

[5]. In particular, the Z and Y blocks of the π model can be realized using RL and RC ladder networks respectively as explained in [5] thereby allowing for their SPICE implementation.

2.3.2 Multilayered PDNs

Realistic multilayered PDN designs consist of multiple irregular shaped planes stacked vertically. Due to the presence of apertures, holes and irregular geometry of the planes, wraparound currents are supported on the plane layers which lead to the electromagnetic (EM) coupling between individual planes in the transverse direction [5], [37].

For multilayered PDNs, modeling techniques based on the multilayered finite difference method (MFDM) has been proposed [37]. This MFDM model discretizes the multilayered PDN structure to yield an equivalent three dimensional (3D) lumped circuit model which can be directly realized in SPICE for both frequency and transient analysis. In order to understand how that is possible, the illustrative example consisting of four

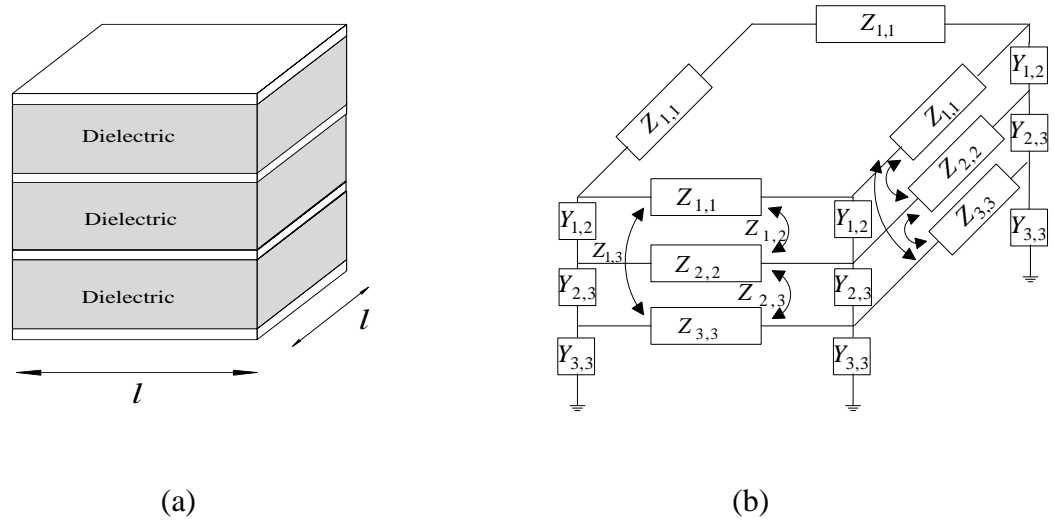


Figure 2-4: (a) Unit cell from the four layered PDN of Figure 2-3. (b) Lumped π model of unit cell.

vertically stacked square planes as shown in Fig. 2-3(a) is considered. It is observed that the presence of an aperture in the middle planes will give rise to wraparound currents thereby leading to EM coupling between all four planes. The coupled four plane structure can be considered as made up of two separate multilayered PDN structure consisting of four and two layers as shown in Fig. 2-3(b). For any multilayered structures of Fig. 2-3(b), each i^{th} plane assigns the $i+1^{\text{th}}$ plane below it as its local reference plane. In other words, considering a current on the bottom of the i^{th} plane, the return path for the same current is considered to exist on the top of the $i+1^{\text{th}}$ plane below.

A common methodology of modeling the multilayered PDNs of Fig. 2-3(b) is by discretizing the structures into numerous multilayered unit cells based on a finite difference treatment of the Helmholtz equation [37]. A unit cell of the four layered PDN section of Fig. 2-3(b) is shown in Fig. 2-4(a). The resistive (R_i), inductive (L_i), capacitive (C_i), conductive (G_i) and skin effect loss (\hat{R}_i) parameters of each i^{th} plane of the unit cell

of Fig. 2-3(a) with respect to its local reference ($i+1^{\text{th}}$ plane of the unit cell of Fig. 2-4(a)) can be described using a quasi-static model provided the dielectric separation between the planes is much smaller compared to the dimensions of the plane similar to what has already been done in (2.6) [5]. In order to obtain an equivalent circuit model of Fig. 2-4(a) compatible with SPICE, the local reference planes of Fig. 2-4(a) are replaced by a single common ground plane which is taken as the bottommost planes in the stacked structures. As a result, the electrical parameters of each i^{th} plane of the unit cell of Fig. 2-4(a) with respect to the common ground is obtained as [5], [37]

$$L_{i,i} = \mu_o \sum_{k=i}^{N-1} d_k$$

$$L_{i,j} = \begin{cases} L_{i,i} & \text{for } i > j \\ L_{j,j} & \text{for } i < j \end{cases} \quad (2.7)$$

$$C_{i,i}(s) = \begin{cases} \epsilon_o \epsilon_r(s) \frac{l^2}{d_{N-1}} & \text{for } i = N-1 \\ 0 & \text{for } i < N-1 \end{cases}$$

$$C_{i,j}(s) = \begin{cases} \epsilon_o \epsilon_r(s) \frac{l^2}{d_i} & \text{for } |i-j|=1 \\ 0 & \text{for } |i-j| > 1 \end{cases} \quad (2.8)$$

$$G_{i,j}(s) = \omega C_{i,j}(s) \tan \delta_i$$

$$R_{i,j} = \begin{cases} R_i & \text{for } i = j \\ 0 & \text{for } i \neq j \end{cases}$$

$$\hat{R}_{i,j}(s) = \begin{cases} \hat{R}_i(s) & \text{for } i = j \\ 0 & \text{for } i \neq j \end{cases} \quad (2.9)$$

where $L_{i,j}$, $C_{i,j}$, $G_{i,j}$, $R_{i,j}$ and $\hat{R}_{i,j}$ represent the coupling term between the i^{th} and j^{th} plane for $1 \leq i, j \leq N-1$ and N represents the total number of PDN layers (i.e. $N = 4$ for Fig. 2-4). It is noted that (2.7) represent the transverse coupling due to the magnetic flux and (2.8) represents the transverse coupling due to the electric field through the dielectric.

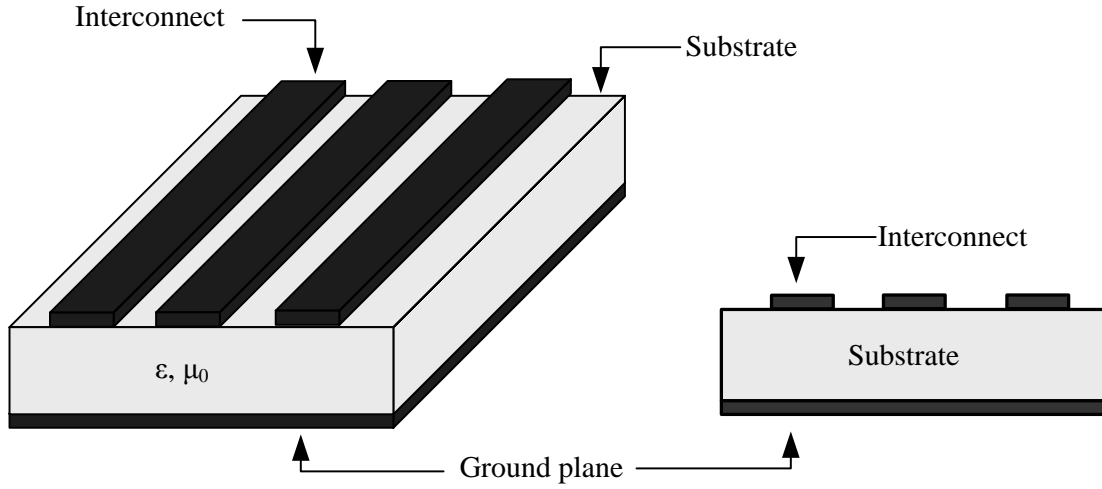


Figure 2-5: Three-dimensional and cross sectional views of an interconnect structure.

Overall, (2.7)-(2.9) provides a generalized quantification of the coupling of any general N layered PDN. Based on (2.7)-(2.9), the equivalent lumped π -model representing each unit cell is illustrated in Fig. 2-4(b) [37] where each of the Z and Y blocks of Fig. 2-4(b) is realized in SPICE using a lumped RL and RC network respectively [5].

For the accurate modeling of the distributed nature of PDNs, the geometric dimensions of each unit cells of Fig. 2-1(b) (single layered PDNs) and Fig. 2.4(a) (multilayered PDNs) has to be very small compared to the PDN dimensions. This leads to very large modified nodal analysis (MNA) matrices representing the PDN when realized using commercial circuit simulators like SPICE. Furthermore, realization of the frequency dependent parameters of (2.7)-(2.9) using lumped RL/RC ladder networks as proposed in [5], [37] will lead to introduction of additional nodes and further augmentation of the MNA matrices. Thus, computational costs of modeling PDNs are typically expensive and alternative methodologies for efficient modeling of PDNs are still being investigated.

2.4 High Speed Interconnect Modeling

Figure 2-5 shows the physical structure of a typical interconnect network. The complexity of the interconnect macromodel depends on the physical dimensions and operating frequency of the circuit. For cases where the minimum wavelength of the travelling electromagnetic wave through the medium is comparable with the cross sectional dimensions of the interconnect network, full wave models are required. On the other hand, as long as the minimum wavelength of the travelling electromagnetic wave is much larger than the cross sectional dimensions of the interconnect network, a TEM mode of propagation is the dominant mode of wave propagation. In TEM mode of propagation, the electric and magnetic fields surrounding the space around the line conductors are transverse or perpendicular to the line axis and to each other [1]. TEM mode exists for transmission lines with homogenous medium and perfect conductors. In inhomogeneous mediums, electromagnetic waves are generated with different velocities. Moreover, interconnect networks with imperfect conductors produce electric fields along the surface conductor. Such interconnect structures violate the TEM wave characteristics, since TEM waves propagate with only one velocity and have no electric field along the surface conductor. However, for many lossy interconnects in presence of inhomogeneous medium, the results are almost similar to TEM structures and thus they can be approximated as TEM mode, referred as quasi-TEM assumptions. One of the important characteristics of TEM mode of propagation (which is approximated for non-perfect conductors in quasi-TEM modes) is the ability of expressing the voltage and current values of each point of the conductor line using the Telegrapher's equations, as below

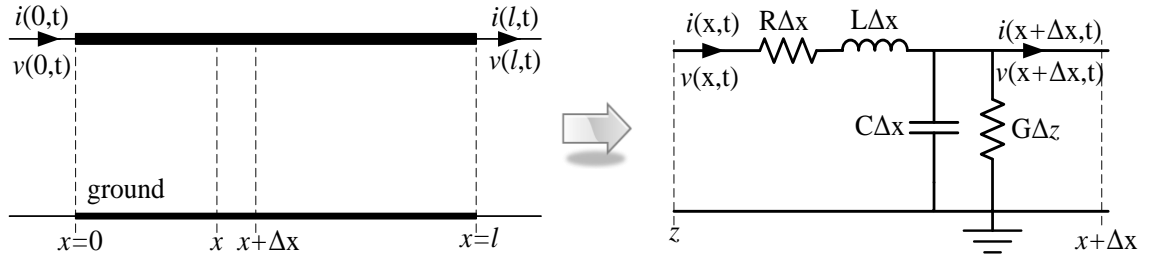


Figure 2-6: Lumped transmission line model for single transmission line.

$$\frac{\partial}{\partial x} \begin{bmatrix} \mathbf{V}(x, s) \\ \mathbf{I}(x, s) \end{bmatrix} = \begin{bmatrix} \mathbf{0} & -(\mathbf{R}(s) + s\mathbf{L}(s)) \\ -(\mathbf{G}(s) + s\mathbf{C}(s)) & \mathbf{0} \end{bmatrix} \begin{bmatrix} \mathbf{V}(x, s) \\ \mathbf{I}(x, s) \end{bmatrix} \quad (2.10)$$

where x is the position variable along the axis of the conductors; $\mathbf{V}(x, s)$ and $\mathbf{I}(x, s)$ represent the spatial distribution of voltage and current vectors of the multi-conductor transmission lines (MTLs) respectively; $\mathbf{R}(s)$, $\mathbf{L}(s)$, $\mathbf{G}(s)$ and $\mathbf{C}(s)$ are the frequency dependent per unit length (p.u.l.) resistance, inductance, conductance and capacitance matrices, respectively. The p.u.l. parameter matrices can be determined by a can be obtained from a static solution of the Laplace equation in the 2-D plane containing the cross section of the conductors of Fig. 2-5 [1]. The difficulty with modeling of interconnects using (2.10) is that they cannot be directly linked to circuit simulators such as SPICE. This is because typical circuit simulators solve nonlinear ordinary differential equations (ODEs) while Telegrapher's equations are expressed as PDEs. To overcome this difficulty, numerical techniques are used to convert distributed models into ODEs as explained in detail in the next subsection.

2.5 Simulating Interconnects in SPICE-like Simulators

For the case when the physical characteristics of the interconnect structure is known and quasi-TEM is assumed, the electrical performance of interconnects can be expressed using the Telegrapher's partial differential equations (PDE). Commercial circuit simulators like SPICE being unable to solve the PDE's in the time domain, macromodeling algorithms are required to convert the PDE to ordinary differential equations (ODE) which can be solved by numerical integration. Moreover, macromodeling algorithms can also be extended to perform EMI analysis due to incident field coupling to lossy transmission lines. The following sections describe some of the existing macromodeling techniques based on quasi-TEM mode of propagation, followed by a review of incident field analysis.

2.5.1 Lumped Segmentation

Lumped segmentation technique uses lumped equivalent circuits of the transmission lines to approximate Telegrapher's equations. Applying Euler's method [1] to (2.10) yields

$$\begin{bmatrix} V(x + \Delta x, s) - V(x, s) \\ I(x, s) - I(x + \Delta x, s) \end{bmatrix} = \Delta x \begin{bmatrix} \mathbf{0} & -(\mathbf{R}(s) + s\mathbf{L}(s)) \\ -(\mathbf{G}(s) + s\mathbf{C}(s)) & \mathbf{0} \end{bmatrix} \begin{bmatrix} V(x, s) \\ I(x, s) \end{bmatrix} \quad (2.11)$$

where $x=[1,2,\dots,\eta]$, $\Delta x=l/\eta$, η is the number of sections and l is the length of interconnect. Equation (2.11) can be implemented by lumped equivalent circuit composed of resistors, inductors and capacitors as shown in Fig. 2-6. In order to ensure that the discretization of (2.11) is accurate, the value of Δx has to be very small. The basic rule of thumb to determine the value of Δx is to ensure that the number of segments (n) satisfy the following condition

$$n = 20 \frac{l \cdot \sqrt{LC}}{t_r} \quad (2.12)$$

where t_r is the rise/fall time. The lumped segmentation model is passive and provides a direct method to discretize (2.10). However as the rise time of signal shortens with VLSI technology and/or if the interconnect is electrically long, many lumped elements are required for an accurate model. This leads to large MNA matrices thereby increasing the simulation time.

2.5.2 Matrix Rational Approximation

Matrix rational approximation (MRA) macromodel directly converts the Telegrapher's equations into time domain macromodels based on analytic rational approximations of exponential matrices [24]-[25]. An important feature of the MRA macromodel is that it is passive by construction. To describe this macromodeling algorithm, the solution of (2.10) can be written in the Laplace-domain as an exponential matrix function as

$$\begin{bmatrix} \mathbf{V}(l,s) \\ \mathbf{I}(l,s) \end{bmatrix} = e^{\mathbf{Z}} \begin{bmatrix} \mathbf{V}(0,s) \\ \mathbf{I}(0,s) \end{bmatrix}$$

$$\mathbf{Z} = \begin{bmatrix} \mathbf{0} & -(\mathbf{R}(s) + s\mathbf{L}(s)) \\ -(\mathbf{G}(s) + s\mathbf{C}(s)) & \mathbf{0} \end{bmatrix} \cdot l \quad (2.13)$$

where l is the length of the transmission line. The exponential matrix $e^{\mathbf{Z}}$ in (2.13) can be expressed with a matrix rational approximation as

$$\mathbf{P}_M(\mathbf{Z})e^{\mathbf{Z}} = \mathbf{Q}_N(\mathbf{Z}) \quad (2.14)$$

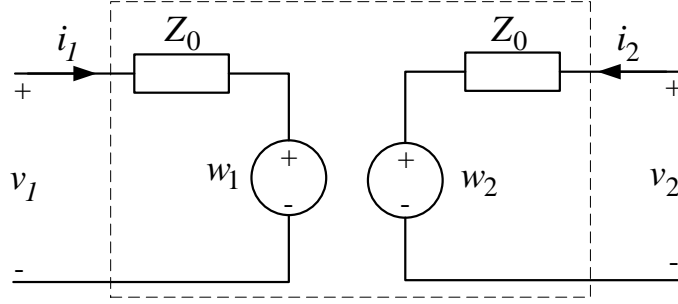


Figure 2-7: Circuit realization of MoC for a two-conductor transmission line.

where $\mathbf{P}_M(\mathbf{Z})$ and $\mathbf{Q}_N(\mathbf{Z})$ are polynomial matrices

$$\begin{aligned}\mathbf{P}_M(\mathbf{Z}) &= \sum_{i=0}^M p_i \mathbf{Z}^i = \sum_{i=0}^M \frac{(2M-i)!M!}{(2M)!i!(M-i)!} \mathbf{Z}^i \\ \mathbf{Q}_N(\mathbf{Z}) &= \sum_{i=0}^N q_i \mathbf{Z}^i = \sum_{i=0}^N \frac{(2N-i)!N!}{(2N)!i!(N-i)!} \mathbf{Z}^i\end{aligned}\quad (2.15)$$

After some mathematical manipulations, the results of (2.15) can be used to obtain a macromodel represented by a set of ordinary differential equations, in a closed form manner [24]-[25]. Since the MRA macromodel is described in terms of predetermined coefficients p_i and q_i , and the p.u.l parameters, the macromodel can be constructed very quickly. While the MRA macromodel has been proved to be highly efficient for interconnects with small line length, it is not very computationally efficient for electrically long lines since the delay of the transmission line is not extracted. Hence, for long lines, a higher order of approximation is required to express $e^{\mathbf{Z}}$ as a matrix rational approximation. In the following subsections two common delay extraction macromodels are reviewed that addresses the computational constraint of such lumped model.

2.5.3 Method of Characteristics

Among the most commonly used algorithms are those based on the generalized method of characteristics (MoC). The MoC extracts the line-propagation delay and produce exact models when applied to lossless transmission lines [26]. Over the years, these algorithms have been extended to model lossy MTLs [27]-[30]. The efficiency of MoC is derived by extracting the propagation delay which allows the attenuation function to be approximated with a low-order rational function. This significantly reduces the computational complexity of the transfer function; especially for long lines with low losses.

The original method of characteristics [26] is able to represent interconnects as ODEs containing time delays. Although the original method of characteristics was developed in the time-domain using what is referred as characteristic curves (hence the name), a simpler alternative derivation in the frequency-domain is presented. The frequency domain solution of (2.13) for a two-conductor transmission line is

$$\begin{bmatrix} I_1 \\ I_2 \end{bmatrix} = \frac{1}{Z_0(1 - e^{-2\gamma l})} \begin{bmatrix} 1 + e^{-2\gamma l} & -2e^{-\gamma l} \\ -2e^{-\gamma l} & 1 + e^{-2\gamma l} \end{bmatrix} \cdot \begin{bmatrix} V_1 \\ V_2 \end{bmatrix}$$

$$\gamma = \sqrt{(G + sC)(R + sL)}$$

$$Z_0 = \sqrt{(R + sL)/(G + sC)} \quad (2.16)$$

where γ is the propagation constant and Z_0 is the characteristic impedance. After some mathematical manipulations, the terms in (2.16) can be expressed as

$$\begin{aligned} V_1 &= Z_0 I_1 + W_1; \\ V_2 &= Z_0 I_2 + W_2 \end{aligned} \quad (2.17)$$

where W_1 and W_2 are defined as recursive relations

$$\begin{aligned} W_1 &= e^{-\gamma l} [2V_2 - W_2]; \\ W_2 &= e^{-\gamma l} [2V_1 - W_1] \end{aligned} \quad (2.18)$$

For lossless transmission lines, γ and Z_0 can be reduced to

$$\gamma = s\sqrt{LC}; \quad Z_0 = \sqrt{L/C} \quad (2.19)$$

which makes γ a purely imaginary number and Z_0 a real constant. The time domain solution of MoC can be obtained by taking the inverse Laplace transform of (2.17) and (2.18) as

$$\begin{aligned} v_1(t) &= Z_0 i_1(t) + w_1(t); \\ v_2(t) &= Z_0 i_2(t) + w_2(t); \\ w_1(t) &= 2v_2(t - \tau) - w_2(t - \tau); \\ w_2(t) &= 2v_1(t - \tau) - w_1(t - \tau) \end{aligned} \quad (2.20)$$

where $\tau = \gamma l$ is represented as a delay term. An equivalent circuit realization of time domain macromodel of a lossless transmission line is demonstrated in Figure 2-7. For the case of lossy transmission lines, γ is not purely imaginary and Z_0 is not a real constant and therefore, the direct time domain representation is not possible. In this case, numerical techniques have been proposed to incorporate lossy transmission line models [27]-[30] using rational approximation of Z_0 and $e^{-\gamma l}$.

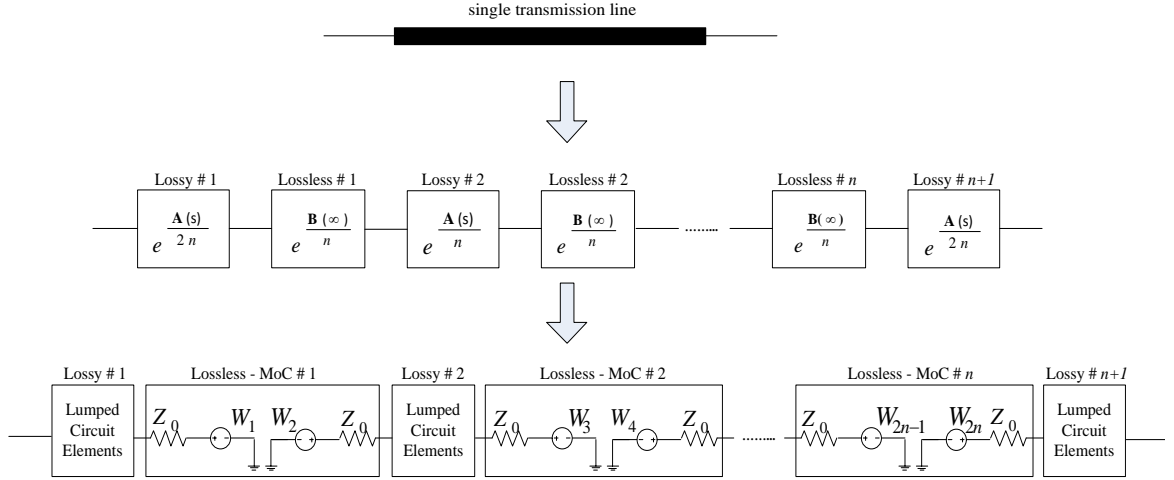


Figure 2-8: Circuit realization of DEFACT macromodel.

2.5.4 Delay Extraction-Based Passive Compact Transmission-Line Macromodeling Algorithm (DEFACT)

Another delay extraction based algorithm is the DEFACT macromodel which, unlike the MoC can be made passive by construction [31]-[32]. To better understand the DEFACT macromodel, the \mathbf{Z} matrix of (2.13) is rewritten as

$$\mathbf{Z} = \mathbf{A} + s\mathbf{B} \quad (2.21a)$$

$$\mathbf{A} = \begin{bmatrix} 0 & -\mathbf{R}(s) - s(\mathbf{L}(s) - \mathbf{L}_\infty) \\ -\mathbf{G}(s) - s(\mathbf{C}(s) - \mathbf{C}_\infty) & 0 \end{bmatrix} \cdot l; \quad \mathbf{B} = \begin{bmatrix} 0 & -\mathbf{L}_\infty \\ -\mathbf{C}_\infty & 0 \end{bmatrix} \cdot l \quad (2.21b)$$

and $\mathbf{L}_\infty = \mathbf{L}(\infty)$ and $\mathbf{C}_\infty = \mathbf{C}(\infty)$ are the extracted p.u.l inductance and capacitance of the line and l represents the line length.

The basic idea of the delay extraction-based passive compact transmission-line (DEPACT) macromodeling algorithm is to separate the extracted delay terms ($e^{s\mathbf{B}}$) from $e^{(\mathbf{A}+s\mathbf{B})}$ thereby enabling $e^{\mathbf{A}}$ to be modeled using a low order rational function. However, this is not a trivial task since the matrices \mathbf{A} and $s\mathbf{B}$ do not commute, (i.e. $e^{(\mathbf{A}+s\mathbf{B})} \neq e^{\mathbf{A}}e^{s\mathbf{B}}$). To approximate $e^{(\mathbf{A}+s\mathbf{B})}$ in terms of a product of exponentials, a modified Lie product [38] is used as

$$e^{\mathbf{A}+s\mathbf{B}} \approx \prod_{i=1}^n \Psi_i + \varepsilon_n \quad (2.22a)$$

$$\Psi_i = e^{\frac{\mathbf{A}}{2n}} e^{\frac{s\mathbf{B}}{n}} e^{\frac{\mathbf{A}}{2n}} \quad (2.22b)$$

where n is the number of sections. The associated error of the approximation scale to the second power of number of sections n , as $\|\varepsilon_n\| \cong O(1/n^2)$ [31] (i.e. (2.22) quickly converges to the exponential matrix of (2.13) with increase of number of sections n). Equation (2.22) shows that the exponential function of (2.13) can be divided into subsections of $e^{\mathbf{A}/2n}$ and $e^{s\mathbf{B}/n}$. The matrix $e^{\mathbf{A}/2n}$ represents a lossy line segment and $e^{s\mathbf{B}/n}$ represents a lossless line segment and the product of the two can be viewed as a cascade of transmission line subnetworks [31], [32]. For a two-conductor transmission line example, each Ψ_i in (2.22) can be realized as shown in Figure 2-8. Here, the lossy terms can be macromodeled using the MRA algorithm (section 2.5.2) and the lossless sections can be modeled using the MoC approach (section 2.5.3). The resulting macromodels are of significant lower orders since for electrically long lines a significant portion of the delay is already extracted using MoC [31]. It is however noted that the accuracy of the Lie approximation of (2.22) is dependent on the line losses, the line

length and the maximum frequency of operation [31]. As these parameters increases, the number of sections, n needs to be increased to obtain a more accurate approximation of (2.13) and consequently may still leads to large macromodels for simulation.

2.5.5 Transmission Line Macromodels with Incident Fields

With the increasing packaging density, proliferation of low powered devices and scaling of the supply voltage, susceptibility of interconnects to external electromagnetic fields is a major issue for signal integrity analysis. For this reason, the analysis of transmission lines excited by an external electromagnetic wave has been an active area of research [4]-[39]-[52]. Majority of the works are based on the formulation given by Taylor in [39] which is applicable for two-conductor transmission lines. The technique is also expanded for frequency domain solution of excited MTLs in [40] and later for the time domain solutions in [41]-[42]. In these formulations, the excited transmission line model is composed of two parts: i. an unexcited transmission line and ii. forcing functions at the terminals of the transmission lines modeling the effects of the incident field. These techniques are based on the quasi-TEM mode of propagation along the transmission line. In [48]-[52], the analysis of MTLs in the presence of an incident field has been evaluated using various macromodeling techniques such as MRA, DEFACT and a passive MoC algorithm to name a few.

2.6 Waveform Relaxation for Parallel Simulation

It is observed from the above discussion that interconnect networks can not only consist of large number of coupled conductors but also for segmentation based macromodeling techniques (of Section 2.5.1 or Section 2.5.2) may require large number of segments for long line lengths, high frequency of operations and large p.u.l. parameters values. As a result, simulation costs of interconnect networks are typically very large. One technique to curb the computational costs is based on model order reduction techniques [23]. In this thesis an alternative technique based on parallel simulation of large networks, referred to as waveform relaxation technique, is discussed.

Waveform relaxation, from its introduction in [53], has proven to be an attractive algorithm to address the issue of exorbitant computational costs for solving large networks using traditional circuit solvers like SPICE. The algorithm is based on partitioning large networks into smaller subcircuits where the coupling between the subcircuits is represented using time domain lumped sources introduced (hereafter referred to as ‘relaxation sources’) into each subcircuit. Assuming an initial guess for the waveforms of the relaxation sources, the subcircuits are solved independently. The present solution of the subcircuits is then used to update the relaxation sources for the next iteration. This process is repeated until the error between two successive iterations falls within a prescribed error tolerance. Solving the individual subcircuits using modern parallel processing resources has allowed the utilization of multiprocessor hardware and provided significant CPU savings in memory and time compared to traditional full circuit simulation [54]. It is noted that the main limitation of relaxation algorithms is the speed of convergence of the iterations. Several methods have been reported to speed up

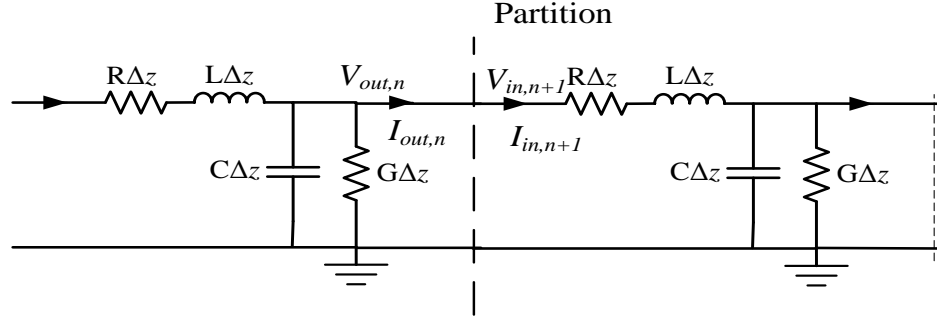


Figure 2-9: Longitudinal partitioning of transmission line using lumped RLGC model.

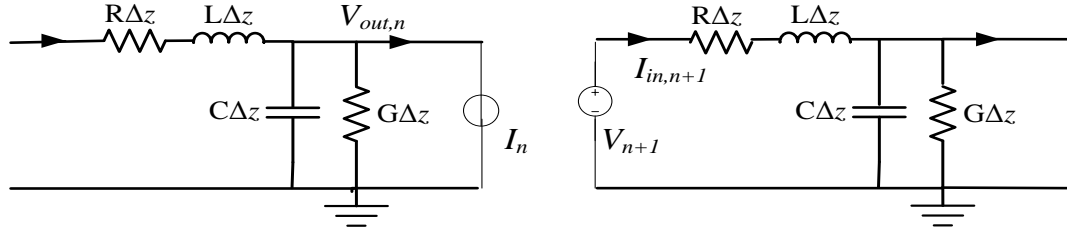


Figure 2-10: Subcircuits generated from Figure 2.9 for single transmission line (no optimization).

convergence, such as time windowing [55], overlapping subdomains [56]-[57] and optimization [58].

In the existing literature, WR algorithms have been successfully implemented for large interconnect networks using two different approaches – transverse partitioning based WR (TP-WR) and longitudinal partitioning based WR (LP-WR). Typically, transverse partitioning techniques attempt to partitioning MTL networks into single lines based on an assumption of weak inductive and capacitive coupling between the lines [54], [59]-[63]. On the other hand, LP-WR attempt to partition the length of the line into smaller sections where each section can now be realized using a particular model outlined in

Section 2.5 [58], [64]-[68]. Hence, TP-WR is very efficient for modeling of MTLs with large number of conductors while LP-WR has been found to be very efficient for modeling of MTLs with electrically long line lengths. Two typical LP-WR algorithms are reviewed next.

2.6.1 Optimization based LP-WR

Consider a single line interconnect modeled using the lumped RLGC methodology of Section 2.5.1. The partitioning between two adjacent lumped sections is illustrated in Fig. 2-9. As a result of this partitioning scheme, the entire line length can be divided into n subcircuits where n is the number of RLGC sections of (2.12). In order to preserve the continuity in the current and voltage waveforms on either side of the partition of Fig. 2-9, the coupling between the subcircuits can be described by the following Dirichlet's transmission condition where the quantities on either side of the equation are relaxed by an iteration count.

$$I_n^{(k+1)}(t) = I_{in,n+1}^{(k)}(t); V_{n+1}^{(k+1)}(t) = V_{out,n}^{(k)}(t) \quad (2.23)$$

where the superscript refers to the iteration count. The equivalent circuit representation of (2.23) is shown in Fig. 2-10. Once this partitioning has been performed, an initial guess of the relaxation sources $(I_i^{(0)}(t), V_i^{(0)}(t))$ is assumed to begin the iterations and the n partitioned subcircuits can now be solved in parallel. Once any k^{th} iteration is over, the relaxation sources can be updated using (2.23) for the $k+1^{\text{th}}$ where the quantities in the right hand side are known from the k^{th} iteration.

However, longitudinal partitioning techniques based on segmentation models have a common limitation that since each segment is cascaded with the next, the Dirichlets

transmission condition of (2.23) is required to preserve the current/voltage waveform at the boundary of the subcircuits and this leads to slow convergence of the WR iterations [58]. In order to address this problem, the work of [58] developed an optimization based constraint for updating the relaxation sources which is mathematically expressed as

$$\begin{aligned} I_n^{(k+1)}(t) + \alpha V_{out,n}^{(k+1)}(t) &= I_{in,n+1}^{(k)}(t) + \alpha V_{in,n+1}^{(k)}(t); \\ V_{n+1}^{(k+1)}(t) + \beta I_{in,n+1}^{(k+1)}(t) &= V_{out,n}^{(k)}(t) + \beta V_{out,n}^{(k)}(t) \end{aligned} \quad (2.24)$$

It can be seen that according to (2.24), the Dirichlet's transmission condition of (2.23) has been replaced by an alternative condition where additional information is exchanged between the subcircuits per iteration. The idea behind [58] is that the values of the scalar weights α and β can be optimized *a priori* so as to artificially accelerate the convergence of WR iterations as explained in detail in [58]. It is to be noted however, that the value of these weights are problem dependent and may need to re-evaluated for changes in the interconnect structure. Another such efficient LP-WR algorithm based on the MoC is explained next.

2.6.2 MoC based LP-WR

Consider a single line interconnect modeled using the MoC methodology of Section 2.5.3. An attractive feature of the MoC is that there exists a natural disjoin between the left and right halves of the macromodel as illustrated in Fig. 2-7 where the two halves of the macromodel are coupled through the W sources of (2.18). As a result, there is no need to preserve the current or voltage waveforms across the partitioning interface (i.e. the Dirichlet's transmission condition is no longer applicable). This ensures that the subcircuits of Fig. 2-7 are weakly coupled and that the WR converge naturally and efficiently [64].

The iterative solution of two halves of the MoC macromodel (of Fig. 2-7) begins with a initial guess of the relaxation sources ($W_1^{(0)}(t)$, $W_2^{(0)}(t)$). Once the two subcircuits of the MoC macromodel have been solved for any general k^{th} iteration is over, the relaxation sources can be updated using a relaxed version of the MoC delayed equations (2.20) as

$$\begin{aligned} w_1^{(k+1)}(t) &= 2v_2^{(k)}(t - \tau) - w_2^{(k)}(t - \tau); \\ w_2^{(k+1)}(t) &= 2v_1^{(k)}(t - \tau) - w_1^{(k)}(t - \tau) \end{aligned} \quad (2.25)$$

where all the waveforms of the right hand side are known from the k^{th} iteration [64]. It is observed that despite the efficient convergence of the WR iterations using (2.25), for lossy MTL networks, the problem of passivity of the MoC macromodel still exists. This has limited the application of MoC based WR algorithms for SPICE simulation.

Besides interconnect networks, WR algorithms can also be applied to PDNs [69]. However, the typical WR based parallel simulation of PDNs of [69] is based on lumped RC models and are applicable for on-chip structures. As a result, sophisticated distributed PDN models for large package/board power bus examples that can include the distributed effects are still under investigation.

Chapter 3

3 Transient Simulation of Distributed Networks using Delay Extraction based Numerical Convolution

3.1 Introduction

This chapter presents a delay extraction based IFFT technique for the macromodeling of distributed networks characterized by their frequency domain, multiport Y parameter data [21]. The proposed algorithm uses time-frequency decompositions to extract multiple propagation delays of a distributed network. Based on the knowledge of the delays, the associated attenuation losses can be quantified in a piecewise manner using the Hilbert transform. As a result, in the time domain, the transfer function is represented as a sum of delayed time domain responses. Numerical examples illustrate that the proposed algorithm shows significantly more accurate results for networks with multiple long delays when compared to existing numerical convolution techniques.

3.2 Motivation and Review of General Time-Frequency Decompositions

3.2.1 Motivation

For ease of presentation, it is assumed that the tabulated data of any general multiport network is described in terms of the Y parameters as

$$Y(s) = [Y_{ij}(s)]; \quad (i, j \in 1, \dots, P) \quad (3.1)$$

where

$$Y_{ij}(s) = \sum Y_{ij}^{(k)}(s) e^{-sT_{k,ij}} \quad (3.2)$$

and $T_{k,ij}$ is the k^{th} propagation delay, $Y_{ij}^{(k)}(s)$ is the attenuation losses corresponding to the k^{th} propagation delay, ‘ s ’ represents the Laplace variable, $[0:F_{\max}]$ is the bandwidth of interest and P is the number of ports of the network. The time domain representations of Y parameters of (3.1) are

$$Y_{ij}(t) = \sum Y_{ij}^{(k)}(t - T_{k,ij}) \quad (3.3)$$

where $Y_{ij}^{(k)}(t)$ is the inverse Fourier transform of $Y_{ij}^{(k)}(s)$. Evaluating $Y_{ij}(t)$ using direct IFFT on the $Y_{ij}(s)$ without delay extraction results in errors in early time [19], [21] leading to inaccurate signal integrity verification such as eye diagram simulations [19]. One approach to reduce these errors is to extract the dominant propagation delay of the system [19], as

$$Y_{ij}(s) = H_{ij}(s) e^{-sT_{ij}} \quad (3.4)$$

where T_{ij} is the dominant propagation delay (i.e. minimum propagation delay) and $H_{ij}(s)$ correspond to the attenuation losses of the overall system. This approach produces accurate results when the system is characterized by a single dominant delay (i.e. where $H_{ij}(s)$ is a minimum phase response and can be extracted using a Hilbert transform of $Y_{ij}(s)$) as illustrated in [19]. For networks characterized by multiple delays, extraction of the dominant delay $T = T_{0,ij}$ allows $H_{ij}(s)$ to be expressed as

$$H_{ij}(s) = \sum Y_{ij}^{(k)}(s) e^{-s(T_{k,ij} - T_{0,ij})} \quad (3.5)$$

Provided the delays are closely spaced, the phase contribution of all $e^{-s(T_{k,ij} - T_{0,ij})}$ is relatively small. As a result, $H_{ij}(s)$ can still be approximated as a minimum phase response and accurately evaluated by applying Hilbert transform on (3.4) using (2.3)-(2.4). However, this methodology of evaluating the attenuation losses may not yield accurate results for the case of a general distributed network with multiple delays which are not grouped close together (i.e. where the phase contribution of $e^{-s(T_{k,ij} - T_{0,ij})}$ is non-negligible) [36]. Thus, application of the Hilbert transform blindly to (3.4) may lead to inaccurate approximation of $H_{ij}(s)$ [36].

In order to address the above issues, a methodology to extract multiple delays for generalized distributed networks using the time-frequency techniques is proposed. The next section briefly reviews the general class of time-frequency decomposition techniques to better explain the proposed algorithm.

3.2.2 General Time-Frequency Decompositions

The time-frequency decompositions are a class of transformations from a one

dimensional function, say $Y_{ij}(s)$, to a two dimensional function $F_{ij}(\omega, \tau)$ that measures the variance of the function with respect to both frequency (ω) and time (τ) variables. The time-frequency transform of $Y_{ij}(s)$ is defined as [70]-[71]:

$$F_{ij}(\omega, \tau) = \int_{-\infty}^{\infty} Y_{ij}(\zeta) W(\zeta - \omega) e^{j\zeta\tau} d\zeta \quad (3.6)$$

where $F_{ij}(\omega, \tau)$ is the two dimensional inverse Fourier transform function, ω and τ are the angular frequency and time variables respectively, $W(\zeta - \omega)$ a window centered at $\zeta = \omega$ of prescribed width L and $s = j\zeta$ represents a simple transformation of variable. The integral of (3.6) provides a mechanism to filter sections of $Y_{ij}(s)$ using an arbitrary window as it sweeps the frequency axis within the prescribed bandwidth of interest, and take the inverse Fourier transform of each section individually. In this work, $W(\zeta - \omega)$ represents a Gaussian window which corresponds to a Gabor transform and provides optimal support in both the time and frequency domains [70]-[71]. The window width (or the standard deviation) can be chosen using the methodologies of [72]-[73]. For the examples of this paper, the window sizes used are determined using the procedure of [73]. The energy of the function $F_{ij}(\omega, \tau)$ can be calculated as

$$\eta_{ij}(\tau) = \int_{-\infty}^{\infty} |F_{ij}(\omega, \tau)|^2 d\omega \quad (3.7)$$

The $\eta_{ij}(\tau)$ of equation (3.7) is a one dimensional function localizing the variation of energy of $F_{ij}(\omega, \tau)$ with time and provides a method to extract propagation delays embedded in any frequency domain data [14]-[15]. The inverse of (3.6) exists [69]-[71] and can be expressed as

$$Y_{ij}(\zeta) = \frac{1}{2\pi} \int_{-\infty}^{\infty} \int_{-\infty}^{\infty} F_{ij}(\omega, \tau) W(\zeta - \omega) e^{-j\omega\tau} d\omega d\tau \quad (3.8)$$

The reconstruction of $Y_{ij}(\zeta)$ in (3.8) can also be done in a piecewise manner by separating the time-frequency plane of (ω, τ) into smaller regions Ω_m , and performing the integral of (3.8) over each region as

$$Y_{ij}(\zeta) = \sum_{m=1} \tilde{Y}_{ij}^{(m)}(\zeta) \quad (3.9)$$

$$\tilde{Y}_{ij}^{(m)}(\zeta) = \frac{1}{2\pi} \int \int_{\Omega_m} F_{ij}(\omega, \tau) W(\zeta - \omega) e^{-j\omega\tau} d\omega d\tau \quad (3.10)$$

$$\bigcup_{m=1} \Omega_m = \Re^2 \quad (3.11)$$

where the summation of each integral of (3.10) over the suitable chosen Ω_m area leads to the piecewise reconstruction of $Y_{ij}(\zeta)$. The time-frequency techniques of (3.6)-(3.11) provide a mechanism to extract the delays and the associated losses from the data for general multiple delay networks.

3.3 Development of the Proposed Algorithm

The objective of this work is to use the time-frequency decompositions to predetermine the delays $T_{k,ij}$ and the corresponding attenuation loss components $Y_{ij}(s)$ in order to evaluate the components of (3.1).

3.3.1 Determining Multiple Delays (T_k)

To determine the propagation delays $T_{k,ij}$, the transform of (3.6) is used to convert the tabulated data of $Y_{ij}(s)$ to the time-frequency domain representation of $F_{ij}(\omega, \tau)$ and to obtain the energy distribution of $\eta_{ij}(\tau)$ using (3.7). From the resultant energy distribution

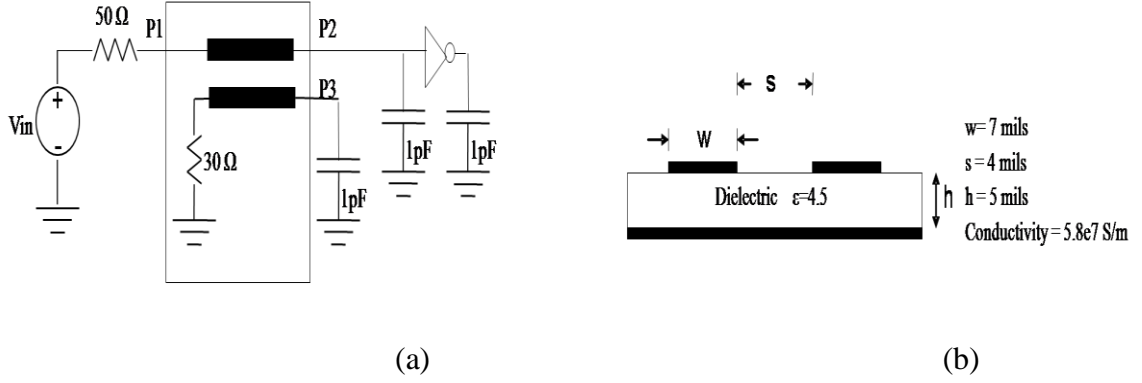


Figure 3-1: Circuit layout of illustrative example. (a) Circuit layout. (b) Geometric layout

$\eta_{ij}(\tau)$, the delays will appear as sharp peaks with significant energy contributions. To illustrate how the delays are evaluated, consider the example of Fig. 3-1(a) where the physical layout of the interconnect network is described in Fig. 3-1(b) and the details of this example is provided in Example 1 of Section 3.4 (also shown in [21]). This example consists of a three port ($P1$ - $P2$ - $P3$) subnetwork consisting of coupled interconnects and terminated with a nonlinear CMOS 180 nm inverter. The three port network is characterized by its tabulated data in terms of the Y parameters up to 3.5 GHz. Identification of the delays are determined by firstly evaluating the energy content of local peaks of $\eta_{ij}(\tau)$ as

$$\hat{\eta}_{ij}^{(k)} = \frac{1}{2\pi} \int_{\tau_{k-1}}^{\tau_k} \eta_{ij}(\tau) d\tau \quad (3.12)$$

where τ_{k-1} and τ_k are time points corresponding to local minimums of $\eta_{ij}(\tau)$ bounding the k^{th} local maxima of $\eta_{ij}(\tau)$. All local maximums with relative energy contributions below a predefined tolerance ϵ

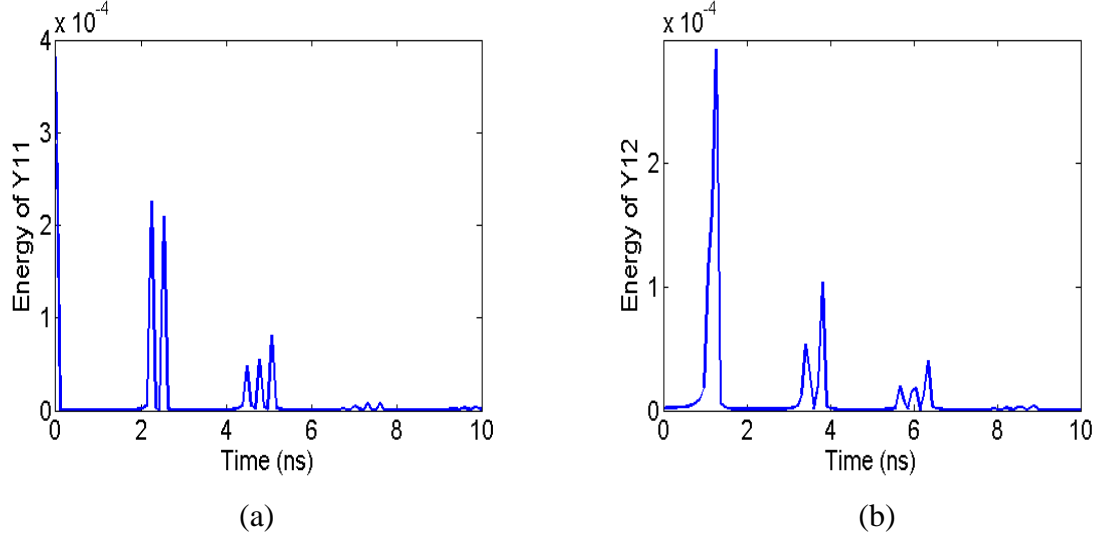


Figure 3-2: Evaluating delay peaks of Example 1. (a) Energy of $|Y_{11}|$ ($\eta_{11}(\tau)$).
(b) Energy of $|Y_{12}|$ ($\eta_{12}(\tau)$) .

Table 3-1: Identified Delays (Example 1)

Delays (ns)	Y_{11}	Y_{12}
T_1	2.25	1.27
T_2	2.54	3.42
T_3	4.49	3.81
T_4	4.79	5.66
T_5	5.08	6.05
T_6	-	6.35

$$\frac{\hat{\eta}_{ij}^{(k)}}{\sum_k \hat{\eta}_{ij}^{(k)}} < \varepsilon \quad (3.13)$$

are discarded. The value of ε is so chosen such that the energy contribution of the neglected delays does not significantly affect the accuracy of the model and is problem

Table 3-2: Partitioning of the (ω, τ) plane for Example 1

Ω_m regions	Y_{11}	Y_{12}
Ω_1	$0 < \tau < 1.00$ ns	$0 < \tau < 2.25$ ns
Ω_2	$1.00 < \tau < 3.00$ ns	$2.25 < \tau < 4.70$ ns
Ω_3	$3.00 < \tau < 6.00$ ns	$4.70 < \tau < 7.25$ ns

dependent [14]. Fig. 3-2 illustrates the energy functions of $\eta_{11}(\tau)$ and $\eta_{12}(\tau)$ where the peaks of the function with significant energy contribution identified using (3.12)-(3.13) and $\varepsilon = 1e-5$ are quantified in Table 3-1.

3.3.2 Partitioning the Time-Frequency Plane

The proposed methodology seeks to represent the frequency contribution of a single or a group of delay peaks of $Y_{ij}(s)$ in terms of piecewise functions $\tilde{Y}_{ij}^{(m)}(s)$ using (3.9)-(3.10). In order to evaluate each $\tilde{Y}_{ij}^{(m)}(s)$, the Ω_m region of (3.10) need to be determined. In this work, the partitioning for of the (ω, τ) plane into Ω_m regions is determined by choosing the point τ_k between two adjacent delays $T_{k-1,ij}$ and $T_{k,ij}$ where $\eta_{ij}(\tau = \tau_k)$ is the minima for $T_{k-1,ij} < \tau < T_{k,ij}$. If the value of $\eta_{ij}(\tau = \tau_k)$ is below a certain predefined threshold δ (i.e. $\eta_{ij}(\tau = \tau_k) < \delta$), then the point τ_k is retained as a valid partitioning point, else it is discarded. The value of δ is so chosen such that the valid partitioning point ($\tau = \tau_k$) can effectively separate the energy contributions of two adjacent delays $T_{k-1,ij}$ and $T_{k,ij}$ from each other, thereby allowing a piecewise decomposition of $Y_{ij}(\zeta)$. For a given predefined threshold δ , the Ω_m regions are expressed as

$$\Omega_m \in \{(\omega, \tau) : 0 \leq \omega \leq 2\pi F_{\max}, t_k \leq \tau \leq t_{k+1}\} \quad (3.14)$$

For the example of Fig. 3-1, the Ω_m regions, evaluated using $\delta = 1e-6$, are shown in Table 3-2.

3.3.3 Computing the Attenuation Losses ($Y_{ij}^{(k)}(s)$)

Once the Ω_m regions are determined, the integral of (3.10) allows a piecewise reconstruction of the frequency domain data. For the case where there is only one identified delay peak in Ω_m , evaluating the integral of (3.10) yields

$$\tilde{Y}_{ij}^{(m)}(s) \approx Y_{ij}^{(m)}(s)e^{-sT_{m,ij}} \quad (3.15)$$

where $T_{m,ij}$ is the extracted delay and $Y_{ij}^{(m)}(s)$ is the the associated attenuation losses within the region Ω_m . For (3.15), taking the Hilbert transform as described by (2.3)-(2.4), the data stream of $Y_{ij}^{(m)}(s)$ can be obtained.

For the case when more than one identified delay exist in the region Ω_m , $\tilde{Y}_{ij}^{(m)}(s)$ can be expressed as

$$\tilde{Y}_{ij}^{(m)}(s) \approx \sum_{n=1}^{N_d} Y_{ij}^{(m,n)}(s)e^{-sT_{m,n,ij}} \quad (3.16)$$

where N_d is the number of delays identified within the Ω_m region which are grouped together. In this case, the attenuation losses $Y_{ij}^{(m,n)}(s)$ cannot be separately evaluated due to the energy spectrum of the delays $T_{m,n,ij}$ overlapping each other. For this scenario (3.16) is approximated as

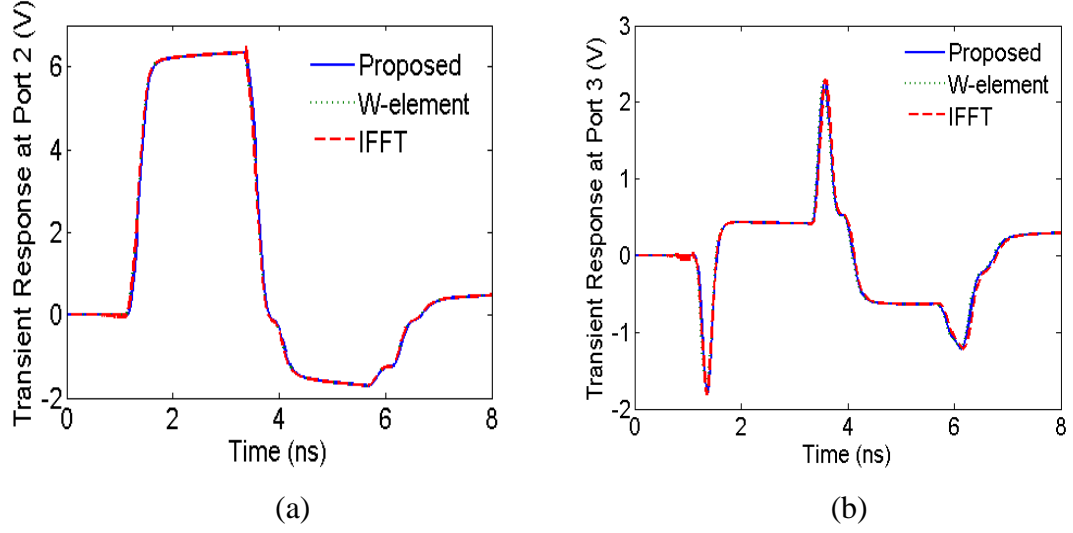


Figure 3-3: Transient response of Example 1 using proposed algorithm, HSPICE's W-element and direct IFFT. (a) Response at P2. (b) Response at P3.

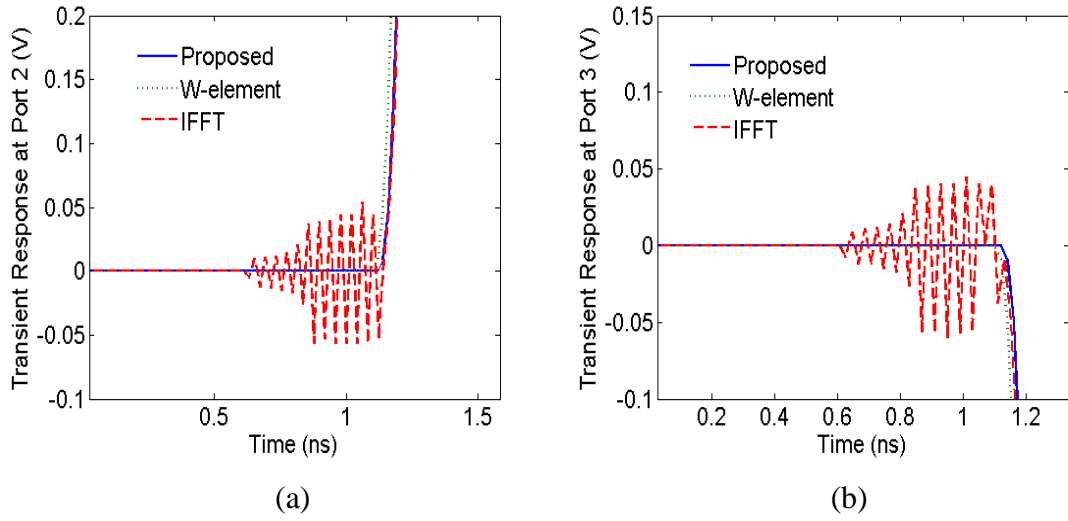


Figure 3-4: Propagation delay capture of Example 1 using the proposed algorithm, HSPICE's W-element and direct IFFT. (a) Response at P2. (b) Response at P3.

$$\begin{aligned}\tilde{Y}_{ij}^{(m)}(s) &= H_{ij}^{(m)}(s)e^{-sT_{m,1,ij}} \\ H_{ij}^{(m)}(s) &= \sum_{n=1}^N Y_{ij}^{(m,n)}(s)e^{-s(T_{m,n,ij}-T_{m,1,ij})}\end{aligned}\quad (3.17)$$

where $T_{m,l,ij}$ is the minimum delay in Ω_m and is already known. Since it is assumed that the delays $(T_{m,n,ij})$ are grouped close together, the phase contribution of all $e^{-s(T_{m,n,ij}-T_{m,l,ij})}$ is relatively small and $Y_{ij}^{(m,n)}(s)$ can be considered as a minimum phase response. Hence, the Hilbert transform as described by (2.3)-(2.4) can still be applied to (3.17) to obtain $H_{ij}^{(m)}(s)$. Once the attenuation loss functions of $Y_{ij}^{(m)}(s)$ or $H_{ij}^{(m)}(s)$ are obtained, they can be easily converted to time domain by an IFFT operation followed by zero padding the data stream to explicitly enforce the $T_{m,ij}$ or $T_{m,l,ij}$ delay respectively.

3.4 Numerical Examples

Three examples are presented in this section to demonstrate the validity of the proposed algorithm (as found in [21]). The proposed algorithm is performed using MATLAB R2008a. In addition, since the examples selected had known structures, the transient responses obtained using proposed model were compared with HSPICE's W-element model [6]. The bandwidth of interest of the examples are determined using the following rule of thumb $F_{max} = 0.35/T_r$ as suggested in [2] where F_{max} is the maximum frequency of interest and T_r is the rise/fall time of the signal.

Example 1: Two Coupled Interconnect Network: A three port network is considered and shown in Fig. 3-1(a) where the physical layout of the network is described in Fig. 3-1(b). The HSPICE field solver is used to obtain the p.u.l. parameters and includes the skin effect losses. The length of the transmission line is set to 20 cm.



Figure 3-5: Two port circuit for Example 2

The network is characterized by its terminal responses (Y parameters) over a bandwidth of 0-3.5 GHz. Using (3.6) and (3.7), the time-frequency transforms of $F_{ij}(\omega, \tau)$ and the energy spectrums of $\eta_{ij}(\tau)$ for all the port-to-port Y -parameters are evaluated. The energy functions of $\eta_{11}(\tau)$ and $\eta_{12}(\tau)$ are shown in Fig. 3-2 and for $\varepsilon = 1e-5$, the delay peaks are identified as shown in Table 3-1. To obtain the attenuation loss responses in terms of sampled data, the (ω, τ) plane of $F_{ij}(\omega, \tau)$ is divided into Ω_m regions for the piecewise integral of (3.10). The results of the partitioning of the time-frequency plane are summarized in Table 3-2.

Once $\tilde{Y}_{ij}^{(m)}(s)$ are evaluated using the integral of (3.10), using the Hilbert transform and enforcing the extracted delays, the terminal responses are described as a sum of delay-causal responses in the time domain. For a trapezoidal input pulse of rise time $T_r = 0.1$ ns and pulse width of 2 ns, the transient responses using the proposed algorithm is shown in Fig. 3-3. In addition, the proposed algorithm is compared with the transient results obtained by directly implementing IFFT on the tabulated data and HSPICE's W-element. It is observed that directly implementing IFFT on band limited data results in a transient response that is not delay-causal as shown in Fig. 3-4. This may result in inaccurate

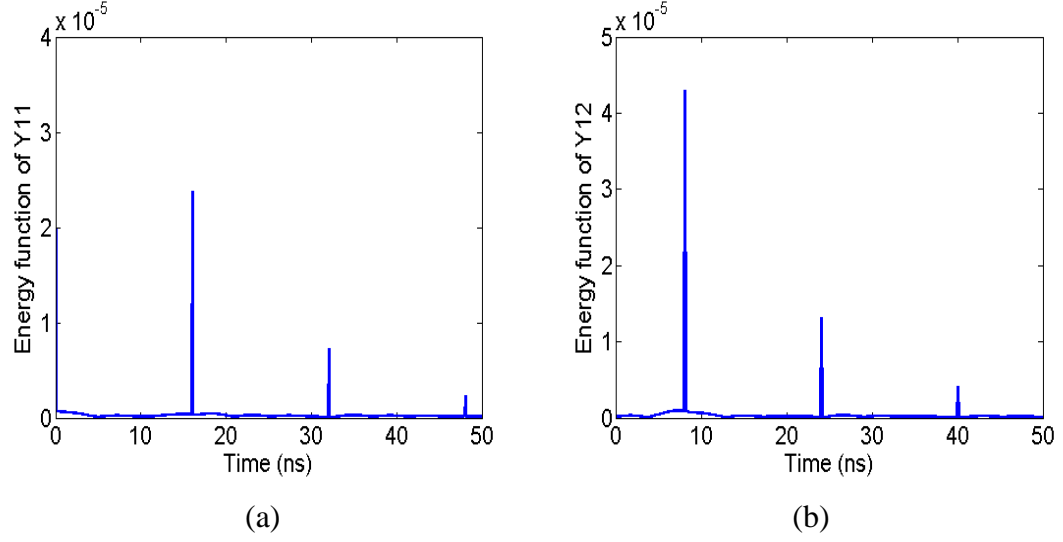


Figure 3-6: Evaluating delay peaks of Example 2. (a) Energy of $|Y_{11}|$ ($\eta_{11}(\tau)$).
(b) Energy of $|Y_{12}|$ ($\eta_{12}(\tau)$) .

signal integrity quantities, such as eye diagram simulations as reported in [19]. However, since the proposed algorithm and HSPICE's W-element model both use delay extraction to obtain the transient response, they provide similar responses.

Example 2: Single Line Network: In order to validate the accuracy of the delay extraction methodology proposed in Section 3.3, a two port example as reported in [13] (Fig. 3-5) is considered. The transmission line network has the resistive, inductive and capacitive p.u.l. parameters of $R = 0.25 \Omega/\text{cm}$, $L = 4\text{nH}/\text{cm}$ and $C = 1.6 \text{pF}/\text{cm}$ respectively and a line length of $l = 100 \text{ cm}$. Hence, the time of flight delay can be analytically determined as $T_0 = l\sqrt{LC}$. Due to mismatch of the termination impedance with the characteristic impedance of the line, the travelling TEM suffers multiple reflections at the near and far end of the network. This leads to multiple delays in the transient response at the near and far ends of the network which can be analytically expressed as [14]

Table 3-3: Comparison of identified delays with the theoretical values of (3.18) for Example 2.

	Y_{11}			Y_{12}		
m	Theoretical Delay ($T_{11}^{(m)}$ (ns))	Observed Delays (T_k (ns))	% Error	Theoretical Delay ($T_{12}^{(m)}$ (ns))	Observed Delays (T_k (ns))	% Error
0	0.00	0.00	0.00	8.00	8.00	0.00
1	16.00	15.98	0.13	24.00	24.02	0.08
2	32.00	31.07	0.22	40.00	39.96	0.10
3	48.00	47.95	0.10	-	-	-

Table 3-4: Partitioning of the (ω, τ) plane for Example 2.

Ω_m Regions	Y_{11}	Y_{12}
Ω_1	$0 < \tau < 8.00$ ns	$0 < \tau < 16.00$ ns
Ω_2	$8.00 < \tau < 24.00$ ns	$16.00 < \tau < 32.00$ ns
Ω_3	$24.00 < \tau < 40.00$ ns	$32.00 < \tau < 48.00$ ns
Ω_4	$40.00 < \tau < 50.00$ ns	-

$$\begin{aligned}
 T_{11}^{(m)} &= 2m * T_0 \\
 T_{12}^{(m)} &= (2m - 1) * T_0; m = \{1, 2, \dots\}
 \end{aligned} \tag{3.18}$$

where $T_{11}^{(m)}, T_{12}^{(m)}$ represent the delays of $Y_{11}^{(m)}, Y_{12}^{(m)}$ respectively and m is an integer. To validate the accuracy of the proposed delay extraction methodology, the network is characterized by its tabulated Y parameters data over a bandwidth of 0-3.5 GHz. Using (3.6) and (3.7), the time-frequency transforms of $F_{ij}(\omega, \tau)$ and the energy spectrums of

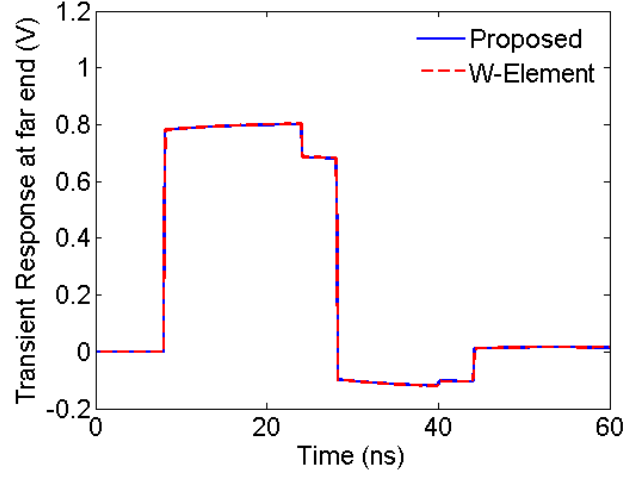


Figure 3-7: Transient response at far end of Example 2.

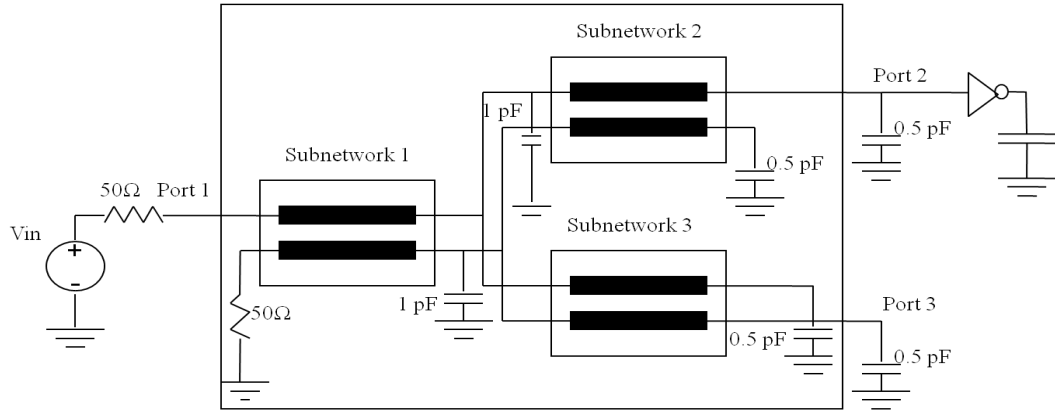


Figure 3-8: Three port circuit for Example 3.

$\eta_{ij}(\tau)$ for all the port-to-port Y -parameters are evaluated. The energy functions of $\eta_{11}(\tau)$ and $\eta_{12}(\tau)$ are shown in Fig. 3-6 and the delays are identified for $\varepsilon = 1\text{e-}5$ as shown in Table 3-3. It is observed from Table 3-3 that the observed delays (T_k) show excellent agreement with the theoretical delay values of (3.18). To obtain the attenuation loss responses in terms of sampled data, the (ω, τ) plane of $F_{ij}(\omega, \tau)$ is divided into Ω_m regions

Table 3-5: Identified Delays (Example 3).

Delays (ns)	Y_{11}	Y_{12}
T_1	2.44	3.22
T_2	2.73	5.57
T_3	4.79	5.96
T_4	5.18	6.84
T_5	5.47	7.13
T_6	6.35	9.28
T_7	7.52	9.57
T_8	7.91	9.86
T_9	9.08	10.45
T_{10}	10.06	10.74
T_{11}	10.35	11.04

for the piecewise integral of (3.10). The results of the partitioning of the time-frequency plane are summarized in Table 3-4. Based on the partitions of Table 3-4 and the methodology outlined in Section 3.3.3, the terminal responses can be converted into a sum of delay-causal responses in the time domain. For a trapezoidal input pulse of rise time $T_r = 0.1$ ns and pulse width of 20 ns, the transient port responses obtained using the proposed algorithm are shown in Fig. 3-7. In addition, the proposed algorithm is compared with the HSPICE W-element model. It is observed that the proposed model gives good agreement with HSPICE's W-element and is similar to those reported in [13].

Table 3-6: Partitioning of the (ω, τ) plane for Example 3

Ω_m Regions	Y_{11}	Y_{12}
Ω_1	$0 < \tau < 1.25$ ns	$0 < \tau < 4.39$ ns
Ω_2	$1.25 < \tau < 3.70$ ns	$4.39 < \tau < 6.55$ ns
Ω_3	$3.70 < \tau < 6.00$ ns	$6.55 < \tau < 7.72$ ns
Ω_4	$6.00 < \tau < 7.00$ ns	$7.72 < \tau < 10.25$ ns
Ω_5	$7.00 < \tau < 8.50$ ns	$10.25 < \tau < 11.00$ ns
Ω_6	$8.50 < \tau < 11.00$ ns	-

Example 3: Cascaded Two Coupled Interconnect Network: A three port example is considered as shown in Fig. 3-8. The linear network consists of three subnetworks, each consisting of two coupled transmission lines. The p.u.l. parameters of the subnetwork 1 are

$$\begin{aligned}
 \mathbf{R} &= \begin{bmatrix} 0.252 & 0 \\ 0 & 0.252 \end{bmatrix} \Omega/cm \\
 \mathbf{L} &= \begin{bmatrix} 3.36 & 0.865 \\ 0.865 & 3.36 \end{bmatrix} nH/cm \\
 \mathbf{C} &= \begin{bmatrix} 1.29 & -0.197 \\ -0.197 & 1.29 \end{bmatrix} pF/cm \\
 \mathbf{G} &= 0 mho/cm
 \end{aligned}$$

and that of subnetwork 2 and 3 are

$$\begin{aligned}
 \mathbf{R} &= \begin{bmatrix} 0.34 & 0 \\ 0 & 0.34 \end{bmatrix} \Omega/cm \\
 \mathbf{L} &= \begin{bmatrix} 4.76 & 1.1 \\ 1.1 & 4.76 \end{bmatrix} nH/cm
 \end{aligned}$$

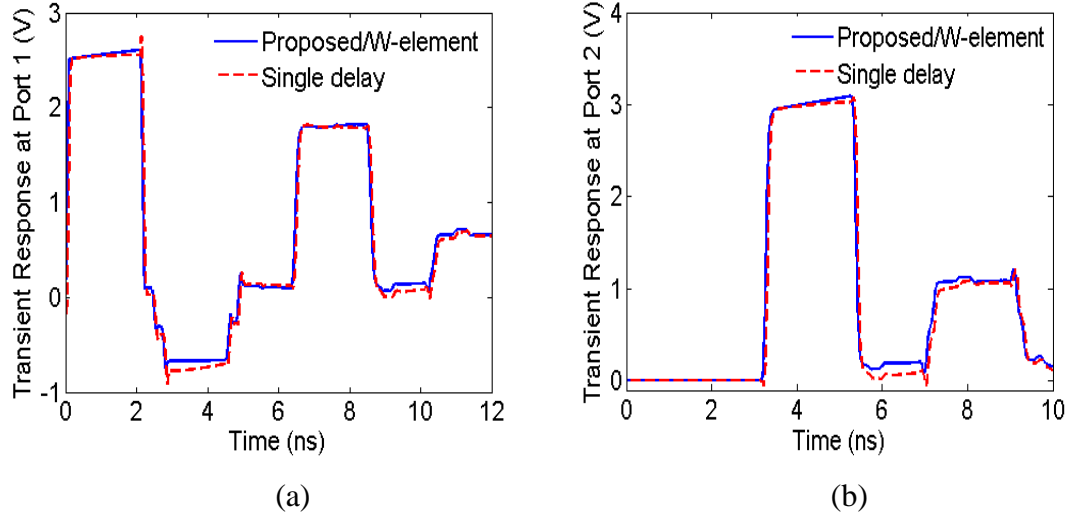


Figure 3-9: Transient response of Example 3 using the proposed algorithm, HSPICE's W-element and single delay extraction based IFFT [19]. (a) Response at Port 1. (b) Response at Port 2.

$$C = \begin{bmatrix} 2 & -0.58 \\ -0.58 & 2 \end{bmatrix} pF/cm$$

$$G = 0 mho/cm$$

The transmission line length of each subnetwork is set to 20 cm and is terminated with a nonlinear inverter. The network is characterized by its terminal responses (Y parameters) as tabulated data over a bandwidth of 0-7 GHz, generated using HSPICE. Next, using the same technique as illustrated in Example 1 and Example 2, the transient response of Example 3 is obtained as well. The extracted delays and the partitioning points of the (ω, τ) plane is reported in table 3.5 and 3.6 respectively. Considering a trapezoidal input pulse of rise time $T_r = 0.05$ ns and pulse width of 2 ns, the transient responses using the proposed algorithm, and the single delay model of [19] are shown in Fig. 3-9. It is observed that the proposed model gives good agreement with HSPICE's W-element, while the single delay extraction model leads to slight errors due to the non negligible phase contribution of the multiple delays.

3.5 Conclusion

In this chapter, a novel approach towards multiple delay extraction within a numerical convolution scheme is proposed for modeling distributed networks characterized by band limited frequency responses. The proposed algorithm uses time-frequency analysis to extract the higher order propagation delays of a distributed network and to evaluate the associated attenuation losses in a piecewise manner, and implements IFFT to efficiently convert the frequency response into a sum of delayed time domain responses. Numerical convolution of the delay-causal response with any input provides accurate transient responses without the need for iterative curve fitting of the band limited data. The algorithm is tested for various multiport transmission line networks and was found to provide more accurate results compared to existing single delay extraction models based on numerical convolution techniques.

Chapter 4

4 Delay Extraction based Macromodeling of Power Distribution Networks

4.1 Introduction

In this chapter, an efficient approach for modeling irregular shaped single layered and multilayered power distribution networks (PDNs) is presented [74]-[75]. The proposed methodology is based on discretization of the structure into a 2D grid of rectangular unit cells. Using a delay extraction based macromodel for each unit cell, a compact circuit model is achieved for the PDN which can explicitly capture the high frequency distributed effects of the network. Moreover, the macromodel is capable of approximating the high frequency skin effect losses and dispersive effect as a passive rational model that is independent of the discretization (i.e. size of the unit cell) and hence needs to be calculated only once for extensive design space explorations. The proposed work has been successfully implemented for a variety of PDN structures and geometries and has been shown to yield significant savings in memory and run time costs compared to the existing quasi-static SPICE lumped models.

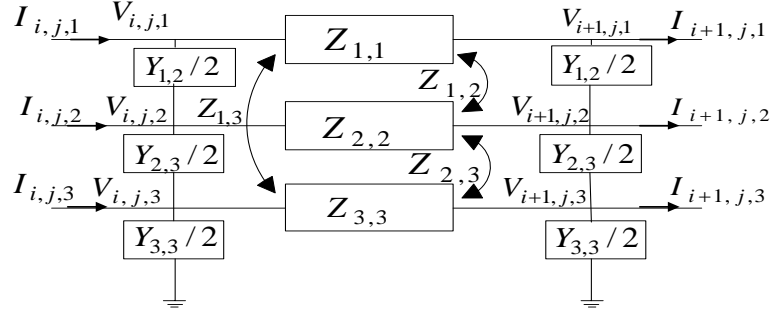


Figure 4-1: Lumped circuit of a single face of unit cell.

4.2 Development of the Proposed Macromodel

The discretization of single and multilayered PDNs into unit cells based on the traditional finite difference method has been covered in Section 2.3. This section begins by demonstrating that the finite difference method for discretization of a general PDN is equivalent to a simple discretization of the Telegraphers partial differential equations for transmission lines. This allows the PDN structures to be realized using a mesh of transmission line segments. Thereafter, the DEFACT macromodel, used to realize the mesh of transmission line segments in SPICE, is described.

4.2.1 Formulation of Transmission Line Model for PDN

In order to explain the proposed transmission line model for PDNs, a general multilayered unit cell obtained from the finite difference discretization of a multilayered PDN, as shown in Fig. 2-4(a), is considered. In order to derive a circuit model representing the electrical performance of the unit cell, it can be represented by an equivalent π -model as illustrated in Fig. 2-4(b). Each of the frequency dependent

elements of Fig. 2-4(b) can be realized in SPICE using a lumped RL/RC network [5], [37].

The π -model representing any single face of the unit cell of Fig. 4-1(b) is considered in Fig. 4-1. The circuit equations governing the voltage/current relationship in the longitudinal direction is given by the following difference equation

$$\begin{aligned}
 V_{i+1,j,k}(s) - V_{i,j,k}(s) = & \sum_{m=1}^{N-1} Z_{k,m} \left(I_{i,j,m}(s) - \left\{ \frac{Y_{m-1,m}(s)}{2} (V_{i,j,m}(s) + V_{i+1,j,m}(s) - V_{i,j,m-1}(s) - V_{i+1,j,m-1}(s)) \right. \right. \\
 & \left. \left. + \frac{Y_{m,m+1}(s)}{2} (V_{i,j,m}(s) + V_{i+1,j,m}(s) - V_{i,j,m+1}(s) - V_{i+1,j,m+1}(s)) \right\} \right) \\
 I_{i+1,j,k}(s) - I_{i,j,k}(s) = & \left\{ \frac{Y_{k-1,k}(s)}{2} (V_{i,j,k}(s) + V_{i+1,j,k}(s) - V_{i,j,k-1}(s) - V_{i+1,j,k-1}(s)) \right. \\
 & \left. + \frac{Y_{k,k+1}(s)}{2} (V_{i,j,k}(s) + V_{i+1,j,k}(s) - V_{i,j,k+1}(s) - V_{i+1,j,k+1}(s)) \right\}
 \end{aligned} \tag{4.1}$$

where the quantities $Z_{k,m}$ and $Y_{k,m}$ for $1 \leq k, m \leq N-1$ is given as

$$Z_{k,m} = 2(R_{i,j} + \hat{R}_{i,j} + sL_{i,j}); \quad Y_{k,m} = \frac{(G_{i,j} + sC_{i,j})}{4} \tag{4.2}$$

and $L_{i,j}$, $C_{i,j}$, $G_{i,j}$, $R_{i,j}$ and $\hat{R}_{i,j}$ represent the coupling term between the i^{th} and j^{th} plane for $0 < i, j < N$ (see (2.7)-(2.9)) and N represents the total number of PDN layers. Defining a new set of variables, $Z_{k,m}^{(pul)} = Z_{k,m}/l$ and $Y_{k,m}^{(pul)} = Y_{k,m}/l$ and replacing them in (4.1), followed by dividing both sides of (4.1) by l and taking the limit to $l \rightarrow 0$, yields after some algebraic manipulations

$$\begin{aligned}
\lim_{l \rightarrow 0} \frac{V_{i+1,j,k}(s) - V_{i,j,k}(s)}{l} &= - \sum_{m=1}^{N-1} Z_{k,m}^{(pul)}(s) I_{i,j,m} \\
\lim_{l \rightarrow 0} \frac{I_{i+1,j,k}(s) - I_{i,j,k}(s)}{l} &= - \sum_{m=1}^{N-1} Y_{k,m}^{(pul)}(s) V_{i,j,m}
\end{aligned} \tag{4.3}$$

The left hand side of (4.3) represents a spatial differential operator and (4.3) can be rewritten as the following differential equation

$$\frac{\partial}{\partial x} \begin{bmatrix} \mathbf{V}_{ij}(s) \\ \mathbf{I}_{ij}(s) \end{bmatrix} = \begin{bmatrix} \mathbf{0} & -\mathbf{Z}^{(pul)}(s) \\ -\mathbf{Y}^{(pul)}(s) & \mathbf{0} \end{bmatrix} \begin{bmatrix} \mathbf{V}_{ij}(s) \\ \mathbf{I}_{ij}(s) \end{bmatrix} \tag{4.4}$$

where $\mathbf{Z}^{(pul)}(s)$ and $\mathbf{Y}^{(pul)}(s)$ are the per-unit-length (p.u.l.) impedance and admittance matrices whose entry in the k^{th} row and m^{th} column is $Z_{k,m}$ and $Y_{k,m}$ respectively and the vectors $\mathbf{V}_{ij}(s)$ and $\mathbf{I}_{ij}(s)$ are defined as

$$\begin{aligned}
\mathbf{V}_{i,j,k}(s) &= [V_{i,j,1}(s), \dots, V_{i,j,N-1}(s)]^t \\
\mathbf{I}_{i,j,k}(s) &= [I_{i,j,1}(s), \dots, I_{i,j,N-1}(s)]^t
\end{aligned} \tag{4.5}$$

The matrices $\mathbf{Z}^{(pul)}(s)$ and $\mathbf{Y}^{(pul)}(s)$ are related to the unit cell parameters of as

$$\begin{aligned}
\mathbf{Z}^{(pul)}(s) &= \mathbf{R}(s) + s\mathbf{L}(s); \\
\mathbf{Y}^{(pul)}(s) &= \mathbf{G}(s) + s\mathbf{C}(s)
\end{aligned} \tag{4.6}$$

where

$$\begin{aligned}
R(s)_{k,m} &= 2[R_{k,m} + \text{Re}(\hat{R}_{k,m}(s))]/l; \\
L(s)_{k,m} &= 2[L_{k,m} + (\text{Im}(\hat{R}_{k,m}(s))/s)]/l;
\end{aligned} \tag{4.7a}$$

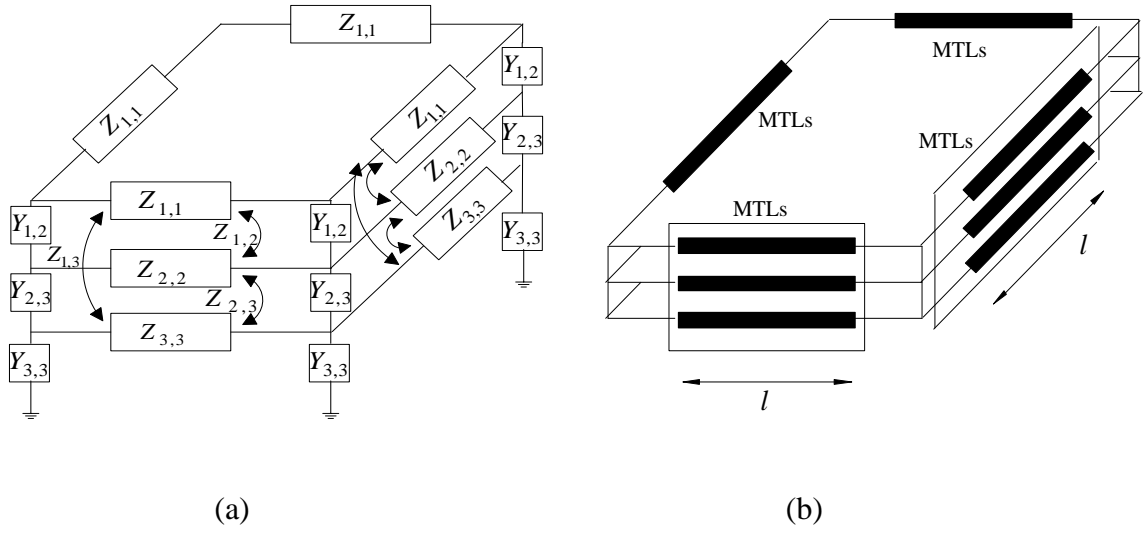


Figure 4-2: (a) Multilayered unit cell. (b) Unit cell model using MTLs.

$$\begin{aligned}
 C(s)_{k,m} &= -[C_{k,m}(s)]/(4l) \quad \forall k \neq m ; \\
 C(s)_{k,m} &= \sum_{m=1, m \neq k}^{N-1} C_{k,m}(s)/(4l) \quad \forall k = m ; \\
 G(s)_{k,m} &= -[G_{k,m}(s)]/(4l) \quad \forall k \neq m ; \\
 G(s)_{k,m} &= \sum_{m=1, m \neq k}^{N-1} G_{k,m}(s)/(4l) \quad \forall k = m ;
 \end{aligned} \tag{4.7b}$$

where $R(s)_{k,m}$, $L(s)_{k,m}$, $C(s)_{k,m}$, $G(s)_{k,m}$ are the entries in the k^{th} row and m^{th} column of $\mathbf{R}(s)$, $\mathbf{L}(s)$, $\mathbf{C}(s)$ and $\mathbf{G}(s)$ matrices respectively and the terms $L_{k,m}$, $C_{k,m}$, $G_{k,m}$, $R_{k,m}$ and $\hat{R}_{k,m}$ can be directly obtained from (2.7)-(2.9). It is observed that (4.4) is the general form of the Telegraphers partial differential equation governing the signal propagation in a MTL structure in the frequency domain [1]. Based on the above discussion, it is appreciated that the finite difference solution of the Helmholtz equation for a unit cell can be represented using distributed MTLs as shown in Fig. 4-2. For the special case of single

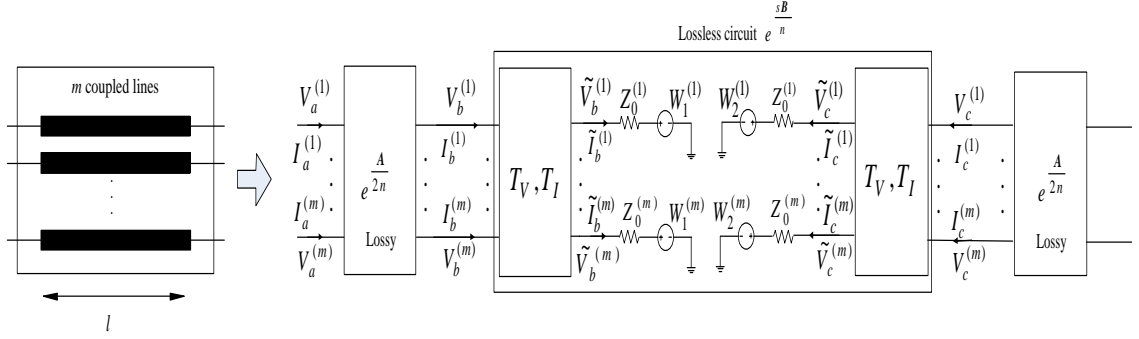


Figure 4-3: DEPACT realization of the single face of the unit cells using MTLs.

layered PDNs, the MTL network of Fig. 4-2 is replaced by a two conductor transmission line segment [74].

In order to obtain an equivalent circuit representation of the MTL compatible with commercial circuit simulators like SPICE, each MTL segment of the Fig. 4-2 is modeled using the delay extraction based passive compact transmission line (DEPACT) segmentation model [31], [32] as explained in the next subsection.

4.2.2 Modeling Unit Cells using DEPACT

Considering the MTL segment making up each face of the unit cell of Fig. 4-2, the solution of (4.4) can be written as an exponential matrix function [31], [32] as

$$\begin{bmatrix} \mathbf{V}_{i+1,j}(s) \\ -\mathbf{I}_{i+1,j}(s) \end{bmatrix} = e^{\boldsymbol{\Phi}} \begin{bmatrix} \mathbf{V}_{i,j}(s) \\ \mathbf{I}_{i,j}(s) \end{bmatrix} \quad (4.8)$$

where $e^{\boldsymbol{\Phi}} = e^{(\mathbf{A}(s)+s\mathbf{B})}$ and \mathbf{A} , \mathbf{B} matrices has already been defined in (2.21b). Typically, the solution of (4.8) does not have an exact time domain counterpart and hence segmentation based modeling techniques as in [1]-[2], [31]-[32] are generally used to derive an equivalent time domain expression of (4.8). Of these segmentation algorithms,

the DEPACT is particularly attractive due to fact that it explicitly extracts the delay of the network leading to better accuracy of the model compared to lumped models of same level of discretization.

The basic idea of DEPACT is to extract the delay terms ($e^{s\mathbf{B}}$) from $e^{(\mathbf{A}(s)+s\mathbf{B})}$ using a Lie decomposition [38], as explained in Section 2.5.4. The Lie decomposition of (2.22) provides a methodology of discretizing the MTL segment of Fig. 4.3 into alternating subsections with the individual stamps of $e^{A(s)/2n}$ and $e^{s\mathbf{B}}$ as shown in Fig. 4-3 for the case $n = 1$. In Fig. 4-3, the modeling of the lossless subsections is performed using a similarity transformation to decouple the lossless MTLs into single conductors followed by the MoC algorithm [1], [26]. In order to model the lossy sections of Fig. 4-3, a Padé approximation is derived as explained in the next subsection.

4.2.3 SPICE Realization of Lossy Section

Based on Fig. 4-3 and (2.22), the lossy subsection with the stamp of $e^{A(s)/2n}$ can be represented as

$$\begin{aligned} \begin{bmatrix} \mathbf{V}_b(s) \\ -\mathbf{I}_b(s) \end{bmatrix} &= e^{A(s)/2} \begin{bmatrix} \mathbf{V}_a(s) \\ \mathbf{I}_a(s) \end{bmatrix} \\ &= e^{\begin{bmatrix} \mathbf{0} & -\mathbf{Z}(s) \\ -\mathbf{Y}(s) & \mathbf{0} \end{bmatrix} l} \begin{bmatrix} \mathbf{V}_a(s) \\ \mathbf{I}_a(s) \end{bmatrix} \end{aligned} \quad (4.9)$$

The variables $\mathbf{V}_a(s)$, $\mathbf{I}_a(s)$ and $\mathbf{V}_b(s)$, $\mathbf{I}_b(s)$ represent the near and far end voltage and current variable vectors as illustrated in Fig. 4-3 respectively, and

$$\mathbf{Z}(s) = \frac{\mathbf{R}(s) + s(\mathbf{L}(s) - \mathbf{L}_\infty)}{2}; \quad \mathbf{Y}(s) = \frac{\mathbf{G}(s) + s(\mathbf{C}(s) - \mathbf{C}_\infty)}{2} \quad (4.10)$$

To capture the frequency dependence of the parameters of (4.9), the functions of (4.10) are approximated as a rational function as

$$\mathbf{Z}(s) \approx \mathbf{r}_0^{(z)} + \sum_{i=1}^{N_z} \frac{\mathbf{r}_i^{(z)}}{s - p_i^{(z)}}, \quad \mathbf{Y}(s) \approx \mathbf{r}_0^{(y)} + \sum_{i=1}^{N_y} \frac{\mathbf{r}_i^{(y)}}{s - p_i^{(y)}} \quad (4.11)$$

where $\mathbf{r}_0^{(z)}$, $\mathbf{r}_0^{(y)}$ are the constant matrices; $\mathbf{r}_i^{(z)}$, $\mathbf{r}_i^{(y)}$ are the matrix containing the i^{th} residue, $p_i^{(z)}$, $p_i^{(y)}$ are the i^{th} poles and N_z , N_y are the order respectively of the rational approximation of (4.11). The poles and residue matrices of (4.11) can be obtained offline for various orders of accuracy while ensuring that the rational approximation is positive real to maintain the passivity of the macromodel [35]. Once the rational functions of (4.11) are available, the DEFACT uses a matrix rational approximation (MRA) derived from a closed form Padé representation of the exponential function of $e^{A(s)/2n}$ [24], [25]. Since the discretization of PDNs result in short MTL segments and the delays of these segments (e^{sB}) have been extracted in (2.22), a Padé order of 1/1 (i.e. $e^x = (1 - x/2)^{-1}(1 + x/2)$) is sufficient to accurately approximate the exponential matrix of (4.9) as

$$e^{A(s)/2} \approx \left[\mathbf{I} - \frac{\mathbf{A}(s)}{4} \right]^{-1} \left[\mathbf{I} + \frac{\mathbf{A}(s)}{4} \right] \quad (4.12)$$

Replacing the rational approximation of (4.11) in (4.12), the exponential matrix of (4.12) can be now be expressed as

$$e^{A(s)/2} = \begin{bmatrix} \mathbf{A}_i(s) & \mathbf{B}_i(s) \\ \mathbf{C}_i(s) & \mathbf{D}_i(s) \end{bmatrix} \quad (4.13)$$

where the $\mathbf{A}_i(s)$, $\mathbf{B}_i(s)$, $\mathbf{C}_i(s)$ and $\mathbf{D}_i(s)$ are expressed in rational form as

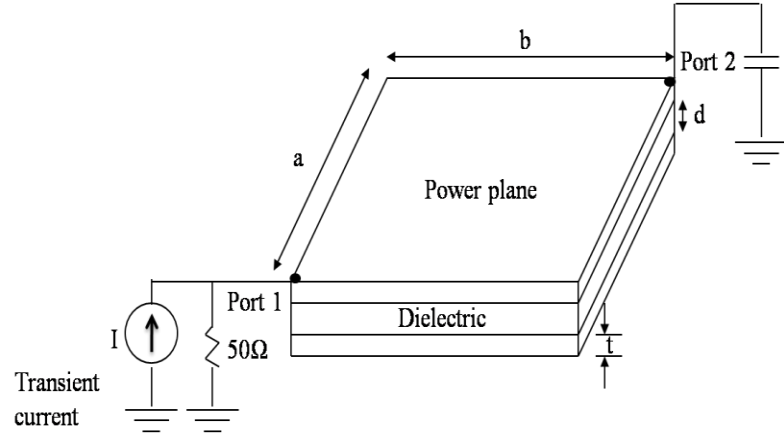


Figure 4-4: Physical structure of PDN for Example 1.

$$\begin{aligned}
 A_i(s) &\approx a_0 + \sum_{j=1} \frac{a_j}{s - \tilde{p}_j}; & B_i(s) &\approx b_0 + \sum_{j=1} \frac{b_j}{s - \tilde{p}_j} \\
 C_i(s) &\approx c_0 + \sum_{j=1} \frac{c_j}{s - \tilde{p}_j}; & D_i(s) &\approx d_0 + \sum_{j=1} \frac{d_j}{s - \tilde{p}_j}
 \end{aligned} \tag{4.14}$$

and the constant matrices \mathbf{a}_j , \mathbf{b}_j , \mathbf{c}_j , \mathbf{d}_j and poles \tilde{p}_j can be obtained from (4.12). It is observed that the rational approximation of (4.11) is independent of the discretization of the structure (i.e. line length l) and hence needs to be done only once for a given bandwidth of interest f_{\max} . With the knowledge of the rational approximation of (4.11), the macromodel of (4.14) can be obtained in a closed form manner for any arbitrary discretization while maintaining the passivity of the model. It is also appreciated that the macromodel of (4.14) can be included in the modified nodal analysis (MNA) matrices of the structure for transient analysis using recursive convolution [34] and this does not augment the MNA matrices in comparison to lumped models which capture the

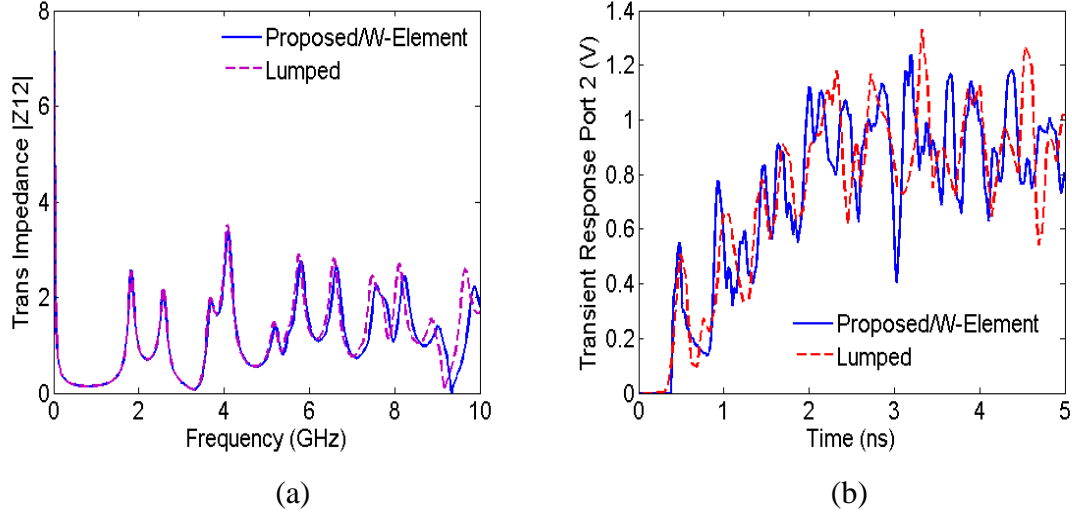


Figure 4-5: Comparison of the proposed DEPACT model with the quasi-static lumped model. (a) Frequency domain response (Z_{12}). (b) Transient response at Port 2.

frequency dependent effects using RL/RC ladders thereby introducing extra nodes/circuit variables in the MNA matrices [5], [37]).

4.3 Numerical Examples

Two examples are presented in this section to demonstrate the validity and efficiency of the proposed delay extraction based macromodeling technique for PDNs. For the proposed work, the rational approximation of (4.11) is obtained using the vector fitting (VF) algorithm [10] on MATLAB 2009b platform and verified to be passive using [35]. For the examples of this section $N_z = N_y = 4$ in (4.11) which corresponds to a 4th order RL/RC ladder to capture the skin effect losses and dispersive effects. The proposed macromodel based on DEPACT is compared with the results of the lumped model based

Table 4-1: Comparison of CPU run time and accuracy of proposed model with lumped model for Example 1

Model	# Unit Cells (length of transmission line segment)	CPU Time (sec)	RMS error w.r.t. IFFT
Proposed	256 ($l = 0.25$ cm)	32.61	0.007
Lumped	256 ($l = 0.25$ cm)	158.10	0.152
	625 ($l = 0.16$ cm)	461.20	0.010
MRA (2 nd order Pade)	256 ($l = 0.25$ cm)	211.75	0.044
	625 ($l = 0.16$ cm)	544.25	0.006

on the FDM [5], [37] (hereafter referred to as the conventional lumped model) where both models are simulated using HSPICE on an UNIX server (66 GB RAM and 160 GB).

Example 1: Single Layered PDN: The objective of the example is to illustrate the accuracy and efficiency achieved using the proposed delay extraction based model compared to existing quasi-static SPICE lumped models for single layered PDNs. A simple rectangular PDN of size 4 cm by 4 cm ($a = 4$ cm, $b = 4$ cm) as shown in Fig. 4-4 is considered. The signal and ground planes are made of copper of thickness $t = 30.5$ μm and separated by a $d = 25.4$ μm thick FR4 dielectric ($\epsilon_r = 4.27$). The input is a current source that mimics the transient current drawn from the PDN during switching of the digital circuits. The PDN is loaded with a linear capacitor of 1pF. Considering a source with rise time 0.1 ns, the size of the unit cell is set to $l = 0.25$ cm. For this given unit cell size, the lumped model of [5] and the proposed delay extraction based model is realized in SPICE. The I/O terminals of the PDN are located at diagonally opposite corners of the PDN as shown in Fig. 4-4. Figure 4-5(a) shows the Z-parameter of the transfer

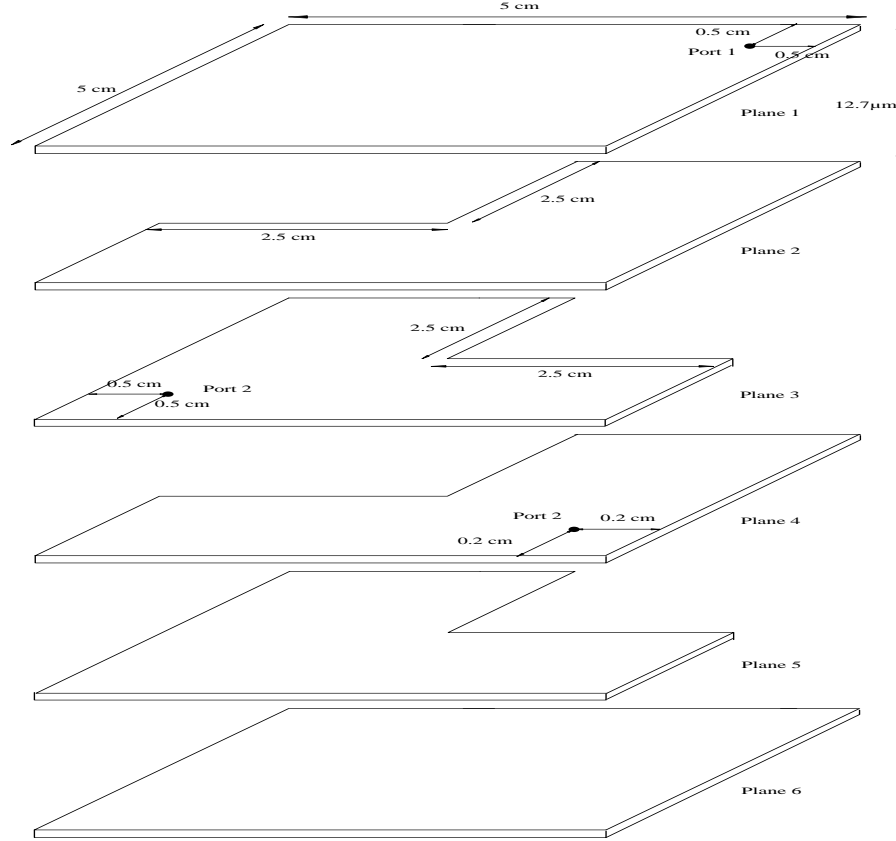


Figure 4-6: 6 coupled multilayered PDN problem of Example 2

impedance (Z_{12}) of the PDN over a bandwidth of 10 MHz - 10 GHz using the proposed model. In addition, the proposed algorithm is compared with the conventional lumped model [5] and the W-element model [33] for the same discretization. It is found that the proposed model can accurately match the W-element model over the entire bandwidth while the lumped model matches the W-element till 5 GHz only.

To estimate the simultaneous switching noise (SSN), a trapezoidal input pulse of rise time $T_r = 0.2$ ns, pulse width of 2 ns and amplitude 20mA is applied at port 1 while the transient response at port 2 is observed. Fig. 4-5(b) shows the transient response at port 2 obtained using the proposed model, the conventional lumped model [5] and the W-element model [33] for the same cell size. The proposed model yields similar responses

as the W-element while the lumped model yields different responses since it cannot capture the high frequency poles of the PDN as seen in Fig. 4-5(a).

Table 4-1 illustrates the computational expense and associated accuracy for the transient analysis using the proposed model, the lumped model and the MRA model [24], [25], all compared against the IFFT result. Note that the proposed model is about 20 times more accurate than the lumped model and 6 times more accurate than the MRA model, all of same discretization. The accuracy of the lumped model can be improved by decreasing the cell size at the cost of increased CPU expense as shown in Table 4-1. For this example, the proposed model provides an approximate speedup of 14 times over the lumped model and 17 times over the MRA model for similar accuracy constraints.

Example 2: Irregular Shaped Multilayered PDN: The objective of this example is to compare the accuracy and efficiency of the proposed delay extraction based model with the lumped model [5], [37] for multilayered PDNs. For this purpose a six layered PDN structure as illustrated in Fig. 4-6 is considered. Each plane of this PDN is 5 cm by 5 cm, made of copper of thickness $t = 0.025$ mm and separated from each other by a FR4 dielectric medium ($\epsilon_r = 4.27$) of thickness $d = 12.7$ μm . The input port is located at Port 1 on plane 1 (4.5, 4.5) and two output ports are located at Port 2 on plane 3 (0.5, 0.5) and Port 3 on plane 4 (4.5, 0.5). Due to the irregular geometry of the planes 2-5, wraparound currents arising in these planes lead to the coupling of entire multilayered structure.

The three port S-parameters of the PDN structure of Fig. 4-6 is extracted using three different methodologies – a reference model based on the exact frequency domain solution of (4.8) for each MTL segment, the proposed macromodel based on DEFACT and the lumped model [5], [37]. In this example, a cell dimensions of $l = 0.5$ cm is

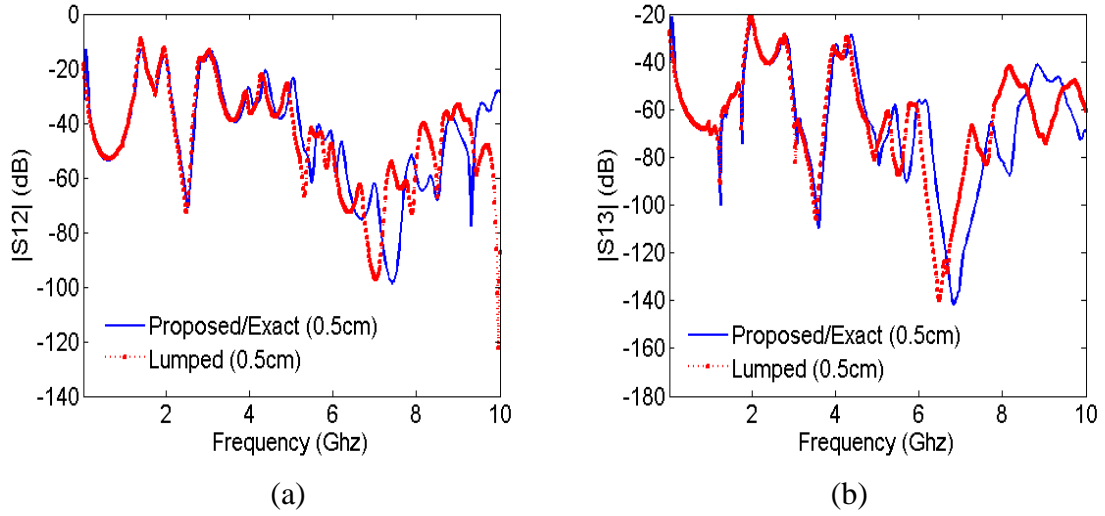


Figure 4-7: Comparison of S parameters of Example 2 using the proposed and lumped models for cell dimensions $l = 0.5$ cm. (a) Magnitude of S_{12} . (b) Magnitude of S_{13} .

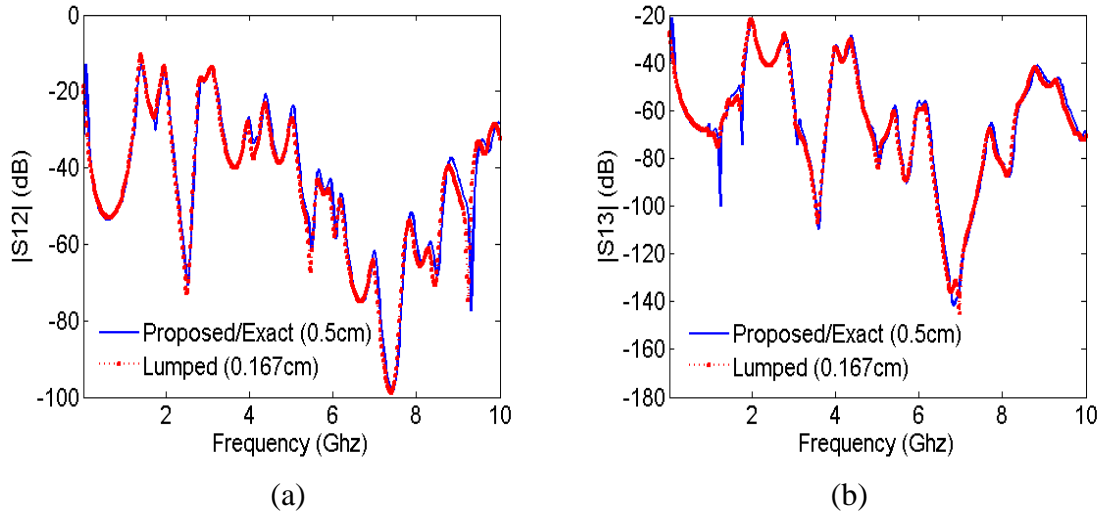


Figure 4-8: Comparison of S parameters of Example 1 the using proposed model ($l = 0.5$ cm) and lumped model ($l = 0.167$ cm). (a) Magnitude of S_{12} . (b) Magnitude of S_{13} .

expected to provide sufficiently accurate results for an input signal of rise time $T_r = 0.2$ ns [33]. As a result, for each of the above model the discretization is set to $l = 0.5$ cm. The results of the above analyses are shown in Fig. 4-7. It is observed that while the proposed macromodel demonstrates good agreement with the exact solution of (4.8) over

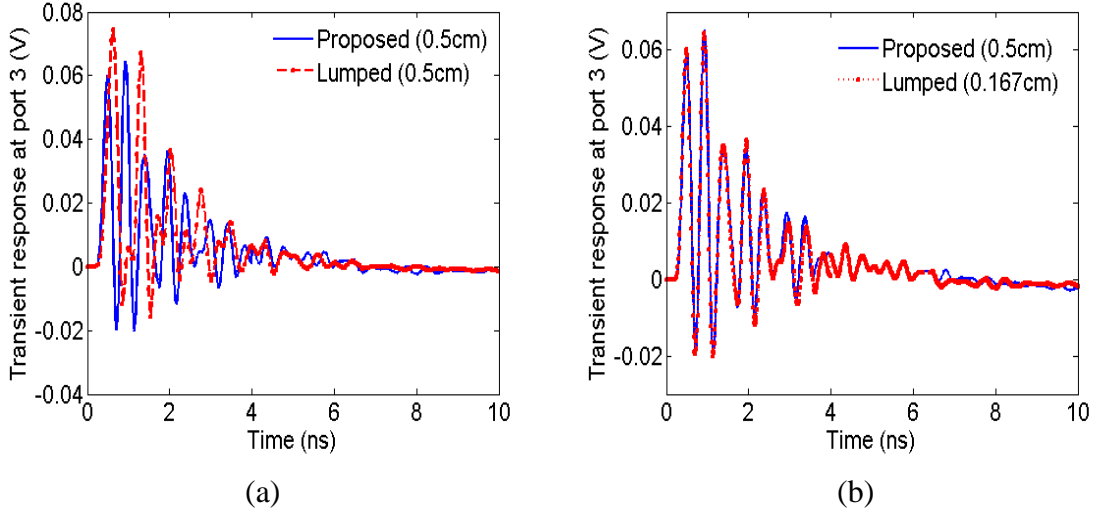


Figure 4-9: Comparison of transient response of Example 2 using the proposed macromodel ($l = 0.5$ cm) and lumped model ($l = 0.167$ cm) (a) Response at Port 2 (b) Response at Port 3.

a bandwidth of 0-10 GHz, the lumped model can only match the exact solution till 4 GHz. The high frequency errors in Fig. 4-7 arise due to the inability of the lumped model to capture the distributed effects of the relatively large unit cell. The results of the lumped model can be improved by considering a smaller discretization of the structure. For this example, the maximum cell dimensions allowable for the lumped model to match the results of the proposed macromodel over the entire bandwidth are $l = 0.167$ cm and the corresponding results are illustrated in Fig. 4-8.

For the transient analysis, an input source modeled as a Norton's equivalent current source with source resistance 20Ω and having a triangular pulse waveform with rise time $T_r = 0.2$ ns and amplitude 50mA is placed at Port 1 while terminating resistances of 500Ω is placed at Port 2 and 3. The input source mimics the injected SSN and the transient response at Port 2 and 3 represents the noise coupling due to the wraparound current. The transient response at Port 2 and 3 using both proposed macromodel and lumped model for

Table 4-2: Comparison of CPU run time and accuracy of proposed model with lumped model for Example 2

Model	No. of Unit Cells (length of MTL segment)	CPU Time (sec)	RMS error w.r.t. IFFT
Proposed	100 ($l = 0.5$ cm)	60.33	4.46e-3
Lumped	100 ($l = 0.5$ cm)	72.35	109.11e-3
	400 ($l = 0.25$ cm)	218.20	50.33e-3
	900 ($l = 0.167$ cm)	483.60	6.56e-3
MRA(2 nd order Pade)	100 ($l = 0.5$ cm)	122.35	67.75e-3
	400 ($l = 0.25$ cm)	288.46	9.50e-3
	900 ($l = 0.167$ cm)	535.67	2.06e-3

the same cell discretization ($l = 0.5$ cm) is shown in Fig. 4-9(a). When the cell discretization for the lumped model is reduced to $l = 0.167$ cm, the transient response for the lumped model shows better agreement with the proposed work as shown in Fig. 4-9(b).

Table 4-2 illustrates the computational expense and associated accuracy for the transient analysis using the proposed macromodel, the lumped model and the MRA transmission line model [24], [25]. For this purpose, all the above two models are compared with respect to the reference model where an IFFT operation is performed on the exact solution of (4.8). It is noted that the proposed macromodel is about 25 times more accurate than the lumped model and 15 times more accurate than the MRA model, all for the same discretization. For this example the proposed macromodel is 8 times as efficient as the lumped model and about 4 times as efficient as the MRA model for a relative error of below $10e-3$.

4.4 Conclusion

In this chapter a delay extraction based approach is presented for achieving accurate macromodels for analysis of single and multilayered power distribution networks in electronic packages and boards. The key contribution of this work is in demonstrating that the finite difference solution of the Helmholtz equation is equivalent to a simple discretization of the Telegraphers partial differential equation. Based on this result a more accurate and efficient delay extraction based macromodel is developed to model the single layered (2D) and multilayered (3D) structure in presence of holes, apertures and irregular geometry. Numerical examples illustrate that the validity and the efficiency of the proposed macromodel over existing quasi-static lumped models.

Chapter 5

5 Longitudinal Partitioning based Waveform Relaxation Algorithm for Efficient Analysis of Distributed Transmission Line Networks

5.1 Introduction

In this chapter a waveform relaxation algorithm is presented for parallelizable transient analysis of large transmission line networks [76], [77]. The proposed methodology represents lossy transmission lines using the DEFACT macromodel of Section 2.5.4. A longitudinal partitioning scheme utilizing the natural disjoint provided by the method of characteristics allows the resulting subcircuits to be weakly coupled by construction [76]. The subcircuits are solved independently using a proposed hybrid iterative technique that combines the advantages of both traditional Gauss-Seidel and Gauss-Jacobi algorithms. The overall algorithm is highly parallelizable and exhibits good scaling with both the size of the network involved and the number of CPUs available. Numerical examples have been presented to illustrate the validity and efficiency of the proposed work.

5.2 Overview of Waveform Relaxation Algorithms

Waveform relaxation (WR), from its introduction in [2], has proven to be an attractive algorithm to address the issue of exorbitant computational costs for solving large networks using traditional circuit solvers like SPICE. The algorithm is based on partitioning large networks into smaller subcircuits and attempting to solve the subcircuits iteratively in parallel.

Presently, two approaches exist for application of waveform relaxation to transmission line networks. One such approach is the transverse partitioning scheme [54], [59]-[63] where multi-conductor transmission lines (MTLs) are partitioned into single lines by assuming weak capacitive and inductive coupling between the lines. The coupling between the lines is represented as time domain relaxation sources introduced into the circuit model of each line.

An alternative waveform relaxation algorithm is based on longitudinal partitioning of the network into repeated subcircuits [58], [64]-[68]. While longitudinal partitioning schemes based on the generalized method of characteristics (MoC) has been reported in [64]-[68], more recent works [58] have focused on partitioning the line based on segmentation models such as the conventional resistive-inductive-conductive-capacitive (RLGC) lumped model [1]. Partitioning techniques based on segmentation models have a common limitation that since each segment directly feeds into the next segment, in other words the adjacent segments are strongly coupled in physical space. This is reflected in the fact that blindly partitioning the conductor between segments requires resolving the stringent

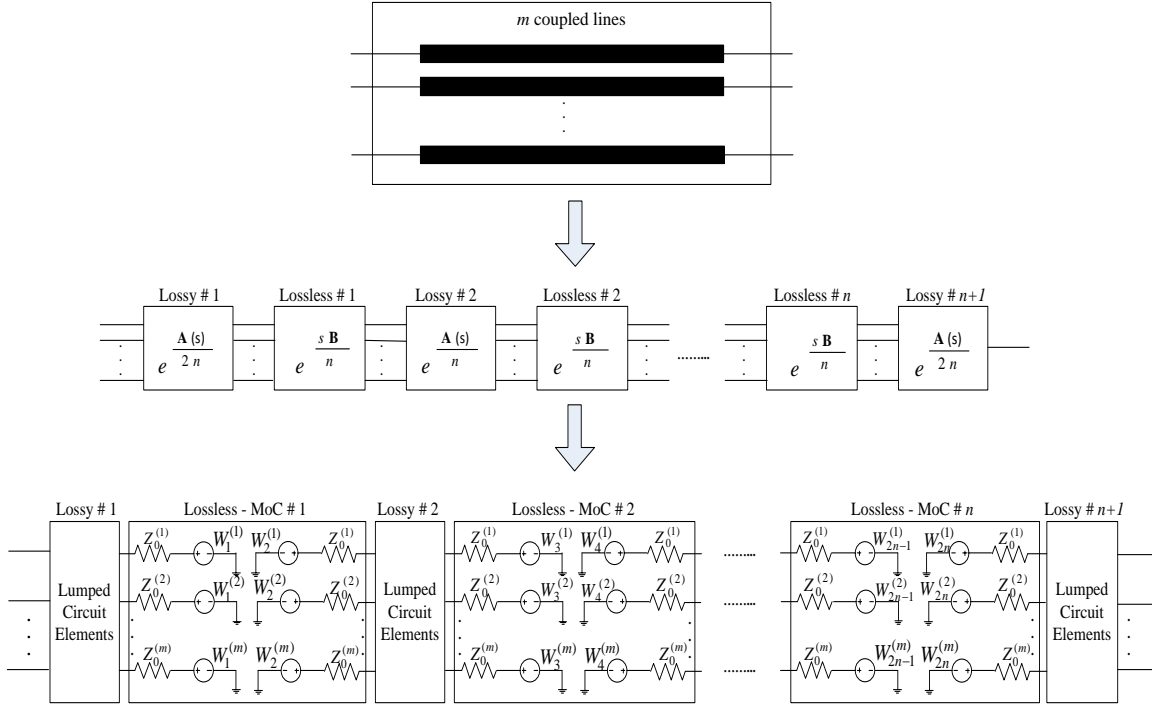


Figure 5-1: SPICE equivalent circuit of a MTL using DEPACT.

Dirichlet's transmission condition across the partition and consequently exhibits poor convergence [58]. The work of [58] accelerated the convergence of the WR algorithm by artificially exchanging additional voltage/current waveforms (i.e. increasing the overlap between subcircuits) followed by optimization routines. The following section addresses this limitation of WR algorithms for typical segmentation based transmission line models.

5.3 Development of Proposed Waveform Relaxation Algorithms

This section begins by describing the proposed longitudinal partitioning scheme for MTLs and thereafter proceeds to discuss both the Gauss-Jacobi (GJ) and the proposed hybrid iterative technique to solve the resultant subcircuits in parallel.

5.3.1 Proposed Partitioning Scheme for MTLs

The DEPACT model of Section 2.5.4 provides a methodology to discretize MTLs into alternating cascade of lossy and lossless line segments as shown Fig. 5-1. To better explain the proposed partitioning methodology, consider the equations for the i^{th} lossless line segment in Fig. 5-1 given below.

$$\begin{bmatrix} \mathbf{V}_{i,out}(s) \\ -\mathbf{I}_{i,out}(s) \end{bmatrix} = e^{\begin{bmatrix} 0 & -\mathbf{L}_\infty \\ -\mathbf{C}_\infty & 0 \end{bmatrix} \frac{l}{n}} \begin{bmatrix} \mathbf{V}_{i,in}(s) \\ \mathbf{I}_{i,in}(s) \end{bmatrix} \quad (5.1)$$

It is observed that (5.1) leads to $2m$ coupled equations. However, the coupled lossless sections can be decoupled into m single lossless lines using a linear transformation of modal voltages/currents as shown below [1]

$$\begin{aligned} \mathbf{V}_{i,in}(s) &= \mathbf{T}_V \tilde{\mathbf{V}}_{i,in}(s); & \mathbf{I}_{i,in}(s) &= \mathbf{T}_I \tilde{\mathbf{I}}_{i,in}(s) \\ \mathbf{V}_{i,out}(s) &= \mathbf{T}_V \tilde{\mathbf{V}}_{i,out}(s); & \mathbf{I}_{i,out}(s) &= \mathbf{T}_I \tilde{\mathbf{I}}_{i,out}(s) \end{aligned} \quad (5.2)$$

where \mathbf{T}_V and \mathbf{T}_I are constant matrices chosen to diagonalize \mathbf{L}_∞ and \mathbf{C}_∞ and have the following properties [1], [32]

$$\tilde{\mathbf{L}} = \mathbf{T}_V^{-1} \mathbf{L}_\infty \mathbf{T}_I; \quad \tilde{\mathbf{C}} = \mathbf{T}_I^{-1} \mathbf{C}_\infty \mathbf{T}_V; \quad \mathbf{T}_V^t = \mathbf{T}_I^{-1} \quad (5.3)$$

and $\tilde{\mathbf{L}} = \text{diag}\{l_1, l_2, \dots, l_m\}$, $\tilde{\mathbf{C}} = \text{diag}\{c_1, c_2, \dots, c_m\}$ are diagonal matrices and the superscript ' t ' denotes the transpose of the matrix. Replacing (5.2)-(5.3) into (5.1) and performing the same algebraic manipulations followed by converting the resultant equations into the time domain, the decoupled lossless sections can be represented using the MoC equations as shown below

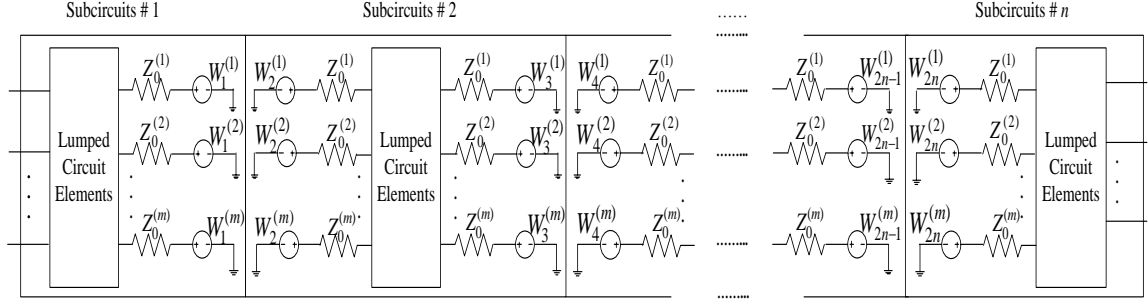


Figure 5-2: Partitioning of MTLs into subcircuits for waveform relaxation.

$$\begin{aligned}
 V_{i,in}^{(j)}(t) &= Z_0^{(j)} I_{i,in}^{(j)}(t) + W_{2i-1}^{(j)}(t) \\
 V_{i,out}^{(j)}(t) &= Z_0^{(j)} I_{i,out}^{(j)}(t) + W_{2i}^{(j)}(t) \\
 W_{2i-1}^{(j)}(t) &= 2V_{i,out}^{(j)}(t - \tau_j) - W_{2i}^{(j)}(t - \tau_j) \\
 W_{2i}^{(j)}(t) &= 2V_{i,in}^{(j)}(t - \tau_j) - W_{2i-1}^{(j)}(t - \tau_j); \quad i = 1, 2, \dots, n; j = 1, 2, \dots, m
 \end{aligned} \tag{5.4}$$

where ‘ j ’ represents the line number, $Z_0^{(j)} = \sqrt{l_j / c_j}$ and $\tau_j = l\sqrt{l_j c_j} / n$ represents the characteristic impedance and delay of each lossless section respectively of the j^{th} line and

$$\begin{aligned}
 \tilde{\mathbf{V}}_{i,in}(t) &= [V_{i,in}^{(1)}(t), \dots, V_{i,in}^{(m)}(t)]^t \\
 \tilde{\mathbf{V}}_{i,out}(t) &= [V_{i,out}^{(1)}(t), \dots, V_{i,out}^{(m)}(t)]^t \\
 \tilde{\mathbf{I}}_{i,in}(t) &= [I_{i,in}^{(1)}(t), \dots, I_{i,in}^{(m)}(t)]^t \\
 \tilde{\mathbf{I}}_{i,out}(t) &= [I_{i,out}^{(1)}(t), \dots, I_{i,out}^{(m)}(t)]^t
 \end{aligned} \tag{5.5}$$

where $\tilde{\mathbf{V}}_{i,in}(t), \tilde{\mathbf{V}}_{i,out}(t), \tilde{\mathbf{I}}_{i,in}(t), \tilde{\mathbf{I}}_{i,out}(t)$ are the time domain counterparts of the vectors $\tilde{\mathbf{V}}_{i,in}(s), \tilde{\mathbf{V}}_{i,out}(s), \tilde{\mathbf{I}}_{i,in}(s), \tilde{\mathbf{I}}_{i,out}(s)$ respectively defined in (5.2). The MoC equations (5.4) for MTLs can be realized using the equivalent circuit of Fig. 5-1 where the matrices \mathbf{T}_V and \mathbf{T}_I arising from the similarity transformation of (5.2) is grouped with the lumped representation of the lossy section. It is observed that the MoC provides natural interfaces for MTLs across which information is exchanged using the time delayed equations of (5.4) rather than the Dirichlet’s transmission conditions of (2.23). Since the Dirichlet’s

transmission condition of (2.23) is responsible for the strong coupling between subcircuits, by avoiding the use of (2.23) and rather longitudinally partitioning transmission lines at natural MoC interfaces, as shown in Fig. 5-2, the WR converges naturally and efficiently [76]. The following section describes the iterative solution of the subcircuits of Fig. 5-2.

5.3.2 Iterative Solution of Subcircuits using Gauss-Jacobi

This discussion begins by considering a general MTL discretized into n subcircuits as illustrated in Fig. 5-2. From Fig. 5-2, it is observed that the sources due to the MoC (i.e. $\{W_{2i-2}^{(j)}(t), W_{2i-1}^{(j)}(t)\}$) act as the relaxation sources that describe that describe the coupling between the adjacent subcircuits. For the k^{th} iteration, it assumed that the waveforms of all the relaxation sources $\{W_{2i-2}^{(k-1,j)}(t), W_{2i-1}^{(k-1,j)}(t)\}; 1 \leq i \leq n$ are known from the previous $k-1^{\text{th}}$ iteration where the additional superscript has been introduced to refer to the iteration count. The known relaxation sources are used as input excitations for the corresponding subcircuits in the k^{th} iteration. This translates to the following terminal conditions required for the i^{th} subcircuits described as

$$\begin{aligned} V_{i-1,out}^{(k,j)}(t) &= Z_0 I_{i-1,out}^{(k,j)}(t) + W_{2i-2}^{(k-1,j)}(t) \\ V_{i,in}^{(k,j)}(t) &= Z_0 I_{i,in}^{(k,j)}(t) + W_{2i-1}^{(k-1,j)}(t); \quad i = 1, 2, \dots, n; \quad j = 1, 2, \dots, m \end{aligned} \quad (5.6)$$

Since the relaxation sources of (5.6) (i.e. $\{W_{2i-2}^{(k-1,j)}(t), W_{2i-1}^{(k-1,j)}(t)\}$) of each i^{th} subcircuit are assumed known beforehand and independent of the present (k^{th}) solution of the remaining $n-1$ subcircuits, the n subcircuits can be solved in parallel using a Gauss-Jacobi (GJ) iteration [55]. The k^{th} iterative solution of all the n subcircuits provides the self consistent

solution of the waveforms $\{V_{i-1,out}^{(k,j)}(t), V_{i,in}^{(k,j)}(t)\}$ which are thereafter used to update the relaxation sources for the future $k+1^{\text{th}}$ iteration using the MoC equations (5.4) as

$$\begin{aligned} W_{2i-2}^{(k,j)}(t) &= 2V_{i-1,in}^{(k,j)}(t-\tau) - W_{2i-3}^{(k-1,j)}(t-\tau) \\ W_{2i-1}^{(k,j)}(t) &= 2V_{i,out}^{(k,j)}(t-\tau) - W_{2i}^{(k-1,j)}(t-\tau); \quad i = 1, 2, \dots, n; \quad j = 1, 2, \dots, m \end{aligned} \quad (5.7)$$

The updating procedure of (5.7) does not require any matrix inversion and since all $2nm$ the equations of (5.7) are mutually decoupled, they can also be solved in parallel. This iterative cycle continues until the absolute error satisfies a predefined tolerance (η)

$$\varepsilon = \frac{1}{2mn} \sum_{j=1}^m \sum_{i=1}^{2n} |W_i^{(k+1,j)} - W_i^{(k,j)}| \leq \eta \quad (5.8)$$

It is noted that the above GJ iterative solution is fully parallelizable and hence faster than sequential GS solution of the subcircuits. However, the GS iterative solution involves greater exchange of waveforms during the updating of the relaxation sources and hence converges faster than GJ solution. Hence, in the next section, a hybrid iterative solution that combines the complimentary features of the GS and GJ solution is described.

5.3.3 Hybrid Iterative Solution of Subcircuits

To explain this contribution, the n subcircuits of Fig. 5-2 is considered to be divided among two groups – group A containing the odd numbered subcircuits and group B, the even numbered subcircuits where the total number of subcircuits within each group is defined as

$$\begin{aligned} n_{odd} &= [n/2] \quad - \quad \text{group A} \\ n_{even} &= n - [n/2] \quad - \quad \text{group B} \end{aligned} \quad (5.9)$$

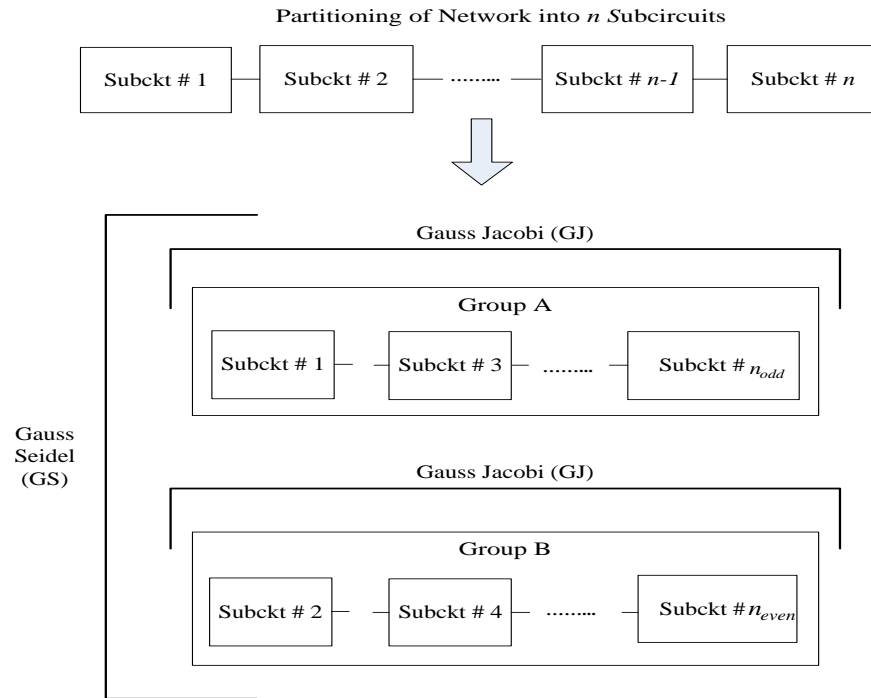


Figure 5-3: Hybrid GS-GJ iterative technique

and $[x]$ represents the greatest integer less than x . Since, for the specific case of longitudinal partitioning, coupling exists between an odd numbered and an even numbered subcircuit only (and not between two odd numbered or two even numbered subcircuits themselves), the k^{th} iterative solution of any subcircuit in any group is independent of the present (k^{th}) solution of any other subcircuit within the same group and rather depends on the present (k^{th}) solution of particular subcircuits within the opposite group. This coupling is addressed using a nested iterative technique. The outer iteration solves the group A and B in sequence (using GS) with updating the relaxation sources after every group solution. This ensures that the coupling between the group A and B converge quickly. The inner iteration solves the subcircuits within each group in

parallel (using GJ) since they are uncoupled. This forms the basis of the proposed hybrid iterative technique and is illustrated in Fig. 5-3.

Assuming that the waveforms of all the relaxation sources responsible for exciting the subcircuits of group A $\{W_{4i-4}^{(k-1,j)}, W_{4i-3}^{(k-1,j)}(t)\}; 1 \leq i \leq n_{odd}$ are known from the previous $k-1^{th}$ iteration, the n_{odd} subcircuits of group A can be solved in parallel via the GJ technique explained in the previous section. Once the GJ is concluded, voltage waveforms $\{V_{2i-2,out}^{(k,j)}(t), V_{2i-1,in}^{(k,j)}(t)\}$ determined from the present (k^{th}) iteration of group A is used to update the relaxation sources responsible for exciting only the subcircuits of group B as

$$\begin{aligned} W_{4i-5}^{(k,j)}(t) &= 2V_{2i-2,out}^{(k,j)}(t-\tau) - W_{4i-4}^{(k-1,j)}(t-\tau) \\ W_{4i-2}^{(k,j)}(t) &= 2V_{2i-1,in}^{(k,j)}(t-\tau) - W_{4i-3}^{(k-1,j)}(t-\tau); \quad i = 1, 2, \dots, n_{even}; \quad j = 1, 2, \dots, m \end{aligned} \quad (5.10)$$

The relaxation sources of (5.10) now serve as the input for the corresponding subcircuits of group B and the n_{even} subcircuits can also be solved in parallel using the GJ technique. The voltage waveforms $\{V_{2i-1,out}^{(k,j)}(t), V_{2i,in}^{(k,j)}(t)\}$ determined from the present (k^{th}) iteration of group B is used to update the relaxation sources responsible for exciting only the subcircuits of group A for the future $k+1^{th}$ iteration as

$$\begin{aligned} W_{4i-4}^{(k,j)}(t) &= 2V_{2i-2,in}^{(k,j)}(t-\tau) - W_{4i-5}^{(k,j)}(t-\tau) \\ W_{4i-3}^{(k,j)}(t) &= 2V_{2i-1,out}^{(k,j)}(t-\tau) - W_{4i-2}^{(k-1,j)}(t-\tau); \quad i = 1, 2, \dots, n_{odd}; \quad j = 1, 2, \dots, m \end{aligned} \quad (5.11)$$

The above iterative cycle of continues till the absolute error of the iterations satisfies the error tolerance as in (5.8). It is noted that (5.10)-(5.11) provide twice the amount of waveform exchange compared to the single waveform exchange of (5.7) per iteration and hence, the hybrid technique exhibits improved convergence compared to the GJ technique.

5.4 Computational Complexity of Proposed Algorithm

This section provides the mathematical reasoning behind the efficiency of the proposed WR algorithm. The analysis begins by considering a general MTL network of Fig. 5-2 discretized into n DEFACT sections. Assuming each DEFACT section to be described using β number of delayed ordinary differential equations, the size of the overall circuit matrix describing the original network is $N = n\beta$. The computational complexity of directly inverting the above matrix to perform time domain analysis is $O(n^3)$ [36], [37]. However, the matrices obtained by traditional circuit simulators are sparse by nature and can be solved more efficiently using sparse matrix routines at a cost of $O(n^\alpha)$ where typically $1.5 \leq \alpha \leq 2$ depending on the sparsity of the matrix [59]. For large distributed networks, the interconnect have to be discretized into many segments to accurately capture the response at the output ports (i.e. large n). For such cases, the super linear scaling of the computational cost for traditional circuit simulators is a major factor limiting its applicability. To address the above issue in the proposed WR algorithm, the n DEFACT sections are separated into n subcircuits each described using β delayed differential equations which can now be solved independently. The total computational cost of the proposed WR algorithm is mathematically quantified using the following lemmas.

Lemma 1: For n subcircuits, the computational cost of the proposed WR algorithm using traditional GJ iterations is $O([n/p]n_i)$ where n_i is the number of iterations and p is the number of CPUs available for parallel processing.

Proof: For typical WR algorithms, the total computational cost can be divided into two parts - the first part is to solve the n subcircuits independently and the next is to update the relaxation sources.

It is assumed that the cost of solving one subcircuit scales as $k_1\beta^\alpha$ where k_1 is the scaling coefficient. Using a GJ iterative technique where the task of independently solving n subcircuits can be distributed over p CPUs, the total cost of solving the n subcircuits per iteration is given by $k_1\beta^\alpha \cdot [n/p]$. The second stage of the algorithm involves updating the $2nm$ relaxation sources using (5.7). This translates to the solution of $2nm$ linear algebraic equations in the time domain per iteration. Since the equations are all decoupled, they can be solved independently in parallel using p CPUs for a cost of $k_2[2nm/p]$ where k_2 is the scaling coefficient for the second part of the proposed WR algorithm. Since, within the context of this analysis, $2m$ is a constant, the above cost can be rewritten as $k_2[2nm/p] = k_3[n/p]$. Thus the total cost per iteration is the sum of the above costs given as

$$\hat{\phi}_{GJ} = k_1\beta^\alpha [n/p] + k_3[n/p] \quad (5.12)$$

where $\hat{\phi}_{GJ}$ is the cost of each GJ iteration. Since the above process needs to be redone for n_i iterations, the total cost of the proposed algorithm using traditional GJ is

$$\phi_{GJ} = \hat{\phi}_{GJ} \cdot n_i = k_1\beta^\alpha [n/p]n_i + k_3[n/p]n_i \quad (5.13)$$

where ϕ_{GJ} is the total cost of the proposed algorithm using GJ.

It is observed that the solution of the $2nm$ linear algebraic equations to update the relaxation sources of (5.7) does not involve any matrix inversion. On the other hand, the solution of each subcircuits involves the inversion of a matrix of size β . As a result, the cost of solving the subcircuits (first part) is found to dominate over the cost of updating the relaxation sources (second part) [54] (i.e. $k_1\beta^\alpha \gg k_3$). Hence, the result of (5.13) can be simplified to

$$\phi_{GJ} \approx k_1\beta^\alpha [n/p]n_i \quad (5.14)$$

where within the context of this work β is a function of the number of MTLs (m) and is treated as a constant. Equation (5.14) demonstrates that the proposed WR algorithm scales as $O([n/p]n_i)$ when using the traditional GJ. The following lemma extends the above analysis to the hybrid iterative technique.

Lemma 2: For n subcircuits, the computational cost of the proposed WR algorithm using the hybrid iterative technique is $O([n/p]\hat{n}_i)$ where \hat{n}_i is the number of iterations involved.

Proof: The cost of the proposed WR algorithm using the hybrid iterative technique can be divided into two parts – the first part is to solve the n_{odd} subcircuits and update the $2n_{even}m$ relaxation sources using (5.10). The second part is to solve the n_{even} subcircuits and update the $2n_{odd}m$ relaxation sources using (5.11). Since updating the relaxation sources using (5.10)-(5.11) does not require any matrix inversion, the contribution of solving (5.10)-(5.11) is minimal compared to the cost of the solution of each subcircuit (see *Lemma 1* and [54]). As a result, the total cost of the hybrid iterative technique can be

approximated as simply the cost of the independent solution of the n_{odd} and n_{even} subcircuits.

The computational cost of solving the n_{odd} subcircuits per iteration using the GJ technique with p parallel CPUs is given by $k_1\beta^\alpha.[n_{odd}/p]$ (from *Lemma 1*). Similarly, the cost of the n_{even} subcircuits per iteration is approximated as $k_1\beta^\alpha.[n_{even}/p]$. Since, the solution of n_{odd} and n_{even} subcircuits proceeds in sequence, the total cost of the hybrid technique per iteration is the sum of the above two costs

$$\hat{\phi}_{GS-GJ} \approx k_1\beta^\alpha([n_{odd}/p] + [n_{even}/p]) \quad (5.15)$$

Multiplying the above cost with the number of iterations (in this case \hat{n}_i) provides an estimate of the full computational cost of the proposed WR algorithm using the proposed GS-GJ hybrid iterative technique as below.

$$\phi_{GS-GJ} \approx \hat{\phi}_{GS-GJ}.\hat{n}_i \approx k_1\beta^\alpha([n_{odd}/p] + [n_{even}/p])\hat{n}_i \quad (5.16)$$

From the definition of n_{odd} and n_{even} in (5.9), (5.16) can be approximated to

$$\phi_{GS-GJ} \approx k_1\beta^\alpha[n/p]\hat{n}_i \quad (5.17)$$

Equation (5.17) demonstrates that the proposed WR algorithm scales as $O([n/p]\hat{n}_i)$ when using the hybrid iterative technique. Comparing the scaling of (5.14) and (5.17) with number of available CPUs (p), it is appreciated that the hybrid iterative technique retains the high degree of parallelizability as the GJ technique. However, the hybrid technique has the added advantage of faster convergence over the GJ counterpart due to

the greater exchange of waveforms using (5.10)-(5.11) compared to the single exchange of (5.7) (i.e. $\hat{n}_i < n$).

It is observed that the main reason behind the attractiveness of the proposed algorithm (whether using GJ or the hybrid technique) is the ability to solve the subcircuits independently. This translates to an almost linear scaling of the computational costs of the proposed algorithm with number of DEPACT sections unlike SPICE which suffers from a super linear scaling. In addition, using GJ and the hybrid technique provides an additional advantage over SPICE of dividing the computational cost of the proposed algorithm over multiple CPUs ($p > 1$). These results will be validated using the numerical examples in the following section.

5.5 Numerical Results

Two examples are presented in this section to demonstrate the validity and efficiency of the proposed algorithm. For a fair comparison of the proposed LP-WR algorithm with full blown SPICE simulation using segmentation techniques, this work is compared with the DEPACT model of [32] (hereafter referred to as ‘full SPICE simulation’) which is based on a delay extraction principle and hence is highly efficient for modeling long MTL networks. The parallel solution of the subcircuits are automated in MATLAB 2011b while the actual solution of the subcircuits are performed using HSPICE on a UNIX server (66 GB RAM and 160 GB memory). A customized C++ code has been developed to extract and update the waveforms of the relaxation sources.

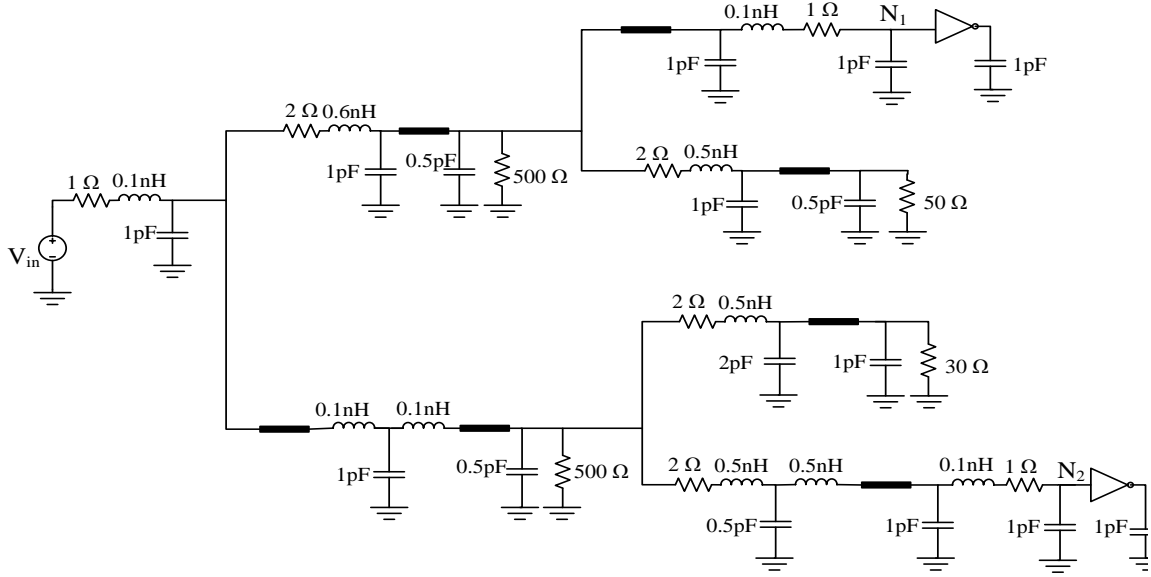


Figure 5-4: Circuit of Example 1.

Example 1: Single Line Network: The objective of this example is to demonstrate the accuracy of the proposed WR algorithm and the superior convergence of the hybrid iterative technique over the traditional GJ technique. For this example a transmission line network consisting of seven transmission line segments as shown in Fig. 5-4 is considered. The per-unit-length (p. u. l.) parameters of the network are $R = 0.25\ \Omega/\text{cm}$, $L = 4\ \text{nH}/\text{cm}$, $C = 1.21\ \text{pF}/\text{cm}$, $G = 0.2\ \text{mmho}/\text{cm}$ and $R_s = 1.9\text{e-}5\ \Omega/\sqrt{\text{Hz}}/\text{cm}$ where $R_t(s) = R_s\sqrt{f}(1+j)$ represents the skin effect losses as a function of frequency f [6]. The network is excited by a trapezoidal voltage source of rise time $T_r = 0.1\ \text{ns}$, pulse width $5\ \text{ns}$, amplitude of 2V and loaded with two SPICE level 49, CMOS inverters using $180\ \text{nm}$ technology.

To illustrate the accuracy of the proposed algorithm, the line length of each segment is set to $l = 30\ \text{cm}$. In this case, the total number of subcircuits required is 420. The network is then solved using both proposed work and the full SPICE simulation. The proposed work

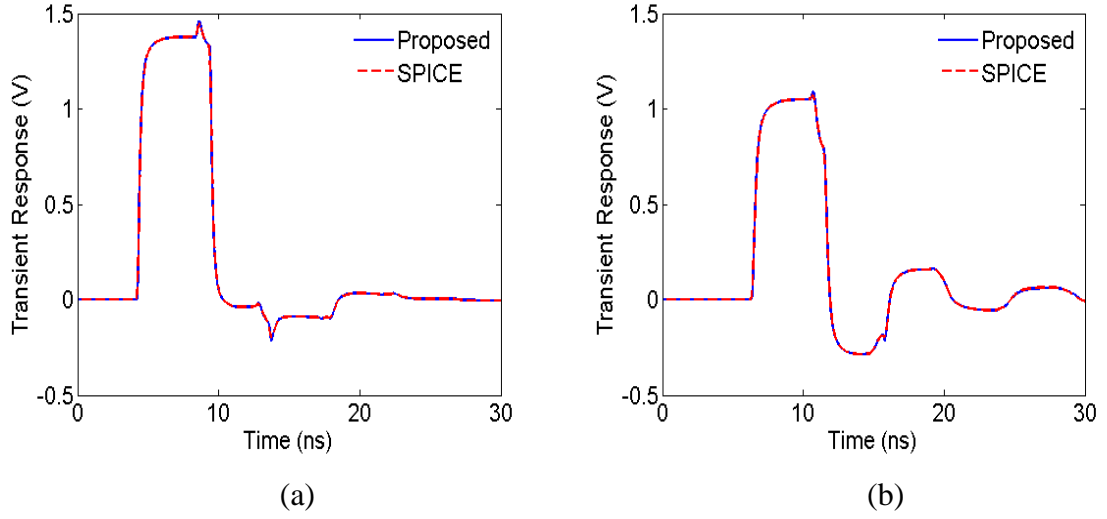


Figure 5-5: Transient response for Example 1. All line lengths are $l = 30$ cm. (a) Transient response at output port N_1 . (b) Transient response at output port N_2 .

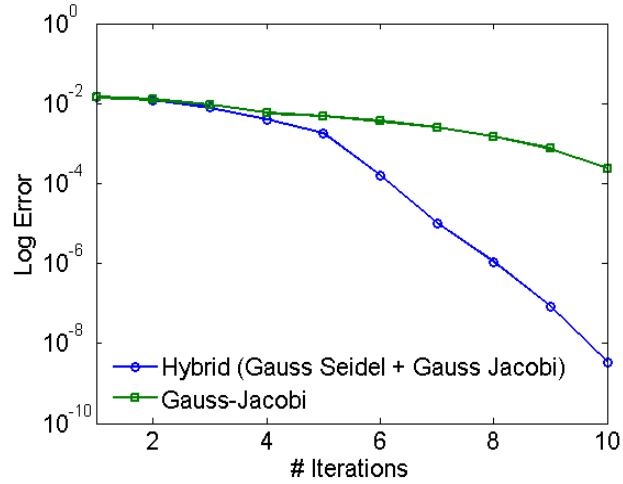


Figure 5-6: Convergence properties of the proposed hybrid iterative technique compared to GJ. All line lengths are $l = 30$ cm

uses the hybrid iterative technique to solve the subcircuits on a sequential platform ($p = 1$) using GJ and the predefined error tolerance set to $\eta = 1e-5$ and an initial guess of the relaxation sources set to the DC solution of zero. The transient responses at the far end of

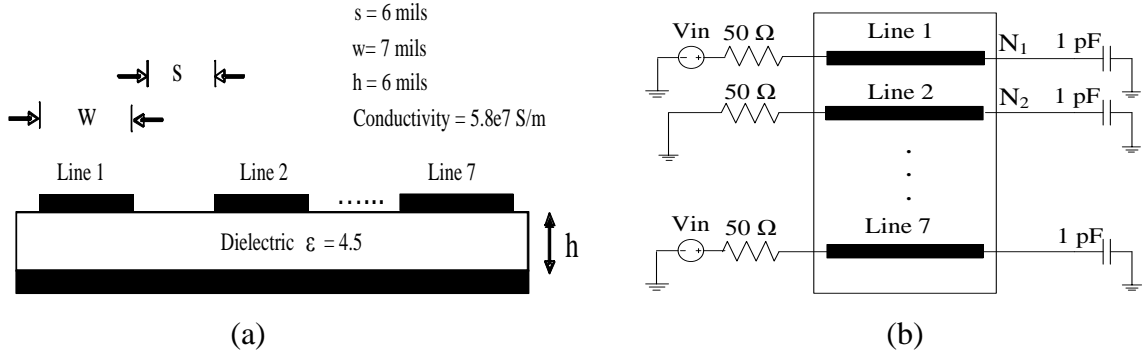


Figure 5-7: Transmission line structure of Example 2.

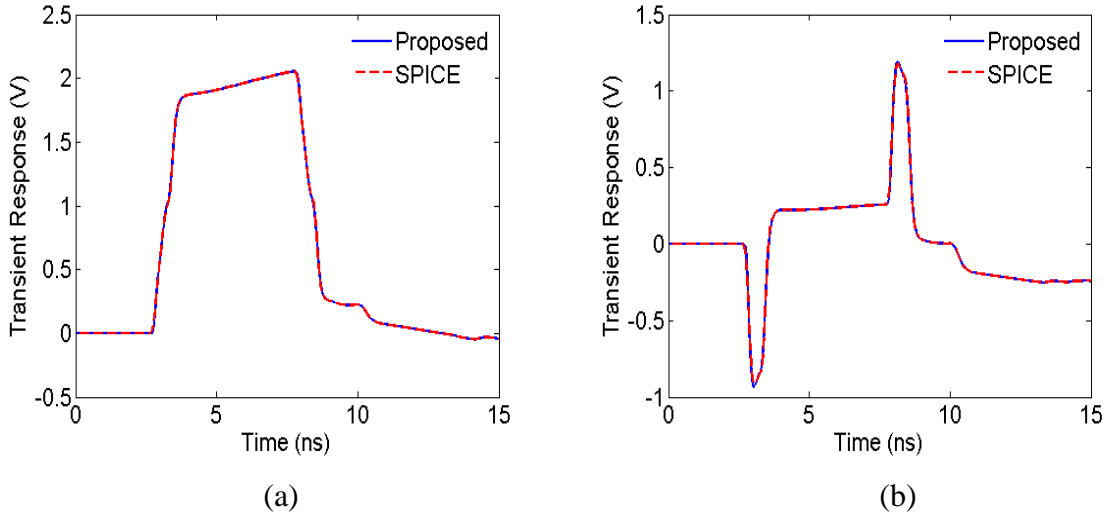


Figure 5-8: Transient response for Example 2. Line length of the network is $l = 50$ cm.

(a) Transient response at output port N_1 . (b) Transient response at output port N_2 .

the network (N_1 , N_2) using the proposed WR algorithm and full SPICE simulations are shown in Fig. 5-5.

Next, the convergence properties of the proposed hybrid technique are compared with the traditional GJ technique. For each algorithm, the number of iterations is varied from 1 to 10 and the scaling of the associated error is displayed in Fig. 5-6. It is observed that the proposed hybrid technique shows significantly faster convergence than the traditional GJ

algorithms. This is due to the fact that the proposed hybrid technique involves twice the amount of information exchange as the GJ technique for same number of iterations.

Example 2: MTL Network: The objective of this example is to illustrate the computational efficiency of the proposed work over full SPICE simulations for MTL structures. For this example a 7-coupled line network with the physical dimensions as shown in Fig. 5-7(a) is considered. The per-unit-length parameters for this example are extracted from the HSPICE field solver [6] and include frequency dependent parameters. For the following analyses, the MTL network topology is shown in Fig. 5-7(b) where line 1, 3, 5 and 7 is excited with trapezoidal voltage sources of rise time $T_r = 0.1$ ns, pulse width 5 ns and amplitude of 2V.

This example begins with a demonstration of the performance of the proposed work compared to full SPICE simulations as the size of the network increases. The line length of the network (l) in Fig. 5-7 is increased from 0 cm to 200 cm in steps of 10 cm. To accurately model the network, the numbers of subcircuits, n are increased in steps of 16 for each 10 cm step and ranges from 0 to 320. For each case, the network is solved using both proposed work and the full SPICE simulation. The proposed work uses both the hybrid technique and traditional GJ technique on a sequential platform ($p = 1$) with the predefined error tolerance set to $\eta = 1e-5$ and an initial guess of the relaxation sources set to the DC solution of zero. For this particular error tolerance, the number of iterations required for convergence is found to be consistently between 5 and 6. The accuracy of the proposed work (with the hybrid technique) compared to full SPICE simulation is illustrated in Fig. 5-8 for $l = 50$ cm (i.e. for 80 subcircuits). The scaling of the computational cost of both proposed work and full SPICE simulation with the line length

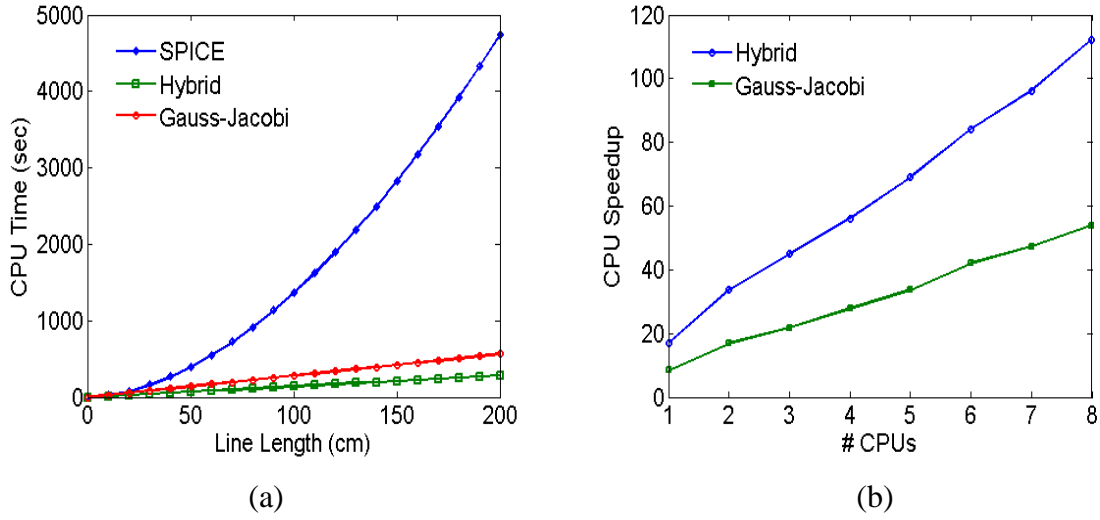


Figure 5-9: Scaling of computational cost for Example 2. (a) Scaling of computational cost with line length (l) (b) Scaling of CPU speed up with number of CPUs ($l = 200$ cm)

Table 5-1: Comparison of CPU run time for Example 2

# CPU	CPU Time (sec)				Speedup w. r. t. Gauss-Jacobi	Speedup w. r. t. Gauss-Seidel	Speedup w. r. t. Hybrid
	Gauss Jacobi	Gauss Seidel	Hybrid	SPICE			
1	562.99	197.35	281.50	4736.30	8.41	24.00	16.83
4	170.67		84.45		27.75		56.09
6	112.60		56.30		42.06		84.13
8	87.97		42.22		53.84		112.17

(l) is shown in Fig. 5-9(a). It is observed from Fig. 5-9(a) that the proposed work scales almost linearly ($O(n)$) for both GJ and the hybrid algorithm as predicted in (5.14), (5.17) respectively while the full SPICE solution of the original network scale super linearly as $O(n^\alpha)$ where $\alpha = 1.8$ for this example. In addition the hybrid iterative technique converges twice as fast as traditional GJ technique.

Next, the performance of the proposed work is demonstrated on a parallel platform. The length of the network is fixed at the corner of our design space where $l = 200$ cm and the network solved using both proposed work and full SPICE simulation. The proposed WR iterations are performed using the hybrid technique, the traditional GS and the traditional GJ techniques where number of processors are varied from $p = 1$ to $p = 8$ for the same error tolerance as before. The CPU speed up offered by the hybrid and GJ techniques over full SPICE simulations is shown in Fig. 5-9(b). The actual CPU run times for the hybrid, GS, GJ and the sequential SPICE simulation is summarized in Table 5-1. The speed up for either iterative technique scale almost linearly with number of processors, thereby demonstrating the high parallelizability of both as theoretically expected from (5.14) and (5.17). The minor deviation of Fig. 5.9(b) from the exactly linear scaling with respect to number of CPUs (p) is due to the incurred communication overheads between processors.

5.6 Conclusion

In this chapter a longitudinal partitioning based waveform relaxation algorithm for parallel transient analysis of distributed transmission line networks is presented. The proposed methodology utilizes the regular MoC interfaces provided by the DEFACT as possible partitioning interfaces thereby longitudinally partitioning the network into weakly coupled subcircuits. The subcircuits are solved independently using a hybrid iterative technique that combines the fast convergence of the proposed GS technique with the parallelizability of the GJ technique. Numerical examples illustrate that the proposed

algorithm exhibits good scaling with both the size of the network and the number of CPUs available for parallel processing, thereby providing significant savings in run time costs compared to full SPICE simulations.

Chapter 6

6 Electromagnetic Interference Analysis of Multiconductor Transmission Line Networks using Longitudinal Partitioning based Waveform Relaxation Algorithm

6.1 Introduction

This work extends the concepts of [76], [77] to perform parallel EMI analysis of MTL networks [78], [79]. The distributed nature of the incident field coupling with the network is represented as lumped sources introduced into each DEFACT section. Combining the lumped sources (due to EM fields) with the delayed sources due to the MoC representation of the lossless section leads to a more compact realization of the subcircuits as well as reduces the communication overhead between processors leading to a more scalable LP-WR algorithm. The resultant subcircuits are solved independently using the hybrid iterative technique that was presented in Section 5.3.3. The overall

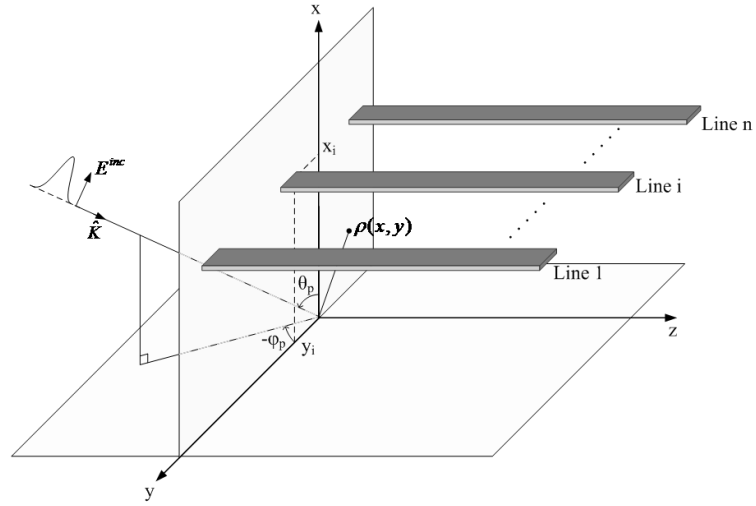


Figure 6-1: Geometry of a multiconductor transmission line exposed to an incident field.

algorithm is highly parallelizable and exhibits good scaling with both the size of the circuit involved and the number of CPUs available as illustrated in the numerical examples section.

6.2 Background of EMI Analysis of MTL Networks

In order to explain the contributions of the proposed work, this section discusses the general formulation of MTL structures exposed to incident fields followed by a description of the DEPACT macromodel reported in [32] to perform the EMI analysis.

6.2.1 General Formulation of MTLs Exposed to Incident EM Fields

Consider a MTL network supporting quasi-transverse electromagnetic mode of propagation, backed by a reference plane and exposed to incident fields as shown in Fig.

6-1. In such cases, the MTL structure is described by the inhomogeneous Telegraphers partial differential equations as follows [1]

$$\frac{\partial}{\partial x} \begin{bmatrix} \mathbf{V}(z, s) \\ -\mathbf{I}(z, s) \end{bmatrix} = \begin{bmatrix} \mathbf{0} & -(\mathbf{R}(s) + s\mathbf{L}(s)) \\ -(\mathbf{G}(s) + s\mathbf{C}(s)) & \mathbf{0} \end{bmatrix} \begin{bmatrix} \mathbf{V}(z, s) \\ \mathbf{I}(z, s) \end{bmatrix} + \begin{bmatrix} \mathbf{V}_F(z, s) \\ \mathbf{I}_F(z, s) \end{bmatrix} \quad (6.1)$$

where $\mathbf{V}(z, s)$ and $\mathbf{I}(z, s)$ represent the spatial distribution of the voltage and current along the longitudinal direction, $\mathbf{R}(s)$, $\mathbf{L}(s)$, $\mathbf{G}(s)$ and $\mathbf{C}(s)$ are the frequency-dependent resistive, inductive, conductive and capacitive per-unit-length (p. u. l.) parameters of the line respectively, $s = j2\pi f$ is the Laplace variable and f is the instantaneous frequency. The functions $\mathbf{V}_F(z, s)$ and $\mathbf{I}_F(z, s)$ represent the effect of the incident field coupled to the MTL and can be mathematically expressed as [48]-[51]

$$\begin{aligned} \mathbf{V}_F(z, s) &= -\frac{\partial}{\partial z} \mathbf{E}_T(z, s) + \mathbf{E}_L(z, s) \\ \mathbf{I}_F(z, s) &= -(\mathbf{G}(s) + s\mathbf{C}(s))\mathbf{E}_T(z, s) \end{aligned} \quad (6.2)$$

and

$$\mathbf{E}_L(z, s) = (\vec{\mathbf{e}}_z(x_i, y_i, z) - \vec{\mathbf{e}}_z(x_0, y_0, z)) \cdot \mathbf{E}_T(z, s) = \int_{\rho(x, y)} \vec{\mathbf{e}}_t(\rho, z) \cdot d\rho \quad (6.3)$$

The variables $\vec{\mathbf{e}}_z$ and $\vec{\mathbf{e}}_t$ are the longitudinal and transverse components of the incident electric field respectively; (x_i, y_i) and (x_0, y_0) refer to spatial coordinates of the i^{th} conductor and the reference conductor respectively and ρ is a parameter of x - and y - in the transverse plane (see Fig. 6-1).

Different types of far radiating sources are often approximated in a localized region of space as uniform plane waves [1], [48]-[52]. For such examples the electric field of the incident field can be expressed as

$$\vec{\mathbf{E}}^i(x, y, z) = E(s)(A_x \vec{\mathbf{a}}_x + A_y \vec{\mathbf{a}}_y + A_z \vec{\mathbf{a}}_z) e^{-s\beta_x x} e^{-s\beta_y y} e^{-s\beta_z z} \quad (6.4)$$

where $E(s)$ is the electric field amplitude, A_x , A_y , and A_z are the direction cosines of the incoming wave and $\beta = [\beta_x, \beta_y, \beta_z]^t$ is the propagation vector. Replacing (6.4) in (6.3) and solving (6.1), the frequency domain expression of the current/voltage at the line extremities is written [79]

$$\begin{pmatrix} \mathbf{V}(l, s) \\ -\mathbf{I}(l, s) \end{pmatrix} - \begin{pmatrix} \mathbf{V}_t(l, s) \\ \mathbf{0} \end{pmatrix} = e^{\boldsymbol{\Phi}l} \begin{pmatrix} \mathbf{V}(0, s) \\ \mathbf{I}(0, s) \end{pmatrix} - \begin{pmatrix} \mathbf{V}_t(0, s) \\ \mathbf{0} \end{pmatrix} + \mathbf{J}(l, s) \quad (6.5)$$

where $e^{\boldsymbol{\Phi}} = e^{(\mathbf{A}(s) + s\mathbf{B})}$ and \mathbf{A} , \mathbf{B} matrices are as defined in (2.21) for unit length and

$$\mathbf{J}(l, s) = \int_0^l e^{\boldsymbol{\Phi}(l-z)} \begin{pmatrix} \mathbf{V}_z(z, s) \\ \mathbf{0} \end{pmatrix} dz \quad (6.6)$$

In (6.5)-(6.6), the terms \mathbf{V}_t and \mathbf{V}_z can be expressed in closed-form as

$$\mathbf{V}_z(z, s) = se^{-s\beta_z z} E_0(s) \mathbf{V}_{F1}; \quad \mathbf{V}_t(z, s) = e^{-s\beta_z z} E_0(s) \mathbf{V}_{F2} \quad (6.7)$$

where

$$\mathbf{V}_{F1} = \begin{bmatrix} \vdots \\ -2A_z\beta_y y_i \\ \vdots \end{bmatrix}; \quad \mathbf{V}_{F2} = \begin{bmatrix} \vdots \\ -2A_x x_i \\ \vdots \end{bmatrix} \quad (6.8)$$

In order to represent the EMI effects of (6.5) using an equivalent circuit model, the DEPACT macromodel of [32] is utilized as explained in the next subsection.

6.2.2 DEPACT Model for EMI Analysis

The DEPACT macromodel uses a modified Lie product [38] to approximate the exponential function in (6.5) as a product of exponentials as already discussed in (2.22) of Section 2.5.4.

The effect of the incident field coupling to the MTL structure can be reduced to the following two steps - the effect of the incident field on the lossless sections ($e^{sBl/n}$) is evaluated first and thereafter, the lossy sections ($e^{Al/2n}$) are incorporated into the macromodel [51]. For this purpose, the solution of (6.1) for any i^{th} lossless section can be formulated similar to (6.5)-(6.8) as [79]

$$\begin{pmatrix} \mathbf{V}_{i,out}(s) \\ -\mathbf{I}_{i,out}(s) \end{pmatrix} - \begin{pmatrix} \mathbf{V}_t(z_i, s) \\ \mathbf{0} \end{pmatrix} = e^{\frac{sBl}{n}} \begin{pmatrix} \mathbf{V}_{i,in}(s) \\ \mathbf{I}_{i,in}(s) \end{pmatrix} - \begin{pmatrix} \mathbf{V}_t(z_{i-1}, s) \\ \mathbf{0} \end{pmatrix} + \mathbf{J}_i(s) \quad (6.9)$$

where

$$\begin{aligned} \mathbf{J}_i(s) &= \int_{z_{i-1}}^{z_i} e^{s\mathbf{B}(z_i-z)} \begin{pmatrix} \mathbf{V}_z(z, s) \\ \mathbf{0} \end{pmatrix} dz \\ \mathbf{V}_{i,in}(s) &= [V_{i,in}^{(1)}(s), \dots, V_{i,in}^{(m)}(s)]^t; \quad \mathbf{V}_{i,out}(s) = [V_{i,out}^{(1)}(s), \dots, V_{i,out}^{(m)}(s)]^t \\ \mathbf{I}_{i,in}(s) &= [I_{i,in}^{(1)}(s), \dots, I_{i,in}^{(m)}(s)]^t; \quad \mathbf{I}_{i,out}(s) = [I_{i,out}^{(1)}(s), \dots, I_{i,out}^{(m)}(s)]^t \end{aligned} \quad (6.10)$$

The variables $\mathbf{V}_{i,in}(s)$, $\mathbf{I}_{i,in}(s)$ and $\mathbf{V}_{i,out}(s)$, $\mathbf{I}_{i,out}(s)$ represent the near and far end voltage and current sources for any i^{th} lossless section, superscript ' j ' represents the line number and $z_{i-1} = (i-1)l/n$. For the case of lossless MTL, the integral of (6.10) can be solved in closed form [51], [79] and when replaced back in (6.9) yields the frequency domain solution for the lossless MTLs exposed to incident fields as

$$\begin{pmatrix} \tilde{\mathbf{V}}_{i,out}(s) \\ -\tilde{\mathbf{I}}_{i,out}(s) \end{pmatrix} = e^{\frac{sBl}{n}} \begin{pmatrix} \tilde{\mathbf{V}}_{i,in}(s) \\ \tilde{\mathbf{I}}_{i,in}(s) \end{pmatrix} \quad (6.11)$$

where

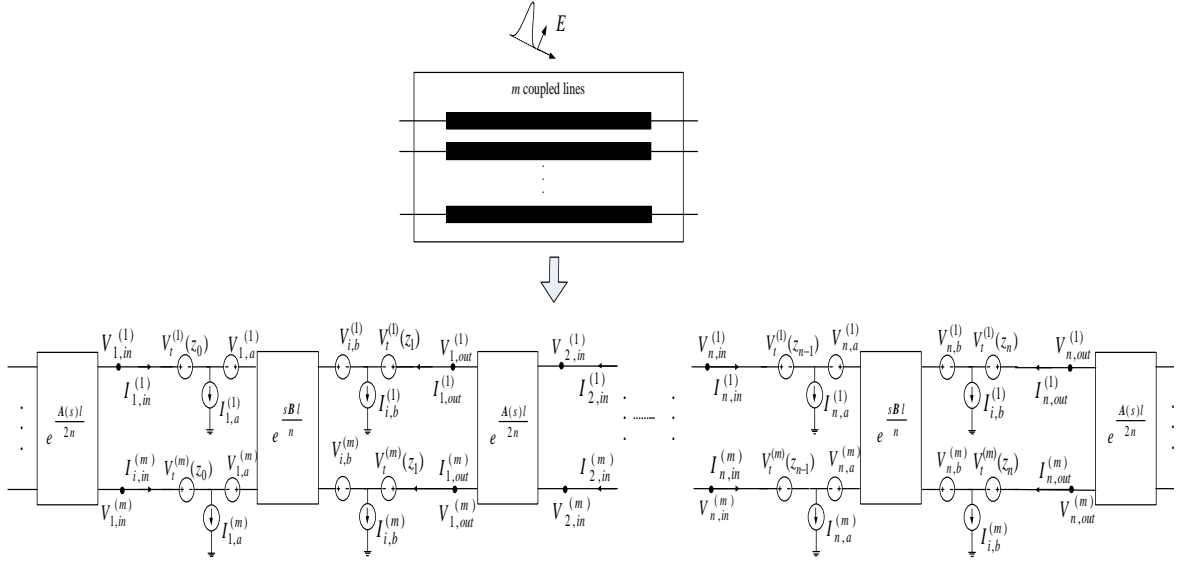


Figure 6-2: Discretization of MTL using DEFACT in the presence of incident fields.

$$\begin{aligned}
 \tilde{V}_{i,in}(s) &= V_{i,in}(s) - (V_t(z_{i-1}, s) - V_{i,a}(s)) \\
 \tilde{I}_{i,in}(s) &= I_{i,in}(s) + I_{i,a}(s) \\
 \tilde{V}_{i,out}(s) &= V_{i,out}(s) - (V_t(z_i, s) - V_{i,b}(s)) \\
 \tilde{I}_{i,out}(s) &= I_{i,out}(s) - I_{i,b}(s); \quad i = 1, 2, \dots, n
 \end{aligned} \tag{6.12}$$

and

$$\begin{aligned}
 \begin{bmatrix} V_{i,a}(s) \\ I_{i,a}(s) \end{bmatrix} &= e^{-s\beta_s z_{i-1}} E_0(s) \begin{bmatrix} \beta_z \mathbf{I} & -\mathbf{L}_\infty \\ -\mathbf{C}_\infty & \beta_z \mathbf{I} \end{bmatrix}^{-1} \begin{bmatrix} \mathbf{V}_{F1} \\ \mathbf{0} \end{bmatrix} \\
 \begin{bmatrix} V_{i,b}(s) \\ I_{i,b}(s) \end{bmatrix} &= e^{-s\beta_s z_i} E_0(s) \begin{bmatrix} \beta_z \mathbf{I} & -\mathbf{L}_\infty \\ -\mathbf{C}_\infty & \beta_z \mathbf{I} \end{bmatrix}^{-1} \begin{bmatrix} \mathbf{V}_{F1} \\ \mathbf{0} \end{bmatrix}
 \end{aligned} \tag{6.13}$$

Now, considering the line losses, the lossy sections ($e^{Al/2n}$) are incorporated between successive lossless sections to provide the equivalent circuit model for the entire MTL structure in presence of incident fields as illustrated in Fig. 6-2.

It is appreciated that the solution of the macromodel of Fig. 6-2 requires the inversion of the corresponding modified nodal analysis (MNA) matrix. The computational complexity

of directly inverting a matrix scales to $O(n^3)$ [79]. However, the matrices obtained by traditional circuit simulators are sparse by nature and can be solved more efficiently using sparse matrix routines at a cost of $O(n^\alpha)$ where typically $1.5 \leq \alpha \leq 2$ depending on the sparsity of the matrix [59]. For large distributed networks operating at high frequency, DEPACT macromodel of Fig. 6-2 may require many segments in Fig. 6-2 (i.e. n is large). For such cases, the super linear scaling of the computational cost for traditional circuit simulators is a major factor limiting their applicability. To address the above issue, the proposed contribution of applying the LP-WR algorithm [77] to perform EMI analysis is explained in the following section.

6.3 Development of Proposed WR Algorithm

This section begins by describing the methodology to longitudinally partition the DEPACT macromodel into compact subcircuits for transient analysis followed by the hybrid iterative techniques to solve the subcircuits.

6.3.1 Generation of Compact Subcircuits

In [51], a similarity transform is directly performed on (6.11) to decouple the m coupled lossless MTL into m single lossless lines. In this work, the similarity transform of [51] is modified in order to group the lumped sources due to the incident fields with the delayed sources due to the MoC which leads to a more scalable LP-WR algorithm. For this purpose, the proposed similarity transformation is performed on the quantities $V_{i,in}(s)$,

$I_{i,in}(s), V_{i,out}(s), I_{i,out}(s)$ (and not on $\tilde{V}_{i,in}(s), \tilde{I}_{i,in}(s), \tilde{V}_{i,out}(s), \tilde{I}_{i,out}(s)$) as

$$\begin{aligned} V_{i,in}(s) &= T_V \bar{V}_{i,in}(s); \quad I_{i,in}(s) = T_I \bar{I}_{i,in}(s) \\ V_{i,out}(s) &= T_V \bar{V}_{i,out}(s); \quad I_{i,out}(s) = T_I \bar{I}_{i,out}(s) \end{aligned} \quad (6.14)$$

where the matrices T_V and T_I are constant matrices chosen to diagonalize L_∞ and C_∞ and have the following properties [1]

$$\tilde{L} = T_V^{-1} L_\infty T_I; \quad \tilde{C} = T_I^{-1} C_\infty T_V; \quad T_V^t = T_I^{-1} \quad (6.15)$$

and $\tilde{L} = \text{diag}\{l_1, l_2, \dots, l_m\}$, $\tilde{C} = \text{diag}\{c_1, c_2, \dots, c_m\}$ are diagonal matrices. Replacing (6.14)-(6.15) in (6.11) and converting to time domain yields the following m decoupled MoC equations

$$\begin{aligned} \hat{V}_{i,in}(t) &= Z_0 \hat{I}_{i,in}(t) + W_{2i-1}(t) \\ \hat{V}_{i,out}(t) &= Z_0 \hat{I}_{i,out}(t) + W_{2i}(t) \quad i = 1, 2, \dots, n \end{aligned} \quad (6.16)$$

where

$$\begin{aligned} W_{2i-1}(t) &= [W_{2i-1}^{(1)}(t), \dots, W_{2i-1}^{(m)}(t)]^t \\ W_{2i}(t) &= [W_{2i}^{(1)}(t), \dots, W_{2i}^{(m)}(t)]^t \\ Z_0 &= [Z_0^{(1)}, \dots, Z_0^{(m)}]^t \\ W_{2i-1}^{(j)}(t) &= 2\hat{V}_{i,out}^{(j)}(t - \tau_j) - W_{2i}^{(j)}(t - \tau_j) \\ W_{2i}^{(j)}(t) &= 2\hat{V}_{i,in}^{(j)}(t - \tau_j) - W_{2i-1}^{(j)}(t - \tau_j); \quad j = 1, \dots, m \end{aligned} \quad (6.17)$$

and

$$\begin{aligned} \hat{V}_{i,in}(t) &= \bar{V}_{i,in}(t) - T_V^{-1} (V_t(z_{i-1}, t) - V_{i,a}(t)) \\ \hat{I}_{i,in}(t) &= \bar{I}_{i,in}(t) + T_I^{-1} I_{i,a}(t) \\ \hat{V}_{i,out}(t) &= \bar{V}_{i,out}(t) - T_V^{-1} (V_t(z_i, t) - V_{i,b}(t)) \\ \hat{I}_{i,out}(t) &= \bar{I}_{i,out}(t) - T_I^{-1} I_{i,b}(t); \quad i = 1, 2, \dots, n \end{aligned} \quad (6.18)$$

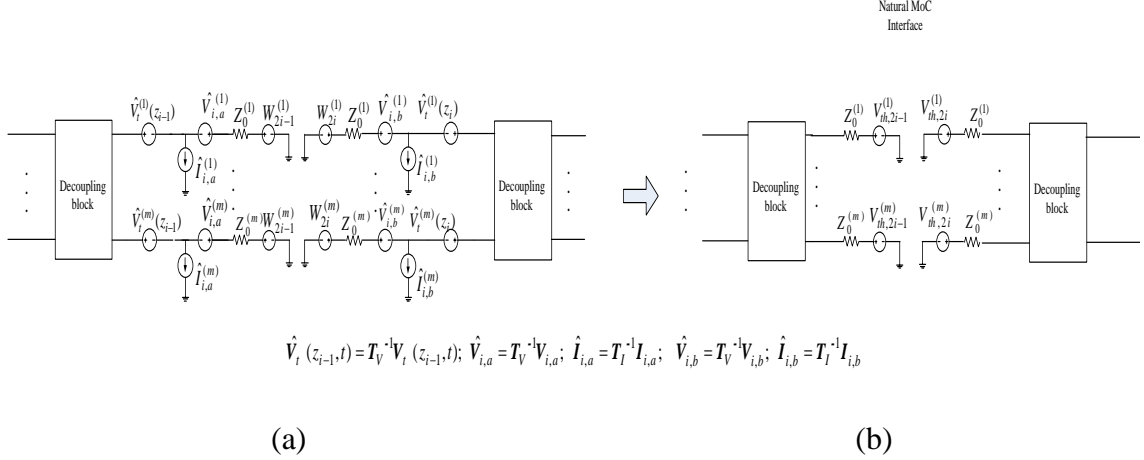


Figure 6-3: Proposed circuit representation of the incident field coupled with i^{th} lossless section. (a) Prior to grouping of the lumped sources. (b) After grouping of the lumped sources using (6.20).

The superscript ‘ j ’ represents the line number, $Z_0^{(j)} = \sqrt{l_j / c_j}$ and $\tau_j = l \sqrt{l_j c_j} / n$ represents the characteristic impedance and delay of each lossless section respectively of the j^{th} line. The variables $\bar{V}_{i,in}(t)$, $\bar{I}_{i,in}(t)$, $\bar{V}_{i,out}(t)$, $\bar{I}_{i,out}(t)$ and $V_{i,a}(t), I_{i,a}(t), V_{i,b}(t), I_{i,b}(t), V_t(z_{i-1}, t)$ are simply the time domain waveforms of the corresponding sources in (6.14) and (6.12) respectively. The lumped sources $V_{i,a}(s), I_{i,a}(s), V_{i,b}(s), I_{i,b}(s)$ and $V_t(z_{i-1}, t)$ can be obtained in a closed form manner using the direct inverse Laplace transform of (6.13) and (6.8) as

$$\begin{aligned} \begin{bmatrix} V_{i,a}(t) \\ I_{i,a}(t) \end{bmatrix} &= E_0(t - \beta_z z_{i-1}) \begin{bmatrix} \beta_z \mathbf{I} & -\mathbf{L}_\infty \\ -\mathbf{C}_\infty & \beta_z \mathbf{I} \end{bmatrix}^{-1} \begin{bmatrix} \mathbf{V}_{F1} \\ \mathbf{0} \end{bmatrix} \\ \begin{bmatrix} V_{i,b}(t) \\ I_{i,b}(t) \end{bmatrix} &= E_0(t - \beta_z z_i) \begin{bmatrix} \beta_z \mathbf{I} & -\mathbf{L}_\infty \\ -\mathbf{C}_\infty & \beta_z \mathbf{I} \end{bmatrix}^{-1} \begin{bmatrix} \mathbf{V}_{F1} \\ \mathbf{0} \end{bmatrix} \\ V_t(z_i, t) &= E_0(t - \beta_z z_i) \mathbf{V}_{F2} \end{aligned} \quad (6.19)$$

Based on (6.16)-(6.19), the representation of the i^{th} lossless section of Fig. 6-2 is illustrated in Fig. 6-3(a). In Fig. 6-3(a) the ‘decoupling block’ represent the lumped

dependent sources used to represent the transformation of (6.14). A key feature of the proposed representation of Fig. 6-3(a) is that the lumped sources due to the incident fields $V_{i,a}(t)$, $I_{i,a}(t)$, $V_{i,b}(t)$, $I_{i,b}(t)$ and $V_t(z_{i-1}, t)$ can be grouped together with $W_{2i-1}(t)$, $W_{2i}(t)$ into a compact Thevenins network as

$$\begin{aligned} V_{th,2i-1}(t) &= \mathbf{T}_V^{-1}(\mathbf{V}_t(z_{i-1}, t) - V_{i,a}(t)) + \mathbf{Z}_0 \mathbf{T}_I^{-1} \mathbf{I}_{i,a}(t) + W_{2i-1}(t) \\ V_{th,2i}(t) &= \mathbf{T}_V^{-1}(\mathbf{V}_t(z_i, t) - V_{i,b}(t)) - \mathbf{Z}_0 \mathbf{T}_I^{-1} \mathbf{I}_{i,b}(t) + W_{2i}(t) \\ \mathbf{R}_{th,2i-1} &= \mathbf{R}_{th,2i} = \mathbf{Z}_0 \end{aligned} \quad (6.20)$$

where $V_{th,2i-1}(t)$, $V_{th,2i}(t)$ represent the Thevenins equivalent sources and $\mathbf{R}_{th,2i-1}$, $\mathbf{R}_{th,2i}$ represent the Thevenins equivalent impedance for the i^{th} lossless section as displayed in Fig. 6-3(b). Replacing the expression for $W_{2i-1}(t)$, $W_{2i}(t)$ from (6.17) into (6.20), the Thevenins sources can be rewritten using delay linear equations for each decoupled line as

$$\begin{aligned} V_{th,2i-1}^{(j)}(t) &= 2\bar{V}_{i,out}^{(j)}(t - \tau_j) - W_{2i}^{(j)}(t - \tau_j) + V_{2i-1,x}^{(j)}(t) \\ V_{th,2i}^{(j)}(t) &= 2\bar{V}_{i,in}^{(j)}(t - \tau_j) - W_{2i-1}^{(j)}(t - \tau_j) - V_{2i,x}^{(j)}(t); \quad j = 1, \dots, m \end{aligned} \quad (6.21)$$

where

$$\begin{aligned} V_{2i-1,x}^{(j)}(t) &= Z_0^{(j)} \left[\mathbf{T}_I^{-1} \right]_j I_{i,a}^{(j)}(t) + \left[\mathbf{T}_V^{-1} \right]_j (V_t^{(j)}(z_{i-1}, t) - 2V_t^{(j)}(z_{i-1}, t - 2\tau_j)) - \left[\mathbf{T}_V^{-1} \right]_j (V_{i,a}^{(j)}(t) - 2V_{i,a}^{(j)}(t - 2\tau_j)) \\ V_{2i,x}^{(j)}(t) &= Z_0^{(j)} \left[\mathbf{T}_I^{-1} \right]_j I_{i,b}^{(j)}(t) + \left[\mathbf{T}_V^{-1} \right]_j (V_t^{(j)}(z_i, t) - V_{i,b}^{(j)}(t)) \end{aligned} \quad (6.22)$$

where $[A]_j$ represents the j^{th} row vector of \mathbf{A} . It is noted that the terms $V_{2i-1,x}^{(j)}$, $V_{2i,x}^{(j)}$ of (6.22) can be calculated offline and stored prior to the LP-WR iterations. From Fig. 6-3(b), it is observed that each lossless section provides a natural MoC interfaces (disjoin) across which current/voltage information is exchanged using the delayed linear equations

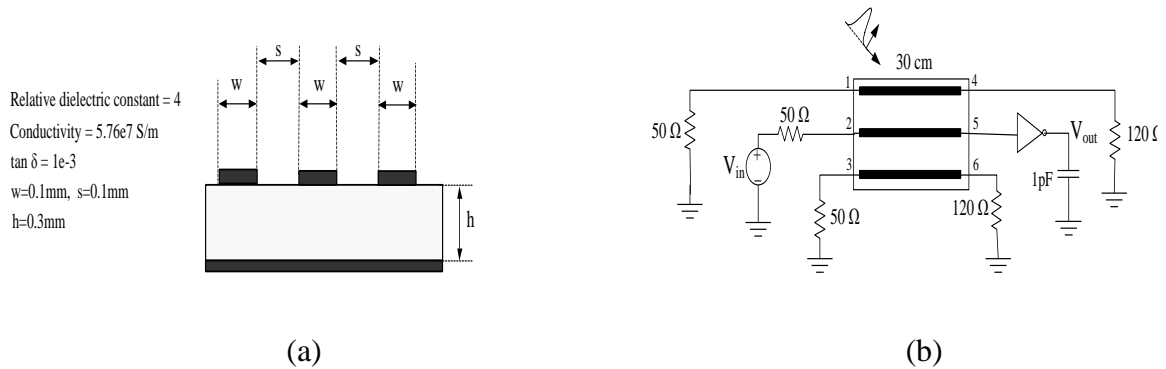


Figure 6-4: Three coupled microstrip lines of Example 1. (a) Geometry of the transmission lines. (b) Circuit layout of the transmission lines.

of (6.22). Partitioning the MTL macromodel of Fig. 6-3(b) along these natural MoC interfaces avoids the need of preserving the current/voltage continuity between subcircuits using Dirichlets transmission conditions and has been demonstrated to exhibit fast convergence for MTL networks in absence of incident fields [79]. Extending such a partitioning methodology for EMI analysis of MTLs based on the proposed representation of Fig. 6-3(b) leads to n subcircuits where the sources $V_{th,2i-1}(t)$, $V_{th,2i}(t)$ act as the relaxation sources responsible for maintaining the coupling between subcircuits. It is observed that based on (6.20) the size of the MNA matrices of each subcircuits is reduced by eliminating the variables $V_{i,a}(t)$, $I_{i,a}(t)$, $V_{i,b}(t)$, $I_{i,b}(t)$ (see Fig. 6-3(a) and 6-3(b)) thereby leading to more compact formulation of the subcircuits. Moreover, solution of each subcircuit now requires the prior knowledge of only the $2m$ waveforms ($V_{th,2i-1}(t)$, $V_{th,2i}(t)$) rather than the $5m$ waveforms of $V_{i-1,a}(t)$, $I_{i-1,a}(t)$, $V_t(z_{i-1},t)$, $W_{2i-2}(t)$, $W_{2i-1}(t)$ as would be required if the proposed partitioning scheme was directly applied to the circuit model of Fig. 6-2. The combination of the above factors leads to improved scalability of the proposed LP-WR algorithm. It is observed from Fig. 6-3(b) that the proposed partitioning scheme does not in any way affect the hybrid iterative scheme outlined in

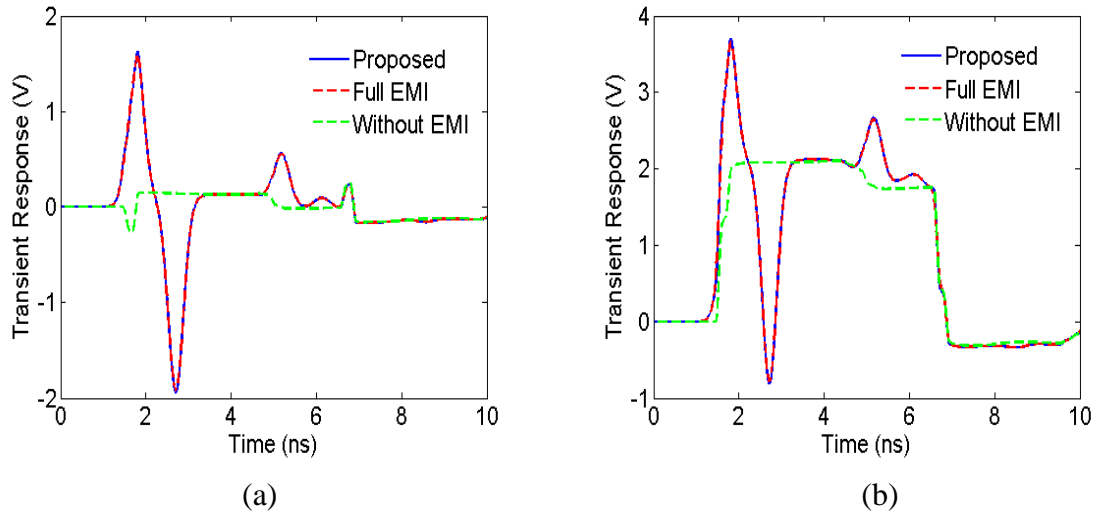


Figure 6-5: Transient response for Example 1 using the proposed LP-WR algorithm and full simulation. (a) Transient response at output port 4. (b) Transient response at output port 5.

Section 5.3.3. As a result, the benefits of the hybrid iterations are transferable to the problem of EMI analysis of MTL networks.

6.4 Numerical Examples

Three examples are presented in this section to demonstrate the validity and efficiency of the proposed work. For a fair comparison of the proposed LP-WR algorithm with full blown SPICE EMI simulation using segmentation techniques, this work is compared with the work of [51] (hereafter referred to as ‘full EMI’). Both techniques are performed using MATLAB 2011b on an UNIX server (66 GB RAM and 160 GB memory). All transient simulations are performed similar to Section 5.5.

Example 1: Three Coupled Microstrip Network: The objective of this example is to demonstrate the accuracy of the proposed LP-WR algorithm compared to the full EMI

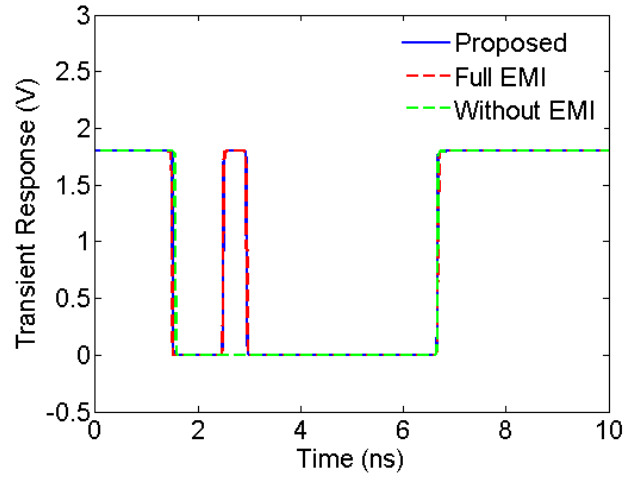


Figure 6-6: Transient response (V_{out}) of inverter in Example 1 with incident fields.

simulation. For this example a three coupled microstrip structure with the physical geometry as shown in Fig. 6-4(a) is considered. The per-unit-length parameters for this example are extracted from the HSPICE field solver [6] and are as given below

$$\begin{aligned}
 \mathbf{R} &= \text{diag} (6.79) \Omega / m \\
 \mathbf{L} &= \begin{bmatrix} 563.53 & 241.75 & 134.50 \\ 241.75 & 556.20 & 241.75 \\ 134.50 & 241.75 & 563.53 \end{bmatrix} nH / m \\
 \mathbf{C} &= \begin{bmatrix} 58.30 & -19.05 & -2.31 \\ -19.05 & 65.06 & -19.05 \\ -2.31 & -19.05 & 58.30 \end{bmatrix} pF / m \\
 \mathbf{R}_s &= \begin{bmatrix} 1.34 & -2.68e-3 & -0.11 \\ -2.68e-3 & 1.42 & -2.68e-3 \\ -0.11 & -2.68e-3 & 1.34 \end{bmatrix} m\Omega / m\sqrt{Hz} \\
 \mathbf{G} &= \mathbf{0}
 \end{aligned}$$

where $\mathbf{R}_l(s) = \mathbf{R}_s\sqrt{f}(1+j)$ represents the skin effect losses as a function of frequency f [6] and *diag* refers to a diagonal matrix. For the following analysis, the line length of the network is set to $l = 30$ cm. In this case, the number of subcircuits required for the proposed LP-WR is $n = 50$. The network is excited by a trapezoidal voltage source of rise

time $T_r = 0.1$ ns, pulse width 5 ns and amplitude of 1.8 V and loaded with a nonlinear inverter as shown in Fig 6-4(b). This network is also exposed to an incident electric field with Gaussian temporal waveform $E(t) = E_0(\exp(-(t - t_0)^2 / T^2))$ where $t_0 = 1$ ns and $T = 0.25$ ns, the peak amplitude $E_0 = 5$ kV/m, an elevation angle $\theta_p = 60^\circ$, azimuthal angle $\varphi_p = -60^\circ$ and a polarized angle $\theta_E = -90^\circ$ as in Fig. 6-1.

To illustrate the accuracy of the proposed algorithm, the network is solved using two methods - the hybrid iterative technique with improved initial guess and the full EMI simulation [51]. For the hybrid technique, the entire time span of analysis between 0-10 ns is divided into 20 time windows and the iterations for each time window are performed on a sequential platform (one processor). For a predefined error tolerance of $\eta = 1e-5$, the hybrid technique required 5 iterations to converge. The transient responses at the far end of the network using the proposed work are illustrated in Fig. 6-5 and exhibits good agreement with the full EMI simulation. Figure 6-6 shows the response of the output of the inverter (V_{out}) illustrating the false switching induced due to the incident field. The CPU cost of solving the full network (full EMI simulation) is 364 seconds and the CPU cost of the proposed LP-WR is 89 seconds (speedup of 4 times).

Example 2: Seven Microstrip Example: The objective of this example is to demonstrate the scalability of the proposed work with respect to the size of the network and the numbers of CPUs available for parallel processing. For this example a seven coupled microstrip structure of [79] with p.u.l. parameter matrices as given below is considered where $R_t(s) = R_s \sqrt{f} (1 + j)$ represents the skin effect losses as a function of frequency f [6]. In addition, the MTL is exposed to a incident electric field with a double exponential

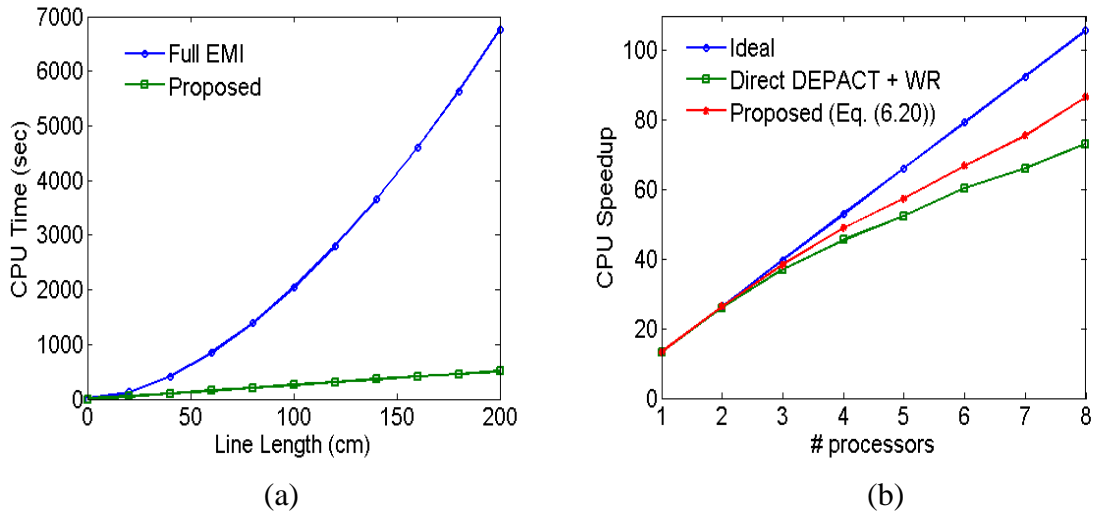


Figure 6-7: Computational efficiency of the proposed LP-WR algorithm over full EMI simulation. (a) Scaling of computational cost with line length (l) (b) Scaling of CPU speed up with number of CPUs (p) ($l = 200$ cm).

Table 6-1: Comparison of CPU run time for Example 2

# CPU	CPU Time (sec)			Speedup w. r. t. DEPACT (Eq. (6.20) + WR)	Speedup w. r. t. direct DEPACT+WR
	DEPACT (Eq. (6.20)) + WR	Direct DEPACT +WR	Full EMI		
1	511.50	511.49	6763.90	13.22	13.22
4	148.49	140.44		45.55	48.16
6	111.80	102.25		60.50	66.15
8	95.55	80.65		70.78	83.86

temporal waveform $E(t) = E_0(\exp(-\alpha t) - \exp(-\beta t))$ with $\alpha = 4 \times 10^8$ and $\beta = 10^9$, the peak amplitude $E_0 = 1 \text{ kV/m}$, an elevation angle $\theta_p = 60^\circ$, azimuthal angle $\varphi_p = -60^\circ$ and a polarized angle $\theta_E = -90^\circ$ as in Fig. 6-1.

This example begins with a demonstration of the scaling of the computational cost of the proposed work compared to full EMI simulation as the size of the network increases. For

this purpose the line length of the network (l) of the network is increased from 0 cm to 200 cm in steps of 10 cm. To accurately model the network, the numbers of subcircuits, n is increased in steps of 16 for each 10 cm step and ranges from 0 to 320. For each case, the network is solved using two methods – the proposed hybrid iterative technique with initial guess and the full EMI simulation of [51]. For the hybrid technique, the entire time span of analysis between 0-15 ns is divided into 20 time windows and the iterations for each time window are performed on a sequential platform. For a predefined error tolerance of $\eta = 1e-5$, the hybrid technique required on average 5 iterations to converge. The scaling of the computational cost of both proposed work and full EMI simulation with the line length (l) is shown in Fig. 6-7(a). It is observed from Fig. 6-7(a) that the proposed work scales almost linearly ($O(n)$) (as expected for the proposed LP-WR [77]) while the full EMI simulation of the original network scale super linearly as $O(n^\alpha)$ where $\alpha = 1.73$ for this example.

Next, the performance of the proposed work is demonstrated on a parallel platform. For this purpose the length of the network is fixed at the corner of our design space where $l = 200$ cm. The network is solved using three methods – full EMI simulation [51], the hybrid technique with initial guess where the partitioning is performed directly on the circuit of Fig. 6.2 (referred to as ‘direct DEPACT+WR’ in Fig. 6-7(b) and Table 6-1) and the same hybrid technique when the partitioning is performed on the more compact circuit of Fig. 6-3(b). Both hybrid techniques use the same time windowing as above and the iterations for each time window are performed on a parallel platform where the number of available CPUs are varied from $p = 1$ to $p = 8$ and the error tolerance set to $\eta = 1e-5$. The scaling of the CPU speed up offered by the proposed hybrid techniques over

full EMI simulations as a function of the number of processors is shown in Fig. 6-7(b) and summarized in Table 6-1. As expected, the speed up for both techniques scales efficiently with number of processors. However, when the partitioning is performed on the circuit of Fig. 6-7(b), the resultant savings in the size of the subcircuits and the communication overheads leads to a more improved scaling of the CPU speedup (closer to the ideal scenario where it is assumed that no communication or scheduling overheads are incurred) than that using the circuit of Fig. 6-2 without Thevenins representation.

6.5 Conclusion

In this chapter a longitudinal partitioning based waveform relaxation algorithm for parallel EMI analysis of MTL networks is presented. In the proposed work, an improved partitioning technique is proposed that replaces the Dirichlet's transmission conditions with delayed linear equations thereby accelerating the convergence of the waveform relaxation iterations. Moreover, the subcircuits are solved independently using a hybrid iterative technique that combines the fast convergence of the proposed GS technique with the parallelizability of the GJ technique. Techniques to compress the size of the subcircuits and reduce communication overheads are also provided. The proposed algorithm is found to scale only linearly with the size of the network and naturally lends itself for parallel implementations.

Chapter 7

7 Waveform Relaxation Algorithm for Fast Transient Analysis of Power Distribution Networks

7.1 Introduction

As demonstrated in the previous chapters, typically WR algorithms allow for a parallel, iterative simulation of a large network, thereby proving to be more efficient than conventional sequential algorithms. However, although WR algorithms have been extensively investigated for various problems including digital circuits [55] and transmission lines [54], [58]-[68], [76]-[79], they have found limited application for PDNs. This is due to the fact that in PDNs, every node is spatially connected in multiple directions leading to the subcircuits being tightly coupled and exhibiting slow convergence. Recently, a one dimensional (1D) partitioning based WR algorithms based on a lumped resistive-capacitive (RC) equivalent model for on-chip PDNs was proposed [69]. In the work of [69], regular V_{DD}/GND connections in on-chip PDNs were used as drain paths for the transient signal leading to good localization of the signal close to the

source and consequently efficient convergence.

In this chapter, a WR algorithm based on the DEPACT model for package/board level PDNs, as introduced in Chapter 3, is developed [80]-[81]. This paper extends the preliminary concepts proposed in [80] to provide a more efficient WR algorithm with improved scalability and convergence properties [81]. A key feature of this work is a 2-D partitioning methodology that physically divides the PDN in horizontal and vertical directions into rows and columns of subcircuits. In order to expedite the convergence of WR iterations, a regular distribution of the global decoupling capacitors over the package/board PDN structures is assumed. These decoupling capacitors serves as extra drain paths for the transient simultaneous switching noise (SSN) to ground, and in doing so, ensures that there is only weak SSN leakage from one subcircuit to the next i.e. coupling between the subcircuits is typically weak. As a result, the amplitude of the relaxation sources is very small and beginning the iterations with the initial guess of the relaxation sources set to the DC solution leads to fast convergence even for PDN examples. Furthermore, the advantages of a hybrid iterative technique that was proposed for transmission lines examples of Section 5.3.3 has been extended to this 2D PDN example as well. A proof of convergence of the proposed WR algorithm has also been provided. The overall algorithm is highly parallelizable and exhibits good scaling with both the size of the circuit matrices involved and the number of CPUs available. Numerical examples have been provided to illustrate the validity and efficiency of the proposed WR algorithm in comparison with solving the entire network.

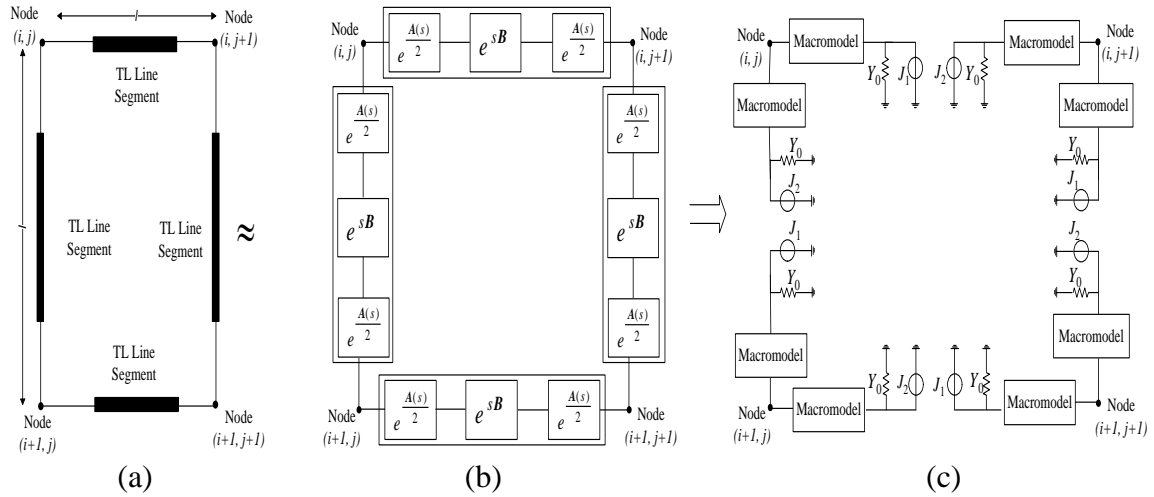


Figure 7-1: Equivalent circuit models for PDNs. (a) Transmission line representation of unit cell. (b) DEPACT representation of unit cell. (c) Equivalent circuit model of unit cell.

7.2 Development of the Proposed WR Algorithm

To illustrate the methodology to model PDNs using the DEPACT macromodel, a single layer, rectangular PDN is considered as shown in Fig. 2-1(a). Typical modeling algorithms for single layered PDNs are based on a 2D discretization of the Helmholtz wave equation over the planar area which translates to the division of the physical structure into rectangular unit cells as shown in Fig. 2-1(b). Each of the unit cells can further be modeled using the DEPACT macromodel as explained in details in Chapter 4 and [74]. The following subsection demonstrates the 2D proposed partitioning.

7.2.1 Proposed 2D Partitioning Methodology

Figure 7-1 illustrates the modeling of the unit cell where the transmission line segments of Fig. 7-1(a) is modeled using a single DEPACT section as shown in Fig. 7-1(b).

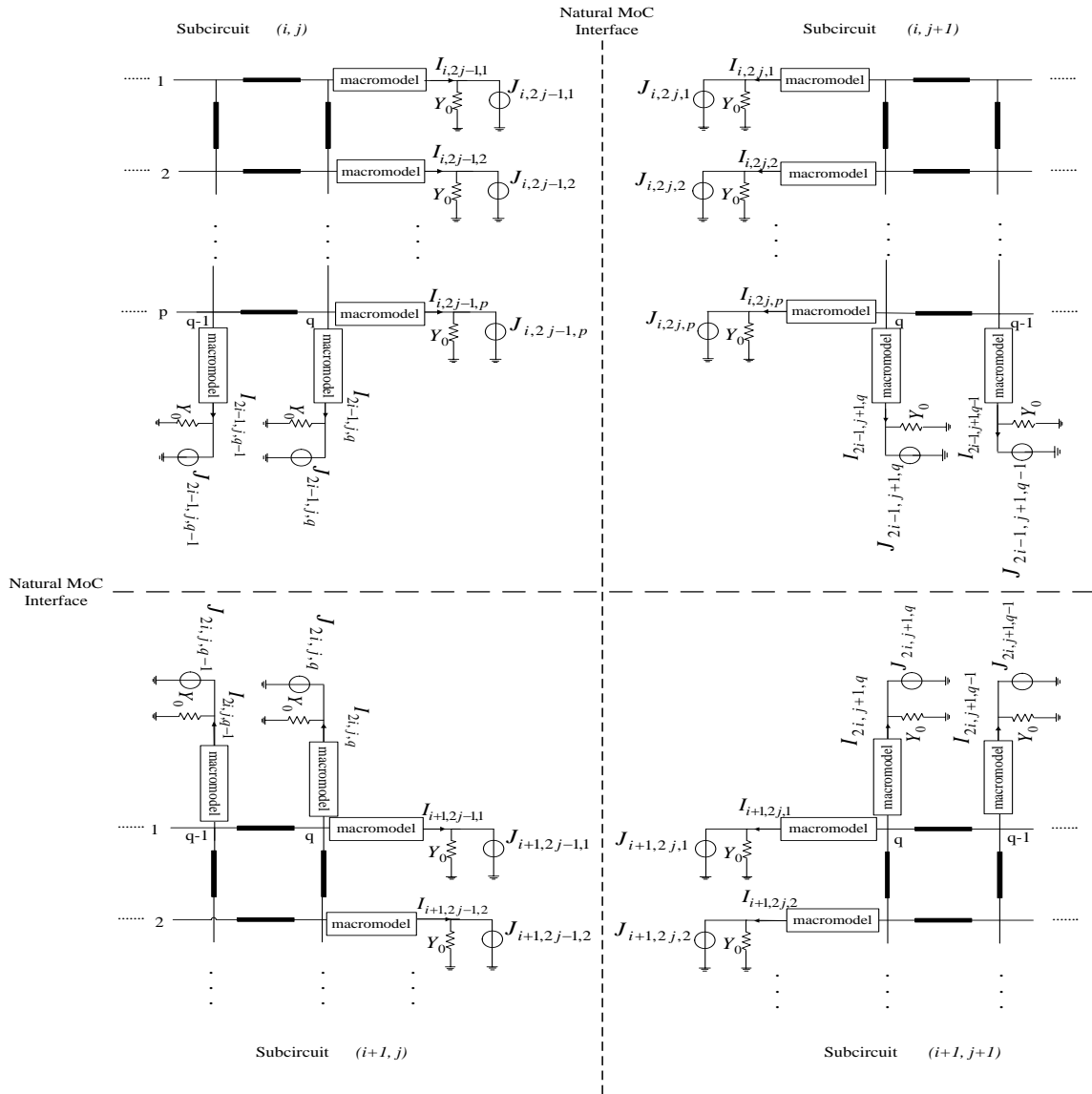


Figure 7-2: Partitioning along the natural MoC interfaces provided by DEFACT model.

Considering the lossless section between the nodes (i, j) and $(i, j+1)$ in Fig. 7-1(b) described in the time domain by the MoC as [1]

$$\begin{aligned}
 V_{i,j}(t) &= Z_0 I_{i,j}(t) + W_{i,j}(t) \\
 V_{i,j+1}(t) &= Z_0 I_{i,j+1}(t) + W_{i,j+1}(t) \\
 W_{i,j}(t) &= 2V_{i,j+1}(t - \tau) - W_{i,j+1}(t - \tau) \\
 W_{i,j+1}(t) &= 2V_{i,j}(t - \tau) - W_{i,j}(t - \tau);
 \end{aligned} \tag{7.1}$$

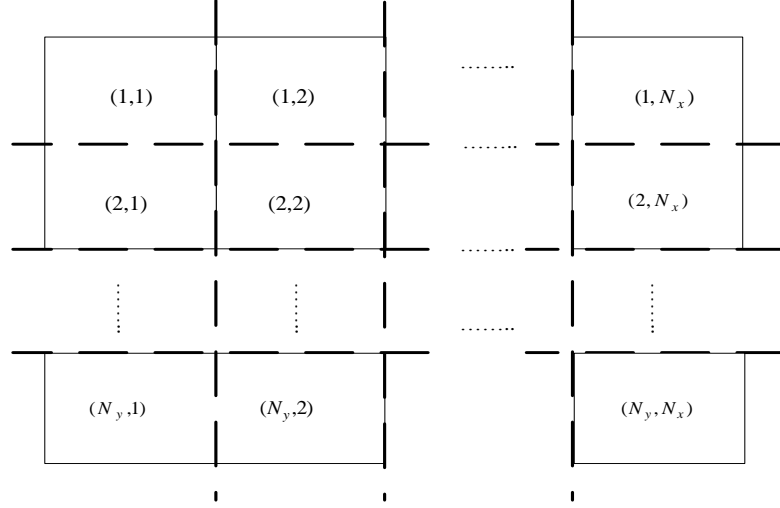


Figure 7-3: Proposed 2D partitioning

where $Z_0 = \sqrt{L_\infty / C_\infty}$ and $\tau = l\sqrt{L_\infty C_\infty}$ are the characteristic admittance and the delay of each lossless section respectively. The MoC equations of (7.1) can be realized by the simple equivalent circuit of Fig. 7-1(c). The natural MoC interfaces provided by the DEPACT allow for a 2D partitioning of the PDN structure and has been shown in detail in Fig. 7-2.

From Fig. 7-2, it is observed that p and q points of coupling exist between adjacent subcircuits along the Y and X direction respectively. Thus, the coupling between $(m, n)^{\text{th}}$ and $(m+1, n)^{\text{th}}$ subcircuit (X direction) is ensured by the relaxation sources $(W_{x,2m-1,\lambda}(t), W_{x,2m,\lambda}(t))$ (see Fig. 7-2) and can be expressed as

$$\begin{aligned} W_{x,2m-1,\lambda}(t) &= 2V_{x,2m,\lambda}(t - \tau) - W_{x,2m,\lambda}(t - \tau) \\ W_{x,2m,\lambda}(t) &= 2V_{x,2m-1,\lambda}(t - \tau) - W_{x,2m-1,\lambda}(t - \tau); \quad (n-1)p < \lambda \leq np \end{aligned} \quad (7.2)$$

Similarly, the coupling between $(m, n)^{\text{th}}$ and $(m, n+1)^{\text{th}}$ subcircuits (Y direction) is ensured by the relaxation sources $(W_{y,2n-1,\mu}(t), W_{y,2n,\mu}(t))$ (see Fig. 7-2) and can be expressed as

$$\begin{aligned}
W_{y,2n-1,\mu}(t) &= 2V_{y,2n,\mu}(t-\tau) - W_{y,2n,\mu}(t-\tau) \\
W_{y,2n,\mu}(t) &= 2V_{y,2n-1,\mu}(t-\tau) - W_{y,2n-1,\mu}(t-\tau); \quad (n-1)p < \lambda \leq np
\end{aligned} \tag{7.3}$$

The above methodology partitions the PDN in 2D into rows and columns of subcircuits as shown in Fig. 7-3 and results in smaller subcircuits than [69] where the PDN was partitioned into block of rows. Since the cost of solving each subcircuit scales super linearly with the size of the subcircuit, the proposed partitioning methodology provides more efficient scaling of the WR algorithm. However, despite the advantages of the proposed partitioning methodology, since each node of Fig. 2-1(b) is spatially connected to other nodes in multiple directions, partitioning the PDN at the natural MoC interfaces still may not yield fast convergence. Hence, techniques to expedite convergence based on placement of decoupling capacitors and extension of the hybrid iterative algorithm of Chapter 5 to the PDN problem is discussed next.

7.2.2 Effect of Decoupling Capacitors

The localization effect due to multiple V_{DD}/GND connections found on on-chip PDN structures has already been found to accelerate the WR iterations [69]. In this work, the localization properties due to a regular arrangement of global decoupling capacitors found on PCB power buses are utilized to accelerate the WR iterations as explained below.

Typical PDN designs at the PCB level include the uniform distribution of global decoupling capacitors over the entire PDN surface to mitigate the effects of SSN [5], [82]-[83]. These decoupling capacitors are represented as a series equivalent resistive-inductive-capacitive (RLC) model. As a result, for frequencies close to the resonance

frequency $f_s = 1/(2\pi\sqrt{LC})$, the decoupling capacitor behaves like a predominantly resistive path to ground, where due to the high conductivity of the electrode, the path resistance (R) is typically very small [5]. Considering the SSN propagating across any $(i,j)^{\text{th}}$ subcircuit of Fig. 7-3, components of the transient current with frequencies located close to f_s will feed into these low impedance paths (i.e. decoupling capacitors) local to the $(i,j)^{\text{th}}$ subcircuit rather than those located in the neighboring subcircuit due to the additional path resistance encountered in crossing the partition interface (similar to what has been observed for the V_{DD}/GND connections in [69]). As a result, for the above noise components, the decoupling capacitors local to each subcircuit ensure reasonable localization of the SSN signal within that subcircuit and consequently the leakage of the SSN signal propagating across the partitioning interfaces is relatively weak (i.e. the relaxation sources has weak amplitude). As a result, even for large amplitude SSN signals as observed during resonance, an initial guess of the relaxation sources set to the DC solution is sufficient for convergence.

To ensure the above localization effect, the partitioning of Fig. 7-2 must ensure sufficient decoupling capacitors local to each subcircuit. It is expected that increasing the size of subcircuits to incorporate more decoupling capacitors within each subcircuit would lead to even better localization of the signal and hence, improved convergence. However, with the increase in subcircuit size, the CPU cost of solving each subcircuit would also increase super linearly leading to a poor scaling of the WR algorithm. It was observed through various experiments with different PDN structures that for subcircuits containing two decoupling capacitors in the horizontal and vertical directions each (i.e. total four decoupling capacitors) provide good localization of the noise signal in either directions

and consequently was a good compromise between the CPU cost of solving each subcircuit and the speed of convergence. This will be illustrated through a numerical example in Section VI.

The above localization effect is maximum near the resonance frequency of the decoupling capacitor (f_s) and decreases as we move away from f_s . In order to ensure that the rate of convergence remains smooth over the entire bandwidth of operation, the hybrid iterative technique proposed in Chapter 5 has extended to PDNs, as described next.

7.2.3 2D Hybrid Iterative Technique

Once the PDN has been partitioned into subcircuits, these subcircuits can be solved independently in an iterative manner. Typically two techniques exist for the iterative solution of the subcircuits – the Gauss-Seidel (GS) and the Gauss-Jacobi (GJ) techniques [55]. In [77], a hybrid iterative technique that combined the complimentary features of GS with that of GJ was proposed for 1D transmission line networks. In this subsection, the 1D iterative technique has been extended to the 2D problem with PDNs.

To begin the hybrid iterative technique, all the subcircuits are divided into two groups – group A and B where the $(i, j)^{\text{th}}$ subcircuit is placed in group A if $i+j$ is an even number or else it is placed in group B if $i+j$ is an odd number. The total number of subcircuits within each group is defined as

$$\begin{aligned} n_A &= [N_x N_y / 2] - \text{group A} \\ n_B &= N_x N_y - [N_x N_y / 2] - \text{group B} \end{aligned} \tag{7.4}$$

and $[x]$ represents the least integer greater than x . From Fig. 7-3, it is observed that such a grouping ensures that subcircuits of one group do not share any partitioning interface with (i.e. are not coupled to) any other subcircuits in the same group but are coupled to subcircuits from the other group. As a result, the exchange of waveforms required to update the relaxation sources only occurs between subcircuits of different groups and never between those of the same group. This grouping can be exploited using a nested iterative technique similar to that of Section 5.3.3. The outer iteration solves group A and B in sequence (using GS) and updates the relaxation sources after every group solution. The inner iteration solves the subcircuits within each group in parallel (using GJ). This forms the basis of the proposed hybrid iterative technique.

In each iteration, the GS sequence begins with the group A before proceeding to the group B. Prior to beginning the k^{th} iteration, it is assumed that the $k-1^{\text{th}}$ iteration has been completed for all N subcircuits and the waveforms of the relaxation sources responsible for exciting the n_A subcircuits of group A have been updated to

$$R_A^{(k-1)} = \{W_{x,2m-2,\lambda}^{(k-1)}(t), W_{x,2m-1,\lambda}^{(k-1)}(t), W_{y,2n-2,\mu}^{(k-1)}(t), W_{y,2n-1,\mu}^{(k-1)}(t)\} \quad (7.5)$$

where $(n-1)p < \lambda \leq np$; $(m-1)q < \mu \leq mq$ and $(m+n)$ is even. If $k = 1$, the waveforms of $R_A^{(0)}$ are simply the initial guesses. Using the relaxation sources with known waveforms of (7.5) as input for the corresponding subcircuits of group A translates to the following terminal conditions (Fig. 7-2)

$$\begin{aligned}
V_{x,2m-2,\lambda}^{(k)}(t) &= Z_0 I_{x,2m-2,\lambda}^{(k)}(t) + W_{x,2m-2,\lambda}^{(k-1)}(t) \\
V_{x,2m-1,\lambda}^{(k)}(t) &= Z_0 I_{x,2m-1,\lambda}^{(k)}(t) + W_{x,2m-1,\lambda}^{(k-1)}(t) \\
V_{y,2n-2,\mu}^{(k)}(t) &= Z_0 I_{y,2n-2,\mu}^{(k)}(t) + W_{y,2n-2,\mu}^{(k-1)}(t) \\
V_{y,2n-1,\mu}^{(k)}(t) &= Z_0 I_{y,2n-1,\mu}^{(k)}(t) + W_{y,2n-1,\mu}^{(k-1)}(t)
\end{aligned} \tag{7.6}$$

The terminal conditions of (7.6) along with the equations arising from the DEFACT representation of the transmission line segments within each subcircuit, together form the set of delayed ordinary differential equations (DODE) describing each subcircuit of group A. These subcircuits can now be solved in parallel on a multiprocessor machine using GJ for a self consistent solution of the left hand side of (7.6) as

$$V_A^{(k)} = \{V_{x,2m-2,\lambda}^{(k)}(t), V_{x,2m-1,\lambda}^{(k)}(t), V_{y,2n-2,\mu}^{(k)}(t), V_{y,2n-1,\mu}^{(k)}(t)\} \tag{7.7}$$

Once the GJ for group A is concluded, the waveforms of the relaxation sources exciting the subcircuits of group B are updated using the delayed MoC equations of as

$$\begin{aligned}
W_{x,2m-3,\lambda}^{(k)}(t) &= 2V_{x,2m-2,\lambda}^{(k)}(t-\tau) - W_{x,2m-2,\lambda}^{(k-1)}(t-\tau) \\
W_{x,2m,\lambda}^{(k)}(t) &= 2V_{x,2m-1,\lambda}^{(k)}(t-\tau) - W_{x,2m-1,\lambda}^{(k-1)}(t-\tau) \\
W_{y,2n-3,\mu}^{(k)}(t) &= 2V_{y,2n-2,\mu}^{(k)}(t-\tau) - W_{y,2n-2,\mu}^{(k-1)}(t-\tau) \\
W_{y,2n,\mu}^{(k)}(t) &= 2V_{y,2n-1,\mu}^{(k)}(t-\tau) - W_{y,2n-1,\mu}^{(k-1)}(t-\tau)
\end{aligned} \tag{7.8}$$

where the waveforms on the right hand side are already known from (7.5) and (7.7). The equations of (7.8) being decoupled, can be solved in parallel. The above updated relaxation sources responsible for exciting the subcircuits of group B are expressed similar to (7.5) as

$$R_B^{(k)} = \{W_{x,2m-3,\lambda}^{(k)}(t), W_{x,2m,\lambda}^{(k)}(t), W_{y,2n-3,\mu}^{(k)}(t), W_{y,2n,\mu}^{(k)}(t)\} \tag{7.9}$$

Using the relaxation sources of (7.9) as the input excitation for the corresponding subcircuits of group B translates to the following terminal conditions (Fig. 7-2)

$$\begin{aligned}
 V_{x,2m-3,\lambda}^{(k)}(t) &= Z_0 I_{x,2m-3,\lambda}^{(k)}(t) + W_{x,2m-3,\lambda}^{(k)}(t) \\
 V_{x,2m,\lambda}^{(k)}(t) &= Z_0 I_{x,2m,\lambda}^{(k)}(t) + W_{x,2m,\lambda}^{(k)}(t) \\
 V_{y,2n-3,\mu}^{(k)}(t) &= Z_0 I_{y,2n-3,\mu}^{(k)}(t) + W_{y,2n-3,\mu}^{(k)}(t) \\
 V_{y,2n,\mu}^{(k)}(t) &= Z_0 I_{y,2n,\mu}^{(k)}(t) + W_{y,2n,\mu}^{(k)}(t)
 \end{aligned} \tag{7.10}$$

Using the terminal condition of (7.10), the subcircuits in group B can be solved in parallel using GJ for a self-consistent solution of the left hand side of (7.10) as

$$V_B^{(k)} = \{V_{x,2m-3,\lambda}^{(k)}(t), V_{x,2m,\lambda}^{(k)}(t), V_{y,2n-3,\mu}^{(k)}(t), V_{y,2n,\mu}^{(k)}(t)\} \tag{7.11}$$

Based on (7.11), the waveforms of the relaxation sources exciting the subcircuits of group A are updated for the $k+1^{\text{th}}$ iteration using the delayed MoC equations of as

$$\begin{aligned}
 W_{x,2m-2,\lambda}^{(k)}(t) &= 2V_{x,2m-3,\lambda}^{(k)}(t-\tau) - W_{x,2m-3,\lambda}^{(k)}(t-\tau) \\
 W_{x,2m-1,\lambda}^{(k)}(t) &= 2V_{x,2m,\lambda}^{(k)}(t-\tau) - W_{x,2m,\lambda}^{(k)}(t-\tau) \\
 W_{y,2n-2,\mu}^{(k)}(t) &= 2V_{y,2n-3,\mu}^{(k)}(t-\tau) - W_{y,2n-3,\mu}^{(k)}(t-\tau) \\
 W_{y,2n-1,\mu}^{(k)}(t) &= 2V_{y,2n,\mu}^{(k)}(t-\tau) - W_{y,2n,\mu}^{(k)}(t-\tau)
 \end{aligned} \tag{7.12}$$

where the waveforms on the right hand side are already known from (7.9) and (7.11). This iterative cycle continues till the absolute error satisfies a predefined tolerance limit. It is noted that the hybrid technique provides more frequent exchange of waveforms using (7.8), (7.12) compared to traditional GJ which allows only a single exchange. As a result, the hybrid technique exhibits better convergence than GJ. Moreover, the subcircuits in group A or B can still be solved in parallel unlike a full blown GS technique.

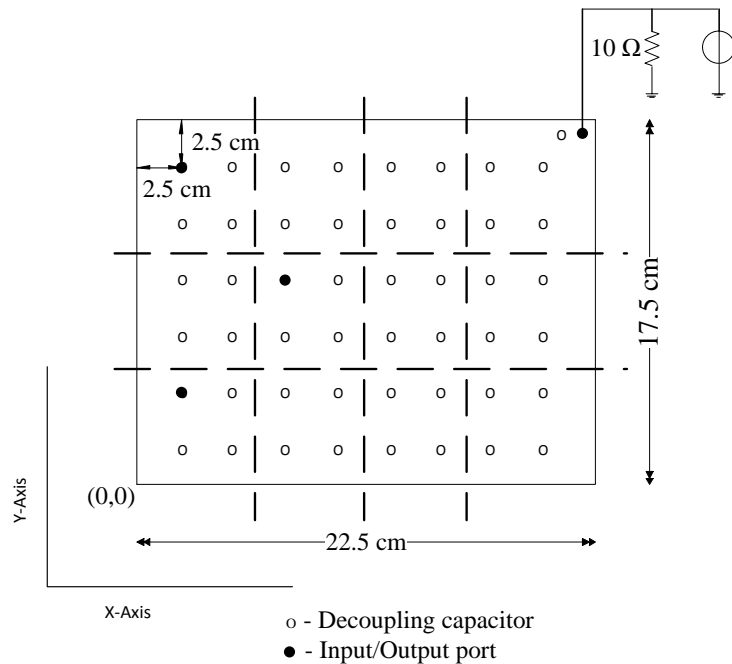


Figure 7-4: PDN structure of Example 1

7.3 Numerical Examples

Two examples are presented in this section to demonstrate the validity and efficiency of the proposed work. For a fair comparison of the WR algorithm with full simulation of the PDN, this work is compared with the work of [74] (hereafter referred to as ‘full EMI’). Both techniques are performed using MATLAB 2011b on an UNIX server (66 GB RAM and 160 GB memory). All transient simulations are performed similar to Section 5.5.

Example 1: The objective of this example is to demonstrate the robustness of the proposed partitioning methodology. For this example a rectangular PDN structure with the physical dimensions shown in Fig. 7-4 is considered. The signal and ground planes are made of copper with thickness $t = 0.025$ mm and separated by $d = 1.1$ mm thick FR4 dielectric ($\epsilon_r = 4.5$). The PDN is discretized into an orthogonal grid of transmission lines

where the length of each line segment is set to 0.5 cm (i.e. $N_c = 46$, $N_r = 36$ of Fig. 2-1). The PDN is populated with a uniform distribution of 48 global decoupling capacitors and a single local decoupling capacitor (0.5 cm away from the SSN source as shown in Fig. 7-4). Each decoupling capacitor belongs to the package size 0805 family and is modeled as a lumped series RLC models where $R = 85\text{m}\Omega$, $L = 0.5\text{nH}$, $C = 7.3\text{nF}$ [83]. The input port is located at Port A (22, 17) while three output ports are located at Port B (2.5, 15), Port C (7.5, 10) and Port D (2.5, 5). To mimic the injected transient current, the input source is modeled as a Norton's equivalent current source with a resistance of 10Ω in parallel. The input waveform is a triangular pulse with rise time $T_r = 0.2\text{ ns}$ and amplitude 100mA. The p. u. l. parameters of the transmission line segment are obtained from the physical and electrical characteristics of the PDN as explained in [74].

To illustrate the localization phenomenon and its effect on the convergence of WR iterations, the above PDN structure is analyzed for two cases – in presence of the decoupling capacitors of Fig. 7-4 (network one) and when no decoupling capacitors are present (network two). For network one, the PDN is partitioned as shown in Fig. 7-4 (two decoupling capacitors in the X and Y directions) yielding a total of $N = 12$ subcircuits ($N_x = 4$, $N_y = 3$ in Fig. 7-3). To provide a fair comparison between the two networks, network two is also partitioned in a similar manner as network one. Figure 7-5 shows the result of the WR iterations at port D for both networks using GS on a sequential platform (number of processors (p) = 1) where the initial guess of the waveforms of the relaxation sources is set to the zero and the error tolerance is set to $\eta = 1\text{e-}6$. It is observed that for network one, the amount of the SSN signal reaching the port D from port A is significantly less than for network two. This is due to the fact that for network one, the decoupling

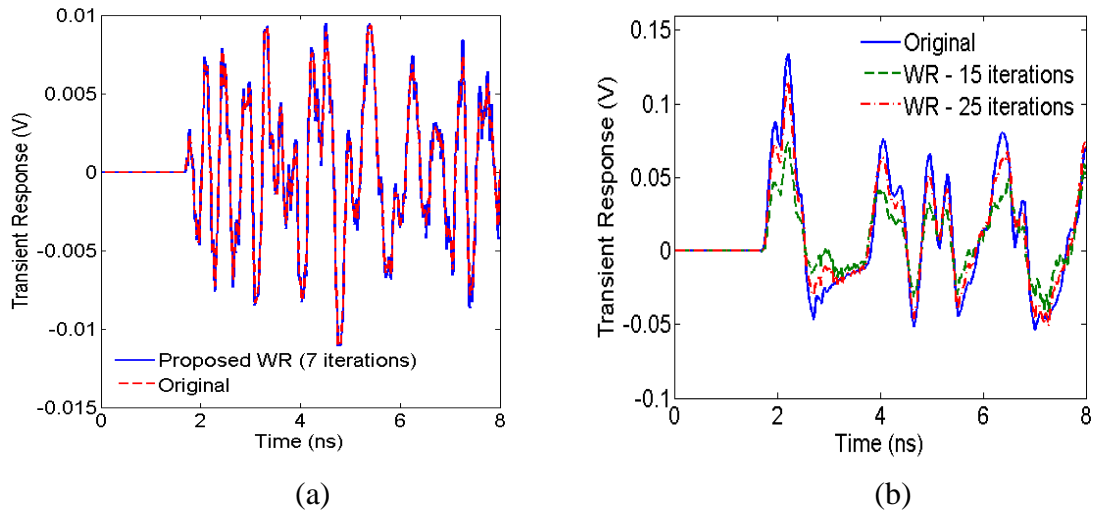


Figure 7-5: Transient response for Example 2 using proposed WR algorithm and full simulation. (a) Transient response at output port B considering decoupling capacitors. (b) Transient response at output port B without decoupling capacitors.

Table 7-1: Change in rate of convergence with number of decoupling capacitors for Example 1

Test case	# Decoupling capacitors per subcircuit in X direction	# Decoupling capacitors per subcircuit in Y direction	# Iterations
1	1	1	12
2	2	1	9
3	2	2	7
4	2	3	7
5	4	3	7

capacitors local to each subcircuit provide reasonable localization of the SSN within that subcircuit by acting as alternative current drain paths and thereby ensure that the strength of SSN propagating between two adjacent subcircuits between ports A and D is relatively weak. As a result, using an initial guess of the relaxation sources set to DC solution of zero converges to the actual solution of network one within 7 iterations but fails to

capture the high amplitude waveform of network two even after 25 iterations.

Next, the dependence of the speed of convergence on the number of decoupling capacitors within each subcircuit is investigated. For this purpose five test cases for the PDN structure of Fig. 7-4 are described in Table 7-1. It is observed from Table 7-1 that the size of the subcircuits are steadily increased from test case 1 to 5 to progressively include more decoupling capacitors within themselves. The WR iterations are performed for each test case using Gauss-Seidel ($p = 1$) with an initial guess of the relaxation sources set to zero and an error tolerance of $\eta = 1e-6$. The variations in speed of convergence with the number of decoupling capacitors within each subcircuit are shown in Table 7-1. It is noted that as size of the subcircuits are increased from test case 1 to test case 3, the increase in number of decoupling capacitors lead to better localization and consequently better convergence. However, beyond test case three, there is negligible improvement in the convergence speed. This is because, increasing the size of each subcircuits also leads to an increase in the number of coupling points between adjacent subcircuit which impedes the convergence and thus offsets any benefit of including additional decoupling capacitors. Furthermore, with the increase in subcircuit size, the CPU cost of solving each subcircuit would also increase super linearly leading to a poor scaling of the WR algorithm.

It was observed through various experiments with different PDN structures that the subcircuits containing two decoupling capacitors in the X and Y directions each (i.e. test case 3 for this example) provide good localization of the noise signal in either directions and consequently was a good compromise between the CPU cost of solving each subcircuit and the speed of convergence.

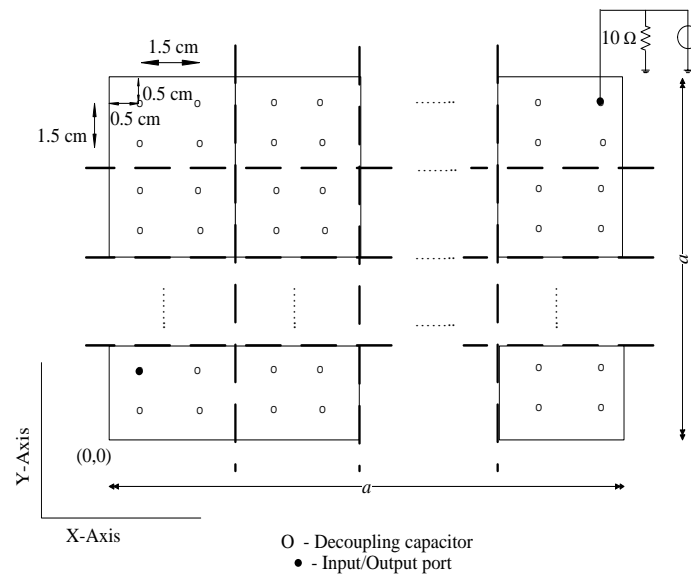


Figure 7-6: PDN structure for Example 2.

Example 2: The objective of this example is to illustrate the computational efficiency of the proposed work over full simulation of the PDN [74]. For this example, a PDN structure of variable dimension a cm as shown in Fig. 7-6 is considered. The signal and ground planes are made of copper of thickness $t = 0.025$ mm and separated by $d = 1.1$ mm thick FR4 dielectric ($\epsilon_r = 4.5$). The PDN is discretized into an orthogonal grid of transmission lines where the length of each line segment was set to 0.5 cm. The PDN contains a uniform distribution of global decoupling capacitors spaced 1.5 cm from each other and 0.5 cm from the PDN edges (Fig. 7-6) where each decoupling capacitor belongs to the package size 0805 family [83]. The input port is located at Port A ($a-0.5, a-0.5$) and an output port is located at Port B (0.5, 2). The input source is modeled as a Norton's equivalent current similar to Example 1 and has a triangular pulse waveform with rise time $T_r = 0.2$ ns and amplitude 100mA. The p. u. l. parameters of the transmission line segment are obtained from the physical and electrical characteristics of the PDN as

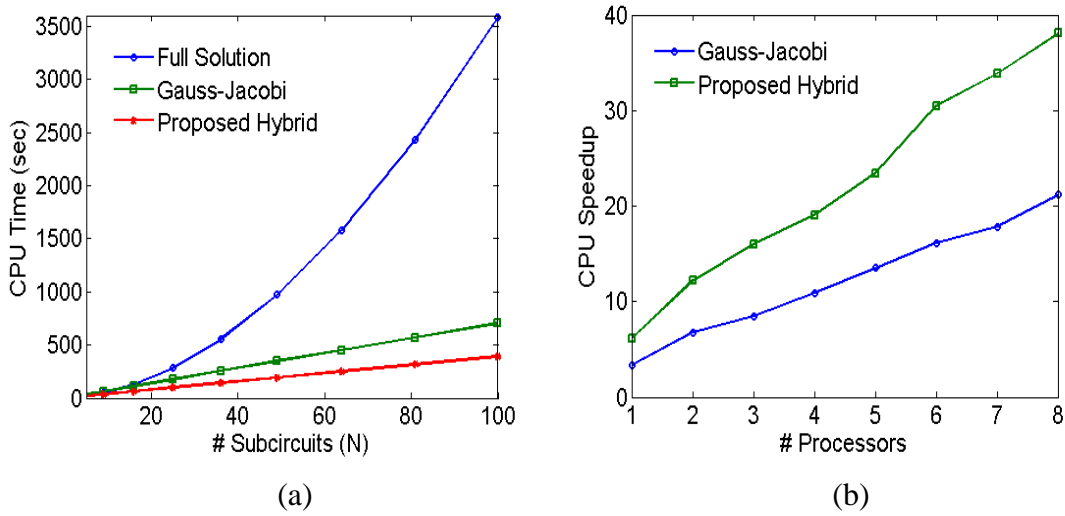


Figure: 7-7: Scaling of computational cost for Example 2. (a) Scaling of computational cost with number of subcircuits (N_0) (number of CPUs set to 1). (b) Scaling of CPU speed up with number of CPUs (p) ($N_0 = 100$).

Table 7-2: Comparison of CPU run time for Example 2

# CPU	CPU Time (sec)			Speedup w. r. t. Gauss Jacobi	Speedup w. r. t. Hybrid
	Gauss Jacobi	Hybrid	Full Simulation		
1	1057.00	587.25	3579.00	3.38	6.09
4	327.70	187.92		10.92	19.04
6	222.35	117.45		16.09	30.47
8	165.45	93.96		21.63	38.09

explained in [74]. The PDN is partitioned as shown in Fig. 7-6 yielding a total of $N = N_x N_y$ subcircuits where for this example $N_x = N_y = N_0$.

To demonstrate the scaling of the computational cost with size of the network, the dimensions of the PDN is increased from $a = 5.5$ cm to $a = 29.5$ cm in steps of 3 cm. This corresponds to N_0 increasing from 0 to 8 in unit steps. For each case, the PDN is solved using three techniques – proposed WR with hybrid technique, proposed WR with

traditional GJ technique and the full PDN simulation [74]. For a fair comparison, both WR algorithms use time windowing [55] where the entire time span ranging between 0-8ns is divided into 20 time windows. The WR iterations are performed on a sequential platform ($p = 1$) with the predefined error tolerance set to $\eta = 1\text{e-}6$. For this particular error tolerance, the number of iterations required for the hybrid technique is 5 while that required for the GJ was 9. The scaling of the computational cost of the WR algorithms and full PDN simulation [74] with the size of the PDN (i.e. N) is shown in Fig. 7-7. It is observed from Fig. 7-7(a) that the CPU cost for both GJ and the hybrid algorithm scales almost linearly with number of subcircuits ($O(N)$). This scaling of the CPU cost with the number of subcircuits is similar to that reported for typical WR algorithms [77], [79]. The CPU cost of the full PDN solution scale super linearly as $O(n^\alpha)$ where $\alpha = 1.83$ for this example. Moreover, the 2D hybrid iterative technique of Section 7.2.3 provides faster convergence than that due to GJ.

Next, the performance of the proposed work is demonstrated on a parallel platform. The dimensions of the PDN is fixed at the corner of our design space where $a = 29.5$ cm. The WR iterations are performed on a parallel processing platform where number of processors are varied from $p = 1$ to $p = 8$ for the same error tolerance as before. The CPU speed up offered by both WR algorithms over full simulation of the PDN [74] is shown in Fig. 7-7(b) and summarized in Table 7-2. The speed ups for either iterative technique scale almost linearly with number of processors, thereby demonstrating the high parallelizability of both. However, the 2D hybrid iterative technique is still much faster than the GJ. The minor deviation of Fig. 7-7(b) from the exactly linear scaling with

respect to number of CPUs (p) is due to the incurred communication overheads between processors and the and scheduling overheads for the time windows.

7.4 Conclusions

In this chapter a waveform relaxation algorithm for the efficient transient analysis of power distribution planes is presented. The proposed methodology represents the network using an orthogonal grid of transmission line segments where a delay extraction based macromodel is used to represent each line segment in time domain. Novel partitioning and iterative techniques are proposed for fast convergence and improved scalability of the proposed relaxation algorithm. The overall algorithm is highly parallelizable and exhibits good scaling with both the size of the circuit matrices involved and the number of CPUs available.

Chapter 8

8 Summary and Future Work

8.1 Summary

The objective of this thesis is to develop efficient algorithms for computer aided signal and power integrity analyses in high speed packaging. This thesis typically derives delay extraction based algorithms and parallelizable solution strategies for the accurate yet efficient broadband macromodeling of high speed interconnects and PDNs. The major contributions of this thesis are summarized below.

Firstly, a delay extraction based IFFT algorithm has been developed for the macromodeling of interconnect networks characterized by their frequency domain, multiport Y parameter matrix. This algorithm exploits a time-frequency decomposition (Gabor transformation) to explicitly extract multiple delays from the tabulated data arising due to the multiple reflections of the signal at the I/O terminals. This is followed by a Hilbert transform to capture the attenuation loss term corresponding to each delay. Thereafter, a simple IFFT operation converts the frequency domain Y parameter data into

a sum of delayed data in the time domain that is more accurate than traditional IFFT and single delay extraction based IFFT techniques. Numerical convolution of the time domain \mathbf{Y} parameter matrix with the input yields the transient network response.

Secondly, a delay extraction based macromodeling algorithm has been presented to model high speed PDNs. This algorithm is based on extending the DEFACT algorithm to single layered (2D) and even multilayered (3D) PDN structures including holes, apertures and irregular geometry thereby providing more efficient broadband macromodels than the existing quasi-static lumped models.

Thirdly, a longitudinal partitioning based WR (LP-WR) algorithm using delay extraction has been developed for the parallel simulation of large high speed interconnects. This algorithm is highly parallelizable, demonstrates naturally swift convergence and the associated computational costs show excellent scalability with the size of the network and the number of CPUs available. Moreover, a hybrid iterative scheme that combines the high parallelizability of the GJ iterative technique with the superior convergence of the GS technique is developed to further accelerate the speed of WR iterations.

Fourthly, the LP-WR algorithms developed for transient analysis of interconnects have been extended to include EMI analysis. A key feature of this work has been that the advantages of the hybrid iterative technique are easily retained for the problem of EMI analysis of interconnects. Moreover, novel techniques to compress the size of subcircuits and reduce communication overheads during iterations have been developed. In addition, techniques based on time windowing and the delay extraction feature of DEFACT have

been exploited to ensure an improved initial guess of the waveforms of the relaxation sources thereby further accelerating the convergence.

Finally, the attributes of the above LP-WR algorithm has been extended to the modeling of the singly layered PDNs. For the problem of PDNs, a 2D partitioning scheme based on the DEPACT model has been developed. The regular distribution of global decoupling capacitors has been considered as additional drain paths for the SSN injected into the PDNs, thereby ensuring good localization of the SSN and consequently efficient convergence of WR iterations. The hybrid iterative technique developed previously for interconnects has been extended to the 2D problem of PDNs.

For each of the above contribution, several numerical examples are provided in this thesis to demonstrate the validity and efficiency of the proposed algorithms.

8.2 Future Work

This section provides some suggestions for future research based on the work presented in this thesis:

1. The extension of WR to PDN modeling is based on an assumption of regular arrangement of decoupling capacitors. However, in many design scenarios, decoupling capacitors are located near to the position of the SSN source (i.e. the position of the ICs embedded in the PDN) rather than being distributed all over the PDN. In such cases, the arrangement of decoupling capacitors may not cover the entire PDN area and this has been found to lead to relatively slow convergence. New

- techniques based on overlapping based WR are currently being investigated that can ensure fast convergence. Overlapping based WR however require multiple solution of the same subcircuit and do not scale optimally with regard to its CPU costs. As a result, novel methodologies need to be developed for faster solution of overlapping based WR iterations and this is a currently open topic of research.
2. Applications of LP-WR for the parallel simulation of power transmission line issues such as corona discharge, lightening discharge and overvoltage analysis can be examined.
 3. While the developed LP-WR provide excellent results where the number of DEFACT sections may increase due to an increase in line resistance, line length or frequency of operation, it still requires the simulation of MTL DEFACT subcircuits and does not scale well with large number of coupled lines. On the other hand, alternative WR algorithms based on a transverse partitioning (TP-WR) can separate the MTL into multiple single line examples which can then be solved iteratively. Hence, in my future work I will seek to combine the LP-WR with the TP-WR to develop a new 2D partitioning methodology based on simultaneous longitudinal and transverse partitioning for taking into account both larger number of DEFACT sections and larger number of coupled interconnects.
 4. The 2D partitioning methodology used for parallel simulation of single layered PDNs in [81] need to be extended to the problem of 3D partitioning for parallel simulation of multilayered PDNs. In order to do so, I am currently investigating decoupling the plane layers using the TP-WR techniques of [59] and then further partitioning each plane layer into smaller subcircuits using the 2D partitioning methodology of [81].

Such a 3D partitioning based WR algorithm is expected to be highly effective for parallel SPICE simulation of complex 3D PDN problems.

References

- [1] C. R. Paul, *Analysis of multiconductor transmission lines*, 2nd ed. New Jersey, NY: John Wiley and Sons, 2008.
- [2] R. Achar and M. Nakhla, "Simulation of high-speed interconnects," *Proc. IEEE*, vol. 89, no. 5, pp. 693-728, May 2001.
- [3] A. Ruehli and A. Cangellaris, "Progress in the methodologies for the electrical modeling of interconnects and electronic packages," *Proc. IEEE*, vol. 89, no. 5, pp. 740–771, May 2001.
- [4] R. R. Tummala, E. J. Rymaszewski, and A.G. Klopfenstein, *Microelectronics Packaging Handbook, pt. I, second ed.* New York: Chapman Hall, 1997.
- [5] M. Swaminathan and A. E. Engin, *Power Integrity Modeling and design for Semiconductors and Systems*. Boston, MA.: Prentice Hall, 2007.
- [6] *HSPICE Signal Integrity User Guide*. Release U-2010.12-RA: Synopsys, Inc., Sep. 2010.
- [7] T. Beyene and J. E. Schutt-Aine, "Accurate frequency-domain modeling and simulation of high-speed packaging interconnects," *IEEE Trans. Microw. Theory Tech.*, vol. 45, no. 10, pp. 1941- 1947, Oct. 1997.
- [8] W. T. Beyene and J. E. Schutt-Aine, "Efficient transient simulation of high-speed interconnects characterized by sampled data," *IEEE Trans. Comp., Packag, Manufact. Technology-Part B*, vol. 21, no. 1, pp. 105-114, Feb. 1998.
- [9] M. Elzinga, K. L. Virga, L. Zhao and J. L. Prince, "Pole-residue formulation for

- transient simulation of high-frequency interconnects using householder LS curve-fitting techniques,” *IEEE Trans. Adv. Packag.*, vol. 23, no. 2, pp. 142-147, May 2000.
- [10] B. Gustavsen and A. Semlyen, “Rational approximation of frequency domain responses by vector fitting,” *IEEE Trans. Power Delivery*, vol. 14, no. 3, pp. 1052-1061, July 1999.
- [11] D. Saraswat, R. Achar and M. Nakhla, “A fast algorithm and practical considerations for passive macromodeling of measured/simulated data,” *IEEE Trans. Comp., Packag, Manufact. Technology-Part B*, vol. 27, no. 1, pp. 57-70, Feb. 2004.
- [12] A. Charest, D. Saraswat, M. Nakhla, R. Achar and N. Soveiko, “Compact macromodeling of high-speed circuits via delayed rational functions,” *IEEE Microwave and Wireless Component Letters*, vol. 17, no. 12, pp. 828 -830, Dec. 2007.
- [13] A. Charest, M. S. Nakhla, R. Achar, D. Saraswat, N. Soveiko and I. Erdin, “Time domain delay extraction-based macromodeling algorithm for long-delay networks,” *IEEE Trans. Adv. Packag.*, vol. 33, no. 1, pp. 219-235, Feb. 2010.
- [14] A. Chinae, P. Triverio, and S. Grivet-Talocia, “Delay-based macromodeling of long interconnects from frequency-domain terminal responses,” *IEEE Trans. Adv. Packag.*, vol. 33, no. 1, pp. 246-256, Feb. 2010.
- [15] P. Triverio, S. Grivet-Talocia, and A. Chinae, “Identification of highly efficient delay-rational macromodels of long interconnects from tabulated frequency data,” *IEEE Trans. Microw. Theory Tech.*, vol. 58, no. 3, pp. 566-577, March 2010.

- [16] C. P. Coelho, J. R. Phillips and L. M. Silveira, "A convex programming approach for generating guaranteed passive approximations to tabulated frequency data," *IEEE Trans. CAD of Integrated Circuits and Syst.*, vol. 48, no. 9, pp. 293-301, Sept. 2004.
- [17] G. Antonini, "SPICE equivalent circuits of frequency-domain responses," *IEEE Trans. Electromag. Compatibility*, vol. 45, no. 8, pp. 502-512, Aug. 2003.
- [18] S. Min and M. Swaminathan, "Construction of broadband passive macromodels from frequency data for simulation of distributed interconnect networks," *IEEE Trans. Electromag. Compatibility*, vol. 46, no. 4, pp. 544-558, Nov. 2004.
- [19] S. N. Lalgudi, E. Engin, G. Casinovi and M. Swaminathan, "Accurate transient simulation of interconnect characterized by band-limited data with propagation delay enforcement in a modified nodal analysis framework," *IEEE Trans. Electromag. Compatibility*, vol. 50, no. 3, pp. 715-729, Aug. 2008.
- [20] A. Beygi and A. Dounavis, "An instrumental variable vector-fitting approach for noisy frequency responses," in *IEEE Trans. Microw. Theory Tech.*, vol. 60, no. 9, pp. 2702-2712, Sept. 2012.
- [21] S. Roy and A. Dounavis, "Transient simulation of distributed networks using delay extraction based numerical convolution", in *IEEE Transactions on CAD of Integrated Circuits and Syst.*, vol. 30, no. 3, pp. 364-373, March 2011.
- [22] N. Na, J. Choi, S. Chun and M. Swaminathan, "Modeling and transient simulation of planes in electronic packages," *IEEE Trans Adv. Packag.*, vol. 23, no. 3, pp. 340-352, Aug. 2000.

- [23] A. Odabasioglu, M. Celik, and L. T. Pilleggi, "PRIMA: Passive Reduced-Order Interconnect Macromodeling Algorithm," *IEEE Transactions on CAD of Integrated Circuits and Sysys.*, vol. 17, no. 8, pp. 645-653, August 1998.
- [24] A. Dounavis, R. Achar, and M. Nakhla, "Efficient passive circuit models for distributed networks with frequency-dependent parameters," *IEEE Trans. on Adv. Packag.*, vol. 23, pp. 382-392, August 2000.
- [25] A. Dounavis, R. Achar, and M. Nakhla, "A general class of passive macromodels for lossy multiconductor transmission lines," *IEEE Trans. Microw. Theory Tech.*, vol. 49, pp. 1686-1696, October 2001.
- [26] F. H. Branin, Jr., "Transient analysis of lossless transmission lines," *Proc. IEEE*, vol. 55, no. 11, pp. 2012-2013, Nov. 1967.
- [27] F. Y. Chang, "The generalized method of characteristics for waveform relaxation analysis of lossy coupled transmission lines," *IEEE Trans. Microw. Theory Tech.*, vol. 37, no. 12, pp. 2028-2038, Dec. 1989.
- [28] S. Grivet-Talocia, H. M. Huang, A. E. Ruehli, F. Canavero, and I. M. Elfadel, "Transient analysis of lossy transmission lines: An efficient approach based on the method of characteristics," *IEEE Trans. Adv. Packag.*, vol. 27, no. 1, pp. 45-56, Feb. 2004.
- [29] A. Dounavis and V. Pothiwala, "Passive closed-form transmission line macromodel using method of characteristics," *IEEE Trans. Adv. Packag.*, vol. 31, no. 1, pp. 190-202, Feb. 2008.
- [30] A. Dounavis, V. Pothiwala and A. Beygi "Passive macromodeling of lossy

- multiconductor transmission lines based on the method of characteristics,” *IEEE Trans. Adv. Packag.*, vol. 32, no. 1, pp. 184–198, Feb. 2009.
- [31] N. Nakhla, A. Dounavis, R. Achar and M. S. Nakhla, “DEPACT: Delay extraction–based passive compact transmission–line macromodeling algorithm,” *IEEE Trans. Adv. Packag.*, vol. 28, no. 1, pp. 13-23, Feb. 2005.
- [32] N. Nakhla, M. S. Nakhla and R. Achar, "Simplified delay extraction-based passive transmission line macromodeling algorithm," *IEEE Trans. Adv. Packag.*, vol. 33, no. 2, pp. 498-509, May 2010.
- [33] L. Smith, R. Raymond, and T. Roy, “Power plane SPICE models and simulated performance for materials and geometries,” *IEEE Trans. Adv. Packag.*, vol. 24, no. 3, pp. 277–287, Aug. 2001.
- [34] S. Lin and E.S. Kuh, "Transient simulation of lossy interconnects based on the recursive convolution formulation," *IEEE Trans. Circuits Systems I*, vol. 39, no. 11, pp. 879-892, November 1992.
- [35] S. Grivet-Talocia, "Passivity enforcement via perturbation of Hamiltonian matrices," *IEEE Trans. Circuits Syst. I*, vol. 51, no. 9, pp. 1755–1769, Sep. 2004.
- [36] F. M. Tesche, “On the use of the Hilbert transform for processing measured CW data,” *IEEE Trans. Electromag. Compatibility.*, vol. 34, no. 3, pp. 259–266, Aug. 1992.
- [37] A. E. Engin, K. Bharath and M. Swaminathan, “Multilayered finite-difference method (MFDM) for modeling of package and printed circuit board planes”, *IEEE Trans. Electromag. Compatibility*, vol. 49, no. 2, pp. 441-447, May 2007.

- [38] F. Fer, "Resolution de l'equation matricielle par produit infini d'exponentielles matricielles," *Acad. Roy. Belg. Cl. Sci.*, vol. 44, no. 5, pp. 818–829, 1958.
- [39] C. D. Taylor, R. S. Satterwhite, and C. W. Harrison, "The response of a terminated two-wire transmission line excited by a nonuniform electromagnetic field," *IEEE Trans. Antennas Propagat.*, vol. 13, no. 6, pp. 987–989, November 1965.
- [40] C. R. Paul, "Frequency response of multiconductor transmission lines illuminated by an incident electromagnetic field," *IEEE Trans. Microw. Theory Tech.*, vol. 22, pp. 454–457, April 1967.
- [41] C. R. Paul, "A SPICE model for multiconductor transmission lines excited by an incident electromagnetic field," *IEEE Trans. Electromagn. Compatibility*, vol. 36, pp. 342–354, November 1994.
- [42] C. R. Paul, "Literal solutions for the time-domain response of a two-conductor transmission line excited by an incident electromagnetic field," *IEEE Trans. Electromagn. Compatibility*, p. 37, May 1995.
- [43] A. K. Agrawal, H. J. Price, and S. H. Gurbaxani, "Transient response of multiconductor transmission lines excited by a nonuniform electromagnetic field," *IEEE Trans. Electromagn. Compatibility*, vol. EMC-22, no. 2, pp. 119–129, May 1980.
- [44] Y. Kami and R. Sato, "Circuit-concept approach to externally excited transmission lines," *IEEE Trans. Electromagn. Compatibility*, vol. EMC-27, no. 4, pp. 177–183, Nov. 1985.

- [45] P. Bernardi, R. Cicchetti, and C. Pirone, "Transient response of a microstrip line circuit excited by an external electromagnetic source," *IEEE Trans. Electromagn. Compatibility*, vol. 34, no. 2, pp. 100–108, May 1992.
- [46] I. Wuyts and D. Zutter, "Circuit model for plane-wave incidence on multiconductor transmission lines," *IEEE Trans. Electromagn. Compatibility*, vol. 36, no. 3, pp. 206–212, Aug. 1994.
- [47] I. Maio and F. Canavero, "Analysis of crosstalk and field coupling to lossy MTLs in a SPICE environment," *IEEE Trans. Electromagn. Compatibility*, vol. 38, no. 3, pp. 221–229, Aug. 1996.
- [48] I. Erdin, R. Khazaka, and M. Nakhla, "Simulation of high-speed interconnects in a multilayered medium in the presence of incident field," *IEEE Trans. Microw. Theory Tech.*, vol. 46, no. 12, pp. 2251–2257, December 1998.
- [49] I. Erdin, A. Dounavis, R. Achar, and M. Nakhla, "A SPICE model for incident field coupling to lossy multiconductor transmission lines," *IEEE Trans. Electromagn. Compatibility*, vol. 43, no. 4, pp. 485–494, November 2001.
- [50] G. S. Shinh et al., "Fast transient analysis of incident field coupling to multiconductor transmission lines," *IEEE Trans. Electromagn. Compatibility*, vol. 48, no. 1, pp. 57–73, February 2006.
- [51] G. S. Shinh, R. Achar, N.M. Nakhla, M.S. Nakhla, and I. Erdin, "Simplified macromodel of MTLs with incident fields (SiMMIF)," *IEEE Trans. on Electromagn. Compatibility*, vol. 50, no. 2, pp. 375 - 389, May 2008.
- [52] A. Beygi and A. Dounavis, "Analysis of excited multiconductor transmission lines

- based on the passive method of characteristics macromodel," *IEEE Transactions on Electromagnetic Compatibility*, vol. 54, no. 6, pp. 1281 - 1288 , Dec. 2012.
- [53] E. Lelarasmee, A. E. Ruehli, and A. L. Sangiovanni-Vincentelli, "The waveform relaxation method for time-domain analysis of large-scale integrated circuits", *IEEE Trans. CAD of Integrated Circuits and Syst.*, vol. 1, no. 3, pp. 131-145, July 1982.
- [54] D. Paul, N. M. Nakhla, R. Achar and M. S. Nakhla, "Parallel simulation of massively coupled interconnect networks", *IEEE Trans. Adv. Packag.*, vol. 33, no. 1, pp. 115-127, Feb. 2010.
- [55] J. White and A. L. Sangiovanni-Vincentelli, *Relaxation Techniques for the Simulation of VLSI Circuits*, Norwell, MA: Kluwer Academic Publications, 1987.
- [56] M. J. Gander and L. Halpern, "Optimized Schwarz waveform relaxation methods for advection reaction diffusion problems", *SIAM J. Numer. Anal.*, vol. 45, no. 2, pp. 666–697, April 2007.
- [57] M. J. Gander, "Overlapping Schwarz waveform relaxation methods for parabolic problems", *Proc. Algoritmy'97*, 1997, pp. 425-431.
- [58] M. Al-Khaleel, A. E. Ruehli and M. J. Gander, "Optimized waveform relaxation methods for longitudinal partitioning of transmission lines," *IEEE Trans. Circuits and Systems I: Regular Papers*, vol. 56, no. 9, pp. 1732-1743, Aug. 2009.
- [59] N. M. Nakhla, A.E. Ruehli, R. Achar and M. S. Nakhla, "Simulation of coupled interconnects using waveform relaxation and transverse partitioning", *IEEE Trans. Adv. Packag.*, vol. 29, no. 1, pp. 78-87, Feb. 2006.
- [60] N. Nakhla, A. E. Ruehli, M. S. Nakhla, R. Achar and C. Chen, "Waveform

- relaxation techniques for simulation of coupled interconnects with frequency-dependent parameters”, *IEEE Trans. Adv. Packag.*, vol. 30, no. 2, pp. 257-269, May 2007.
- [61] A. R. Sridhar, N. M. Nakhla, R. Achar, M. S. Nakhla and A. E. Ruehli, “Fast EMI analysis via transverse partitioning and waveform relaxation”, *IEEE Trans. Electromagn. Compatibility*, vol. 51, no. 2, pp. 358-371, May 2009.
- [62] M. A. Farhan, N. M. Nakhla, M. S. Nakhla, R. Achar and A. E. Ruehli, “Overlapping partitioning techniques for simulation of strongly coupled distributed interconnects”, *IEEE Trans. Comp., Packag. Manufact. Technology*, vol. 2, no. 7, pp. 1192-1201, July 2012.
- [63] Y.-Z. Xie, F. G. Canavero, T. Maestri and Z.-J. Wang, “Crosstalk analysis of multiconductor transmission lines based on distributed analytical representation and iterative technique”, *IEEE Trans. Electromag. Compatibility*, vol. 52, no. 3, pp. 712-727, Aug. 2010.
- [64] F. Y. Chang, “The generalized method of characteristics for waveform relaxation analysis of lossy coupled transmission lines,” *IEEE Trans. Microw. Theory Tech.*, vol. 37, no. 12, pp. 2028–2038, Dec. 1989.
- [65] F. Y. Chang, “Waveform relaxation analysis of RLCG transmission lines”, *IEEE Trans. Circuits and Systems*, vol. 37, no. 11, pp. 1394-1415, Nov. 1990.
- [66] F. Y. Chang, “Relaxation simulation of transverse electromagnetic wave propagation in coupled transmission lines”, *IEEE Trans. Circuits and Systems*, vol. 38, no. 8, pp. 916-936, Aug. 1991.

- [67] F. Y. Chang, "Waveform relaxation analysis of nonuniform loss transmission lines characterized with frequency dependent parameters", *IEEE Trans. Circuits and Systems*, vol. 38, no. 12, pp. 1484-1500, Dec. 1991.
- [68] F. Y. Chang, "Transient simulation of nonuniform coupled lossy transmission lines characterized with frequency-dependent parameters-part I: waveform relaxation analysis", *IEEE Trans. Circuits and Systems I – Fundamental Theory and Appl.*, vol. 39, no. 8, pp. 585-603, Aug. 1992.
- [69] R. Achar et al., "Parallel and scalable transient simulator for power grids via waveform relaxation (PTS-PWR)," *IEEE Trans. VLSI Syst.*, vol. 19, no. 2, pp. 319-332, Feb. 2011.
- [70] J. Yao and P. Krolak, "The generalized Gabor transform," *IEEE Trans. Image Processing*, vol. 4, no. 7, pp. 978-988, July, 1995.
- [71] A. I. Zayed, *Handbook of Function and Generalized Function Transformation*. New York: CRC Press 1996.
- [72] L. Mansinha, R. Stockwell, and R. Lowe, "Local S-spectrum analysis of 1-D and 2-D data", *Physics of the Earth and Planetary Interiors*, vol. 103, no. 3-4, pp. 329-336, Nov. 1997.
- [73] R. Stockwell, L. Mansinha and R. Lowe, "Localization of the complex spectrum: the S transform", *IEEE Trans. Signal Processing*, vol. 44, no. 4, pp. 998-1001, 1996.
- [74] S. Roy and A. Dounavis, "Efficient modeling of power/ground planes using delay extraction based transmission lines", *IEEE Trans. Comp., Packag, Manufact. Technology*, vol. 1, no. 5, pp. 761-771, May 2011.

- [75] S. Roy and A. Dounavis, "Macromodeling of multilayered power distribution network based on a multiconductor transmission line approach", accepted for future publication in *IEEE Trans. Comp., Packag, Manufact. Technology*, January 2013.
- [76] S. Roy, A. Dounavis and A. Beygi, "Fast electromagnetic interference analysis of distributed networks using longitudinal partitioning based waveform relaxation", in *Proc. IEEE MTT-S 60th International Microwave Symposium*, June 2012, pp. 1-3.
- [77] S. Roy, A. Dounavis and A. Beygi, "Longitudinal-partitioning-based waveform relaxation algorithm for efficient analysis of distributed transmission-line networks", *IEEE Trans. Microw. Theory Tech.*, vol. 60, no. 3, pp. 451-463, March 2012.
- [78] S. Roy, A. Beygi and A. Dounavis, "Fast electromagnetic interference analysis of distributed networks using longitudinal partitioning based waveform relaxation", *Proc. IEEE MTT-S 60th International Microwave Symposium*, June 2012, pp. 1-3.
- [79] S. Roy, A. Beygi and A. Dounavis, "Electromagnetic interference analysis of multiconductor transmission line networks using longitudinal partitioning based waveform relaxation algorithm", *IEEE Trans. Electromag. Compat.*, vol. 55, no. 2, pp. 395-406, April 2013.
- [80] S. Roy and A. Dounavis, "Waveform relaxation based analysis of noise propagation in power distribution networks", in *Proc. 20th IEEE Conference on Electrical Performance of Electronic Packages*, October 2011, pp. 255-258.
- [81] S. Roy and A. Dounavis, "Delay extraction based waveform relaxation algorithm for fast transient analysis of power distribution networks", *IEEE Trans. Comp., Packag, Manufact. Technology*, vol. 2, no. 12, pp. 2044-2056, December 2012.

- [82] J. Fan, J. L. D. Knighten, N. W. Smith, A. Orlandi, T. P. Van Doren, T. H. Hubing, and R. E. DuBroff, "Quantifying SMT decoupling capacitor placement in DC power-bus design for multilayer PCBs," *IEEE Trans. Electromag. Compat.*, vol. 43, no. 4, pp. 712–727, Nov. 2001.
- [83] J. Fan, W. Cui, D. L. James, D. P. Thomas, and J. L. Knighten, "Estimating the noise mitigation effect of local decoupling in printed circuit boards," *IEEE Trans. Adv. Packag.*, vol. 25, no. 2, pp. 588–599, May 2002.

Curriculum Vitae

Name: Sourajeet Roy

Post-secondary Education and Degrees: Sikkim Manipal Institute of Technology
Rangpo, India
2002-2006 B. Tech.

The University of Western Ontario
London, Ontario, Canada
2007-2009 M. E. Sc.

The University of Western Ontario
London, Ontario, Canada
2009-2013 Ph.D.

Related Work Experience Research Assistant
The University of Western Ontario
2007-2013

Teaching Assistant
The University of Western Ontario
2007-2013

Selected Publications:

S. Roy and A. Dounavis, "Parallel transient simulation of package/board power distribution networks based on a two-dimensional overlapping partitioning methodology", accepted for publication in *IEEE Trans. Comp., Packag, Manufact. Technology*, May 2013

S. Roy, A. Beygi and A. Dounavis, "Electromagnetic interference analysis of multiconductor transmission line networks using longitudinal partitioning based waveform relaxation algorithm", *IEEE Trans. Electromag. Compat.*, vol. 55, no. 2, pp. 395-406, April 2013.

S. Roy and A. Dounavis, "Delay extraction based waveform relaxation algorithm for fast transient analysis of power distribution networks", in *IEEE Trans. Comp., Packag, Manufact. Technology*, vol. 2, no. 12, pp. 2044-2056, December 2012.

S. Roy, A. Dounavis and A. Beygi, "Longitudinal-partitioning-based waveform relaxation algorithm for efficient analysis of distributed transmission-line networks", *IEEE Trans. Microw. Theory Tech.*, vol. 60, no. 3, pp. 451-463, March 2012.